Thin-disk lasers based on Yb^{3+}-doped ceramics

Doctor of Engineering

Department of Engineering Science
Graduate School of Informatics and Engineering
University of Electro-Communications

Hiroaki Nakao

March 2015

Thin-disk lasers based on Yb^{3+}-doped ceramics

APPROVED BY SUPERVISORY COMMITTEE:

CHAIRPERSON : Assoc. Prof. Akira Shirakawa

MEMBER : Prof. Hitoki Yoneda

MEMBER : Prof. Masayoshi Watanabe

MEMBER : Prof. Masayuki Katsuragawa

MEMBER : Assoc. Prof. Junji Kawanaka

和文概要

本論文では、Yb^{3+}添加セラミック材料を用いた thin-disk レーザーの特性評価及び高効率 · 高出力動作の実証、また利得媒質とヒートシンクの独自の接合工程の開発を行った。現在、高出力レーザーは加工等の産業応用が盛んに行われており、基礎研究においても新たな分野の開拓が成されている。光源に対しては、主として高効率 · 高出力 · 高輝度であることが要求されるが、従来用いられていたバルク型 · ファイバー型のレーザーでは、熱光学的歪曲や非線形性の抑制に課題があった。これらの問題に対して、thin-disk 型のレーザーは優位な特性を示す。薄い利得媒質 ($100 \sim 500\ \mu m$) を面冷却することから、高い冷却能力及び小さな非線形性が得られる。更に熱流束がレーザーの光軸と同軸であるため、熱光学的歪曲の最小化が可能となる。また利得媒質として、低発熱かつ高効率動作が可能な Yb^{3+}添加材料を用いることで、特に高平均出力超短パルスレーザー動作に優位性を示し、近年、急速に実証や製品化が進んでいる。しかし、ほぼ全ての光源において単結晶材料が用いられている。セラミック材料での実証例はほぼ無く、その理由も不明である。セラミック材料は単結晶材料と比較し、機械的強度の向上や高濃度添加等の可能性があり、高出力レーザー光源用利得媒質として重要な材料である。従って、セラミック材料を用いた thin-disk レーザーの実証を行い、セラミック材料の有用性の評価を行うことを目的とした。また他の目的として、利得媒質とヒートシンクの独自の接合工程の開発がある。接合部の品質は、thin-disk レーザーの性能を左右する最も重要な点である。しかし、接合はドイツの一部企業 · 大学のみでしかできず、世界的に thin-disk レーザーは大きくドイツに依存している。従って、ドイツの研究機関と競合するため、また、研究途上で発生した問題や要求に柔軟に対応することができる環境を構築するためにも、独自の接合技術の開発は必要不可欠である。評価を行う材料として、thin-disk レーザーで特に顕著になる問題の解決が可能な材料に注目した。Thin-disk レーザーは相互作用長が短く、励起光吸収量や利得が小さい。これらを補うために、利得媒質に複数回励起光を入射するマルチパス励起光学系や、高濃度添加材料が用いられる。しかし、Yb^{3+}イオンの添加濃度の増加に伴い、熱伝導率の低下や強励起時の非線形過程の増加が発生する。前者は Yb^{3+}イオンと置換される母材の質量差に起因するため、Yb^{3+}イオンとほぼ同等の質量を持つ Lu^{3+}イオンを含む材料を用いることで抑制可能である。後者は特に添加濃度分布の制御が困難な単結晶で問題となるもので、添加濃度の上限を制限している。これは、我々が神島化学工業 (株) と共同開発した非反応性焼結法による、均一な添加濃度の制御により抑制が可能である。以上より、Lu を含むセラミック材料が望ましく、その中でも特に $Lu_3Al_5O_{12}$ (LuAG) 及び Lu_2O_3 に注目した。Yb:LuAG は、現在最も重要な利得媒質である Yb:$Y_3Al_5O_{12}$ (YAG) と類似した材料であり、高濃度添加と高熱伝導率の両立が可能である。また、Yb:YAG と比較し利得が大きく、増幅器として有望な材料である。Yb:Lu_2O_3 は Yb:YAG と比較

し、高い熱伝導率及び広い利得帯域幅を示す。超短パルスレーザー発振器として重要な材料であるが、融点が高く大口径な単結晶育成が困難である。セラミックであれば、融点以下での焼結が可能であるため大口径な媒質の作製が可能である。10 at.% Yb^{3+}添加 LuAG セラミックを用いて thin-disk レーザーの特性評価を行った。最大出力 · 効率等の評価のために連続 (CW) 空間多モード発振実験を行った。厚さ 150 μm の試料を用いて、最高出力 166 W、スロープ効率 72%、光-光変換効率 60%を実証した。これは現在単結晶 Yb:LuAG で報告されている効率と同等である。次に共振器設計による試料上での TEM_{00} モード径の制御を行い、CW 空間単一モード発振実験を行った。試料上での TEM_{00}モード径を励起光径の 80%に制御することで、厚さ 200 μm の試料にて回折限界に近いビーム品質 ($M^2 = 1.22$) を達成した。また、薄いセラミック材料での影響が懸念される、偏光解消効果についても評価を行った。共振器内に偏光選択のためのブリュースタ板 (BP) を挿入し、出射ビームの偏光度及び偏光解消による損失の評価を行った。厚さ 200 μm の試料において、偏光度は約 99.5%、共振器一周での偏光解消による損失は約 0.15%であった。これらの結果から、セラミック材料が thin-disk レーザーでも有用であることが明らかにされた。3 at.% Yb^{3+}添加 Lu_2O_3 セラミックを、開発した接合行程にて接合し、自作のマルチパス励起光学系を用いて thin-disk レーザーの特性評価を行った。接合方法として、In-Sn ハンダを用いた接合及び、エポキシ樹脂を用いた接合の 2 種類を開発した。厚さ 300 μm でハンダ接合された試料を用い、スロープ効率 61%、光-光変換効率 45%の CW 空間多モード発振を実証した。また、厚さ 250 μm でエポキシ接合された試料を用い、スロープ効率 56%、光-光変換効率 44%の CW 空間多モード発振を実証した。この時、最大励起密度は一般的な破壊閾値 (5 kW/cm^2) に近い 4.4 kW/cm^{2}に達したが、試料の破損やレーザー動作に不安定性等は観測されなかった。また、接合試料のサーモグラフィー測定から、より高い励起密度 (6 kW/cm^{2}以上) での thin-disk レーザー動作の可能性も示唆された。これらの結果より、接合工程の基盤技術の確立が証明された。

Abstract

Thin-disk laser is one of the key technologies in modern high power laser fields. It enables to realize high beam quality under high average power operation owing to its almost negligible thermo-optic distortions. Recently, various thin-disk laser sources based on single crystals have been investigated, whereas only a few thin-disk lasers have been demonstrated with ceramics. In this thesis, the performances of the thin-disk lasers are evaluated. These are based on Yb^{3+}-doped ceramics, especially Yb^{3+}-doped $Lu_3Al_5O_{12}$ (LuAG) and Yb^{3+}-doped Lu_2O_3 ceramics which are expected to have advantages in high power and highly efficient operations. The spectroscopic properties and the thermal properties of the ceramics are measured systematically. Using the Yb:LuAG ceramic with a doping concentration of 10 at.% and a thickness of 150 μm, a high power and a highly efficient thin-disk laser operation is demonstrated in a continuous wave (CW) regime. The maximum output power reaches 166 W with the maximum slope efficiency and the maximum optical efficiency of 72% and 60%, respectively. The efficiencies are almost comparable to those of the thin-disk lasers based on Yb:LuAG single crystals. These results show that ceramics are one of the best gain media for the thin-disk lasers as is the case in the single crystals. The Yb:Lu_2O_3 ceramics with a doping concentration of 3 at.% are contacted on copper heat sinks with new contacting schemes. The thin-disk lasers based on Yb:Lu_2O_3 ceramics were demonstrated in a CW regime. The maximum slope efficiency of 61% and the maximum optical efficiency of 45% are achieved with 300 μm-thick ceramic thin-disk. Any damages of the disks and instabilities are not observed in those operation parameters. Additionally, the high damage threshold of the disks (at least 6 kW/cm^2) is expected from the thermographical measurements of the disks. These results denote that the new schemes can be used for high power lasers.

Contents

List of Figures

List of Tables

List of acronyms

AOM acousto-optic modulator 44

ASE amplified spontaneous emission 106

Au-Sn gold-tin 27

BBO BaB_2O_4 45

BP Brewster's plate 71

bpp bipolar push-pull 45

BS beam splitter 32

CW-ML CW mode-locked operation 58

Cz Czochralski 9

DFB-LD distributed feedback LD 91

DFT discrete Fourier-transform 93

DM dichroic mirror 55

EOM eletctro-optic modulator 45

FAP $Ca_5(PO_4)_3F$ 15

FCLD fiber-coupled laser diode 55

FRCI focus retro-collimated interferometer 32

FT Fourier-transform 32

FWHM full width half maximum 54

GDD group delay dispersion 57

GLP Glan-laser prism 72

GTI Gires-Tournois interferometer 57

HR high reflection 55

HT high transmission 55

IFSW Institut für Strhalwerkzeuge 4

IFT inverse Fourier-transform 39

In-Sn indium-tin 27

IR infrared 50

LD laser diode 53

LuAG $Lu_3Al_5O_{12}$ 2

MI Michelson interferometer 32

NA numerical aperture 55

OC output coupler 55

OPD optical path difference 26

PC Pockels-cell 45

PSI phase shifting interferometer 32

PZT piezoelectric transducer 109

Q-ML Q-switched mode-locking 58

QWP quarter-wave plate 44

RE rare earth 6

RE_2O_3 sesquioxide 2

ROC radius of curvature 33

SEM scanning electron microscope 48

SESAM semiconductor saturable absorber mirror 18

SSL solid-state laser 1

TFP thin-film polarizer 46

VBG volume-bragg grating 87

VESTA visualization for electronic and structural analysis 18

YAG $Y_3Al_5O_{12}$ 2

Yb Ytterbium 6

Chapter 1

Introduction

1.1 Motivation

The thin-disk concept, first introduced by A. Giesen in 1994 [1], is one of the most progressive technology especially in recent high power, ultrashort pulsed laser fields. Though a wide variety of the pulsed laser sources based on fibers or bulk solids have been produced, a strong trade off is existed between repetition rate and pulse energy. Figure 1.1 describes a typical relationship between pulse energies and the repetition rates of conventional pulsed laser sources. Most of the sources indicate tendencies that "the high repetition rate but the low pulse energy"or "the low repetition rate but the high pulse energy"with a constant average power. The critical limitation for realizing high pulse energy and high repetition rate (corresponding to high average power) with high brightness and short pulse durations of ps-fs regime are the nonlinearity of the gain medium under a high peak power operation and a thermal management. The thin-disk concept gives the solution to suppress both negative factors. Its approximately one-dimensional thermal distribution inside the gain medium led by the combination of an uni-axial heat flow and a large pump spot size compared with the thickness of the gain medium significantly suppresses harmful thermo-optic distortions which are always fatal disadvantages in conventional solid-state lasers (SSLs). The short thickness of the gain medium and the large pump spot size on the disk lead to an almost negligible nonlinearity which is one of the limitation factor in fiber lasers. These advantages of the thin-disk concept make it a breakthrough technology to scale average powers to hundreds of W $\sim$ kW-level and more.

The thin-disk laser sources have intensively been investigated and commer-

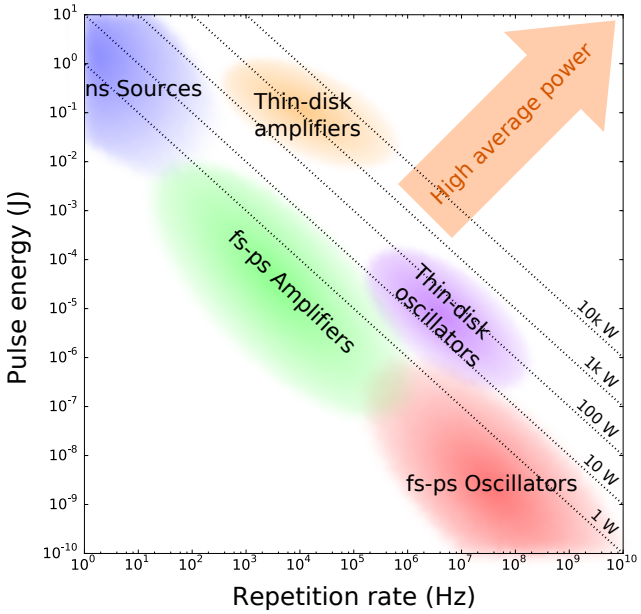

Fig. 1.1: Typical tendency of the relationship between the pulse energy and the repetition rate. Dotted lines indicate average powers. The typical distributions for the conventional laser sources based on fibers, bulk-solids, and thin-disks are shown.

cialized in recent years. Currently, Yb^{3+}-doped $Y_3Al_5O_{12}$ (YAG) single crystal is employed as the gain medium especially for high energy/power purposes. YAG is the most sophisticated host material and thus it has the powerful driving force to develop new scientific fields and markets. Of course, potentials of other host materials, e.g. $Lu_3Al_5O_{12}$ (LuAG) [2], sesquioxides (RE_2O_3s) and $LuScO_3$ [3], for the thin-disk laser have intensively been investigated. It is very worthwhile subject to broaden the aspect and enhance performances further because the performances of the lasers strongly depend on the properties of the gain material (host material).

Generally, the gain materials are mainly desired to have broad gain bandwidth, large emission cross section and high mechanical toughnesses for high power and ultrashort pulse generations. In addition, the thermal conductivity of the gain medium is important even in the thin-disk concept. Extra temperature rising of the disk caused by the low thermal conductivity not only degrades the wavefront of the laser beam, but also lower the repetition rate and the damage threshold. In the thin-disk concept, the thin-disk shaped gain medium itself not only enables the effective thermal management, but

also lowers one-pass pump absorption. A multi-pass pumping system and high rare earth (RE^{3+}) doping are required to improve the total pump absorption. The high Yb^{3+}-doping leads to the significant decline of the thermal conductivity due to the mismatch of the atomic mass between the host atom and RE^{3+} [4]. In terms of satisfying high thermal conductivity and high RE^{3+} doping simultaneously, the Lu-based materials are focused as promising host materials because of almost the same atomic mass of Lu^{3+} as that of Yb^{3+} [2].

Investigating the potentials of the ceramic materials as the gain media for the thin-disk lasers is another important issue. Though many thin-disk lasers based on single crystalline materials have been demonstrated, to the best of our knowledge, only five demonstrations of the thin-disk lasers based on the ceramics have been reported. Two reports employs Yb:YAG ceramic thin-disks as the gain media [5,6]. Only our group have reported the thin-disk lasers based on the ceramic gain media other than Yb:YAG [7–9]. Why are not the activities of the ceramic thin-disk lasers so high despite the ceramics are now widely used in bulk- or slab-concepts? Investigating the ceramic thin-disk lasers and finding out the performances are the important subject. Generally, the mechanical toughnesses of the ceramic are higher than those of the single crystal. Hence the current maximum extractable energy/peak power limited by the damage threshold of the gain medium itself is possible to be scaled by employing the ceramics as the gain media. An additional advantage in the ceramic is possibility to fabricate RE_2O_3 with a large aperture size and high optical quality. Though the optimized heat exchanger method enables the growth of RE_2O_3 with high optical quality [10], the available aperture size is limited due to their quite high melting temperatures. Fabrication of RE_2O_3 ceramics with high optical quality and large aperture sizes is possible. Because the mono-disperse single crystalline RE_2O_3s are chemically synthesized and sintered with much lower temperature [11] than the melting temperature, the defects introduced during the single crystal growth process can be almost negligible. The chemically synthesized powders of the single crystals can indicate the homogeneous distribution of the doping concentration. The nonlinear absorption which is the problem especially in highly Yb^{3+}-doped YAG maybe due to the concentration gradient can be significantly suppressed in the ceramic [12]. These advantages make ceramic as the suitable material for the high power/energy applications.

Not only investigating the thin-disk laser performances of the ceramic gain materials, but also developing the our original contacting method between the gain medium and the heat sink is important subject. The contacting quality between the gain medium and the heat sink is the key factor in the thin-

disk concept because it is seriously connected to the laser performances of the thin-disk lasers. Currently, only a part of German companies or universities, e.g. Trumpf GmbH [13], Dausinger + Giesen GmbH [14], and Institut für Strhalwerkzeuge (IFSW), Universität Stuttgart [15], can commercially provide the contacting of the gain medium on the heat sink with high quality, reliability, reproductivity and mass productivity. Almost all of the demonstrations of the thin-disk lasers/amplifiers use the thin-disk modules or disks with heat sinks provided by previously mentioned facilities. It means, Germany, where is the birthplace of the thin-disk concept, has the significant driving force in the thin-disk laser fields; in other words, the thin-disk technologies strongly depend on them. Several benefits: the reduced cost and time for the contacting, and the flexible experimental environment to handle the problem for the experiment, are obtained after the own contacting technique is established.

1.2 Outline

In this thesis, the potentials of the Yb:LuAG and Yb:Lu_2O_3 ceramics as the gain media for thin-disk lasers will be explored, and new contacting schemes and multi-pass pumping module will be developed. The mechanical, the thermal, and the spectroscopic properties of both ceramics are systematically measured first of all. The laser performances in the bulk-geometry are evaluated to get rid of the extra losses originated in the thin-disk concept itself. Then the thin-disk laser operations are demonstrated. Yb:LuAG ceramic thin-disks are contacted at the IFSW. The mounted disks are tested with the multi-pass pumping module also provided by the IFSW to evaluate the maximum laser performances. The thin-disk laser performances of Yb:LuAG ceramics are measured in the multi-mode regime, in the fundamental-mode regime, under the polarization control, and in the Q-switched regime. Yb:Lu_2O_3 ceramic thin-disks are contacted on the heat sink using the new contacting techniques. Several wavefront measurement systems are developed to measure the profile of contacted Yb:Lu_2O_3 ceramic thin-disks. Using the mounted disks and the multi-pass pumping module, the thin-disk laser operation is demonstrated. The thin-disk laser performances of Yb:Lu_2O_3 ceramics are evaluated in the multi-mode regime to check weather the disks work successfully without the damage and the instability. The temperature of the disk under lasing is measured with a thermographical camera as another qualification of the contacted disks.

The outline of the rest of this thesis is as follows.

In Chapter 2, general characteristics of the single crystal and ceramic as hosts for Yb^{3+}-doped gain media will be discussed. The crystallographic structures and state-of-arts regarding Yb:LuAG and Yb:Lu_2O_3, and Yb:YAG are compared.

Theories used in this thesis will be summarized in Chapter 3. The energy level of Yb^3 ion is assumed as a quasi-four level system. The background and design of the thin-disk concept will be discussed. Not only the conventional contacting technique is used but also the original contacting techniques are developed. The measurement and the analysis system to qualify the wavefront of the disks contacted with our techniques will be mentioned. The strategies for the resonator designs in both multi-mode and fundamental-mode regimes will be explained. With the Yb:LuAG ceramic thin-disk, the cavity-dumped active Q-switching is challenged. The basics and components of the Q-switch, and concept of the cavity-dumping will be introduced.

In Chapter 4, the properties and the laser performances of Yb:LuAG ceramic will be evaluated. The general properties and laser performances in the bulk-geometry of the 10 at.% Yb:LuAG ceramic are investigated in the former part in the Chapter. Then, the thin-disk lasers of Yb:LuAG ceramic in the multi-mode regime and the fundamental-mode regime are measured with conventional contacting technique and the multi-pass pumping module to evaluate the maximum performances. The thin-disk laser operation under the polarization control is checked to estimated the depolarization loss caused by the thermally-induced birefringence. Finally, the actively Q-switched laser operation as the preliminary step toward the regenerative amplifier is challenged.

In Chapter 5, the properties and the thin-disk laser experiments of Yb:Lu_2O_3 ceramics, our own contacting techniques, and constructed wavefront measurement and analysis system will be discussed. Same as is the case in Chapter 4, the general properties and the laser performances in the bulk-geometry is measured. The details of the developed multi-pass pumping module and of new contacting methods i.e. the soldering and the gluing will be mentioned. The profiles of the contacted disks are measured and analyzed with a combination of the Fourier-transform methods and the Zernike polynomials. The thin-disk laser experiments of the soldered and the glued 3 at.% Yb:Lu_2O_3 ceramics are demonstrated in the multi-mode regime. The temperature of the disks are measured with the thermographical camera.

Finally, this thesis is concluded and outlooks are introduced.

Chapter 2

Gain medium for thin-disk laser

2.1 Laser gain medium

Laser material (gain medium), the combination of the trivalent ion of the rare earth (RE) atom and the host material, is the absolutely necessary element for laser/amplifier architectures. For highly efficient, high power purposes, the trivalent ion of Ytterbium (Yb) is often employed due to its favorable operation scheme. The host material is also the important factor because it contributes significantly to determine the properties of the laser material. The performances of the lasers can be customized by selecting the host materials, and this is one of the advantage of the solid-state laser. In other words, the greatest attention has to be paid to the qualities and the features of the laser material because even small negative factors in laser material can easily affects the laser performances. The general characteristics of Yb^{3+}, and the single crystal and the ceramic host material are discussed.

2.1.1 Yb^{3+} ion as dopant

Yb is one of the lanthanide atom with the atomic number of 70. Its trivalent ion is promising for high power operation with high optical efficiency due to its unique energy level scheme. Figure 2.1 shows the energy level of Yb:YAG as an example [16]. It has only two energy levels: $^2F_{5/2}$ and $^2F_{7/2}$ whose manifold consist of three and four Stark sub-levels, respectively. The energy level scheme leads to the small quantum defect e.g. $\approx 8\%$ when the pump wavelength and the laser wavelength are 940 nm and 1030 nm, respectively. The absence of other energy levels excludes the harmful process for the laser operation such as the excited state absorption and quenching processes. Yb^{3+}

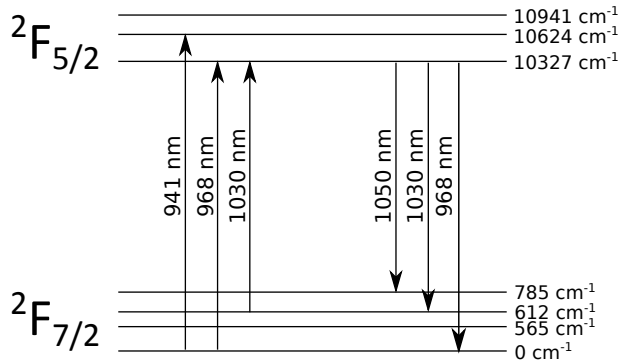

Fig. 2.1: Energy level of Yb:YAG [16].

ions also show the broader gain bandwidth compared with Nd^{3+} ion due to the electron-phonon coupling [17]. This is the advantage in wavelength tunable lasers and mode-locked lasers. Additionally, the long upper state life time of Yb^{3+} (typically 1 - 2 ms) enables a large energy storage and allows high energy extraction via the Q-switching.

The simple energy level scheme of Yb^{3+} ion requires the pumping with high pump power density. It causes the detrimental cooperative up-conversion processes such as the green emission by Yb^{3+}-Yb^{3+} pair and hopping to the charge transfer state of Yb^{2+} [12]. The latter limits the maximum doping concentration of Yb^{3+} and is a more sticky problem in the thin-disk concept because the heavy doping is favorable to improve the pump absorption and the gain.

2.1.2 Selection of host material

Currently, single crystals, glasses, and ceramics are mainly used as the hosts. Single crystals and ceramics indicate almost identical properties because ceramics is the polycrystal of the tiny single crystals. Glasses are the amorphous materials. Absence of lattice structure introduces broad gain bandwidth due to inhomogeneous broadening [18]. Additionally, producing glasses with large aperture size and high optical quality at a low cost is easily possible. But, the low thermal conductivity and the weak mechanical properties make glasses not suitable materials for high power/energy applications. For this reason, single crystals and ceramics can be the options for the thin-disk lasers. In both single crystals and ceramics, not all of them can be used as the laser host materials. The host material are desired to be transparent (colorless) at least around both pump and laser wavelengths. In addition, the cross-

sectional distribution of the refractive indices for the direction of the laser beam should be homogeneous to avoid wavefront distortions.

The crystal systems of single crystals are broadly classified into two categories: isotropic or anisotropic (see Table 2.1). The refractive index in Cartesian coordinates is given by

$$\frac{x^2}{n_x^2} + \frac{y^2}{n_y^2} + \frac{z^2}{n_z^2} = 1 \tag{2.1}$$

The host material is the dielectric transparent crystal, and thus its dielectric constant ϵ is related to the refractive index n [19] . If the crystal has equal ϵ for each direction, it means the refractive index is independent to the axis i.e. $n_x = n_y = n_z = 1$, it is called as "optically isotropic" crystal and only the crystal with a cubic structure can indicates the optical isotropy. Of course fabricating transparent ceramic with optically isotropic crystal can be possible due to its homogeneous refractive index. Other systems, where the crystal has different refractive indices, are called as "optically anisotropic" crystals. If all of the refractive indices are different ($n_x \neq n_y \neq n_z$), the crystal has two optical axes. Such kind of crystal is called "bi-axial". If the crystal has the relationship of the refractive index $n_x = n_y \neq n_z$, this crystal has one optical axis and is called "uni-axial". Here two refractive indices can be determined. One is the ordinary index $n_o = n_x = n_y$ and the other is the extraordinary index $n_e = n_z$. If $n_o < n_e$, the crystal has the positive birefringence, wheres if $n_o > n_e$, the crystal shows the negative birefringence. In such kind of cases, controlling the orientation of the crystal axis must be necessary for fabricating the transparent ceramic. Otherwise, the fabricated ceramic should become translucent.

2.2 Single crystal and ceramic

Yb^{3+}-doped single crystal and ceramic are important laser materials for current high power/energy laser applications. In the thin-disk laser sources, which

Table 2.1: Crystal system.

Optically isotropic	Optically anisotropic	
Cubic	Uni-axial -Tetragonal -Trigonal -Hexagonal	Bi-axial -Orthorhombic -Monoclinic -Triclinic

have the advantage in high power/energy extraction, the importance of single crystalline gain media are high whereas almost no thin-disk lasers based on ceramic gain medium. The difference in the activities would be originated in the natures of both hots materials. In this section, the basics of single crystal and ceramic and their current statuses as the hosts for the thin-disk gain media are discussed.

2.2.1 Single crystal as host material

Single crystal is the most traditional, and still the most popular host material due to its excellent optical, thermal and mechanical properties. It is the monocrystalline solid material whose crystal lattice is continuous, and hence has the possibility to grow the both the isotropic and the anisotropic transparent crystals with high optical qualities.

State-of-art

Various thin-disk lasers/amplifiers have been demonstrating with single crystalline gain materials. Recent remarkable results are summarized in Table 2.2. Yb:YAG single crystal holds the records for the highest CW output power per one disk [20], the highest average output power [21] and pulse energy [22] in the mode-locked operation, and the amplifiers with extremely high power/energy levels [23–27]. Currently, only Yb:YAG single crystal is used for the industrial applications though there are many gain materials with broad gain bandwidth. The reason is mainly due to the high reliability of Yb:YAG, i.e. the superior spectroscopic properties with high thermal and mechanical toughnesses, and easy growth of the crystal with large aperture size and the high optical quality by use of well optimized growing techniques. Other single crystalline materials, especially Yb^{3+}-doped RE_2O_3s have intensively been investigated due to their importance for ultrashort pulsed laser sources. Though the thin-disk laser operations based on Yb:RE_2O_3 with high average powers or short pulse durations have been demonstrated [28–30], the limitation in the maximum available aperture size of the grown RE_2O_3 single crystals due to the high melting temperatures of RE_2O_3 is the serious problem for further power scaling.

Disadvantages in single crystal

Single crystal is mainly grown from the melt or the liquid solution of the raw materials, e.g. the Czochralski (Cz) method [47] (Fig. 2.2). The growing process requires quite long time (typical growing rate $\approx$ mm/1hour) and

Table 2.2: State-of-art in the thin-disk concept with single crystalline gain materials. Recent demonstrations of CW lasers, mode-locked lasers, and amplifiers are summarized.

CW

Material	P_{out} (W)	η_{opt} (%)	η_{slope} (%)	Remarks	Ref.
Yb:YAG	10k			$M^2 = 110$	[20]
	4k			$M^2 = 1.38$	
Yb:LuAG	5k	61.9	71*		[2]
	742	58.5		$M^2 = 1.5$	[31]
Yb:Lu_2O_3	32.6	72	80		[32]
	670	66	80		[33]
	301	73	85		
Yb:$LuScO_3$	250	69	81		[34]
Yb:Sc_2O_3	264	70	80		
Yb:$LaSc_3(BO_3)_4$	≈ 0.5**	≈ 58**	64		[35]
	40	43	48		[36]

Mode-locked

Material	P_{avg} (W)	f_{rep} (MHz)	E_p (μJ)	τ (fs)	Remarks	Ref.
Yb:YAG	275	16.3	16.9	583	SESAM	[21]
	242	3.03	80	1,070	SESAM	[22]
	230	20	11.5	330	Kerr-lens	[37]
	17	40	1.1	200	Kerr-lens	[38]
	17	40	0.4	190***	Kerr-lens (positive)	[39]
Yb:Lu_2O_3	141	60	2.4	738	SESAM	[28]
	7	64	0.1	142	SESAM	
Yb:$LuScO_3$	5.1	77.5	0.07	96	SESAM	[30]
Yb:$(Lu,Y,Sc)_2O_3$	4.6	75	0.06	101	SESAM	
Yb:Lu_2O_3 Yb:Sc_2O_3	8.6	41.7	0.2	124	SESAM	[29]
dual gain	1.4			103		
Yb:$KY(WO_4)_2$	22	25	0.9	240	SESAM	[40]
	3.21	1	3	680	Cavity-dump	[41]
Yb:$KLu(WO_4)_2$	25.6	34.7	0.74	440	SESAM	[42]
	9.5			451	SESAM (positive)	
Yb:$KGd(WO_4)_2$	1.1	86.4	0.01	112	SESAM	[43]
Yb:$CaAlGdO_4$	5.1	65	0.8	62	SESAM	[44]
Yb:$YCa_4O(BO_3)_3$	2	19.7	0.1	270	SESAM	[45]
	4.7	24.4	0.2	455	SESAM	

Amplifier

Material	P_{avg} (W)	f_{rep} (Hz)	E_p (mJ)	τ (p s)	Remarks	Ref.
Yb:YAG	1327	300k	4.4	8	Multi-pass	[23]
		100	165	<2***	Regen.	[24]
			320		to Multi-pass	
	14k (intra burst)	100k (burst)	140 /pulse (80 pulse/burst)		Two disk cascaded	[25]
	300	10k	30	1.6	Regen.	[26]
	100	2k	50	1.7	Regen.	[27]
Yb:KYW	10	20k	0.5	185	Regen.	[46]

* the slope efficiency was measured in a different experiment with a low pump power.

** estimated value from the graph due to no values are described in the reference.

*** after pulse compression.

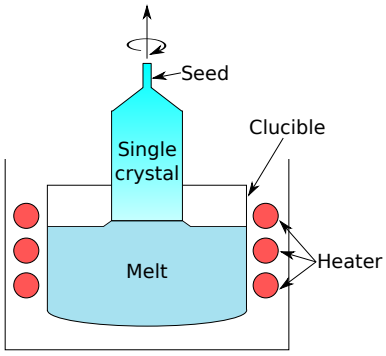

Fig. 2.2: Schematic of the Czochralski method.

the cost becomes high. Furthermore, growing single crystal with large aperture size and high optical quality is difficult due to some limitation factors and scattering sources. One obvious limitation factor is the crucible. Not only it limits the maximum available aperture size, but also can be introduce undesirable impurities which contaminate the melt of the raw materials and would introduce another phase inside the single crystal. Another limitation factor is density gradient caused by the change of the strength of the melt, and the stress strain. The strength of the melt or the liquid solution of the raw materials decreases or changes as the growth of the single crystal. It can leads to the spatial dependence of the refractive index which can degrade the wavefront. This can be avoided using the double crucible Cz method with automatic powder supply system. Some nonlinear crystals such as $LiTaO_3$ have been grown with the method [48]. The stress strain induced during and after the growing process can cause the dislocation and spatial fluctuation of the refractive index. Hence the wavefront has to be measured to chose the volume where no damage exists or the distortion of the wavefront is minimized when a laser rod is made.

Transition can be the additional serious problem when growing single crystal which has higher melting temperature than the phase transition temperature of such as RE_2O_3s. It makes the growth of such kinds of crystals with high optical qualities and large aperture sizes difficult [49]. Recently, the growth of sesquioxide single crystals with good optical quality fabricated using optimized heat exchanger method has been reported. The available aperture size and yield ratio seem to be still a problem [10].

These problems are relaxed in the thin-disk concept due to its short required length of the gain medium. Though homogeneity and no defects are

required in the radial direction, the requirement for the longitudinal direction is relaxed. The defects which can be the serious problems in the thin-disk concept would be the concentration gradient and the transition. The density gradient can be suppressed with the above mentioned method. However, when RE^{3+} is doped, controlling the doping concentration during the growing process becomes difficult. It can introduce the spatial fluctuation of the doping concentration, the clusters of RE^{3+} in other words, and hence can increase the non-radiative factors such as concentration quenching [50] and nonlinear loss [12]. Currently, the latter nonlinear loss, maybe due to the transition to the charge transfer state of Yb^{2+} caused by the increase of the Yb^{3+}-Yb^{3-} interaction rate, are serious problems in the thin-disk lasers based on the single crystalline materials with high doping concentration of Yb^{3+}.

2.2.2 Ceramic as host material

Ceramic is another option to overcome the weak point of both single crystal and glass. Advantages and disadvantages are simultaneously led by the nature of ceramic itself.

Background

There are three classification of ceramic.

1. Inorganic
2. Inorganic and non-metal
3. Inorganic, non-metal and sintered object

Here, the third definition is used to describe the ceramic. The usual "translucent" ceramics such as cups, dishes and so on have the flexibility in its shape and size with quite low cost. The great efforts have been paid to fabricate the "transparent" ceramic which can be used as the gain material.

The first demonstration of the hot-pressed Dy^{2+}:CaF_2 ceramic laser was reported in 1966 [51]. After the first report, there have been no additional laser demonstrations for several years. The second lasing was achieved in 1973 with Nd^{3+}:Y_2O_3 fabricated using the cold-press method [52]. However, reducing the losses in the ceramic was quite difficult, and then fabricating the ceramic with high optical quality was estimated to be almost impossible at this time. In 1995, the report regarding the hot-pressed Nd^{3+}:YAG demonstrated by Ikesue *et. al.* [53] changed the situation. Actually, though the efficiency was not so high compared with the present ceramic materials, the scattering losses in

their ceramic have been greatly reduced. In 1998, Ken-ichi Ueda and Takagimi Yanagitani have launched the collaboration research on the fabrication of the transparent ceramic, and have reported the Nd^{3+}:YAG ceramic fabricated using the nano-crystalline and the vacuum sintering technology [54]. This is actually the first report of the transparent ceramic fabricated using the non-reactive sintering method. In 2004, our Nd:YAG ceramic have indicated higher laser performance than that have been achieved with the single crystalline Nd:YAG [55].

Now the ceramic material becomes popular laser material in the bulk-geometry, but not popular in the thin-disk concept. There are only five demonstrations regarding the ceramic thin-disk lasers: two Yb:YAG ceramic thin-disk lasers in the CW regime [6, 12], the CW and the mode-locked operations of Yb:Y_2O_3 ceramic [7], Yb:LuAG ceramic thin-disk laser in the CW regime [8, 9], and Yb:Lu_2O_3 ceramic thin-disk laser in the CW regime [9]. Here refs. [8, 9] are our reports. To the best best of my knowledge, any reasons have not yet been reported. The nonlinear loss and the growth of single crystal with high melting temperature such as RE_2O_3 which are mentioned in Subsection 2.2.1 are the problems. These points can be resolved by the ceramic technology. Because the tiny crystals in the ceramic are prepared using the chemical synthesis in our case, the doping concentration of Yb^{3+} should be precisely controlled. High Yb^{3+}-doping can be possible in the ceramics. Additionally, the sintering temperature is much lower than the melting temperature. Thus, the fabrication of the RE_2O_3 ceramics with large aperture size and high quality become possible.

Scattering natures in ceramic

Below five factors (also described in Fig. 2.3) can be considered as the scattering natures in the ceramic [56].

(i). Surface scattering.

(ii). Refractive index modulation around the grain boundaries.

(iii). Defects such as pores inside tiny crystals and voids between grain boundaries.

(iv). Birefringence.

(v). Different phase between the grain boundaries.

Because the ceramic itself is polycrystal and most scatterings are occurred at the grain boundary, the ceramic can include large amount of scattering

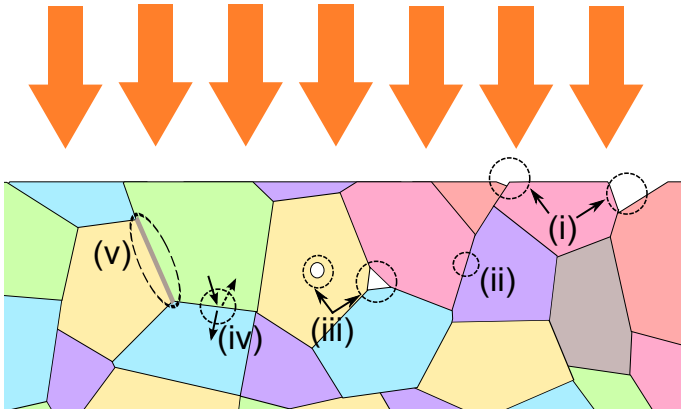

Fig. 2.3: Scattering natures in the ceramic. Five scattering sources, (i) surface scattering, (ii) refractive index modulation around the grain boundaries, (iii) defects such as pores inside tiny crystals and voids between grain boundaries, (iv) birefringence, (v) different phase between the grain boundaries, are proposed [56].

sources. Fabricating the transparent ceramic is equaled to make the clean grain boundary.

The differences between our fabrication method and former methods are uniformity of the size and purity of each tiny crystal. Since the ceramic fabricated using the former methods (classified as the reactive sintering method) is made from the oxide of each raw material (Al_2O_3, Y_2O_3, and Nd_2O_3, in case of Nd:YAG), the size of each tiny single crystal is large and the uniformity of the size are inhomogeneous [53]. Furthermore, each raw material reacts with each other and then Nd:YAG crystals are synthesized during the sintering process. In this process, keeping the stoichiometry condition is quite difficult. The small deviations from the stoichiometry point easily introduces additional defects such as the second phase, pores and so on [57]. In contrast, our fabrication method propsed by Konochima Chemical, which is classified as the non-reactive sintering method, enabled the fabrication of the ceramic with high optical quality [58, 59]. Because the chemically synthesized powder of the raw material is prepared, obtaining the very tiny and almost equal size of grains is possible. Konoshima Chemical also employs the vacuum sintering process which leads to the self-energy (surface tension) driven growth of the Nd:YAG crystals. In addition, slip casting process which does not require any pressing process dramatically reduces the static birefringence (almost nothing) inside the ceramic. Consequently, the fabrication the transparent ceramic with high optical qualities has been realized.

Fabrication of anisotropic ceramic

As discussed in Subsection 2.1.2, only the cubic system indicates no axis dependence of the refractive index and hence the fabrication of the ceramic is possible. In contrast, the anisotropic crystal has two (uni-axial) or three (bi-axial) refractive indices. The crystal axes of each tiny single crystal in the ceramic are randomly oriented (Fig. 2.4). It means, the laser beam meets different refractive indices crystal by crystal and is reflected at the grain boundaries. Thus, anisotropic ceramic becomes translucent even each tiny crystal in the ceramic is transparent.

In the book knowledge, the fabrication of the transparent anisotropic ceramic should not be possible. It has recently been demonstrated by adding the strong magnetic field [60]. T. Taira and his coworkers have reported the first demonstration of fabrication of Nd^{3+}- or Yb^{3+}-doped $Ca_5(PO_4)_3F$ (FAP) in 2009 [61], and have demonstrated the first laser oscillation of Nd:FAP in 2011 [62]. Though the laser performance is not so high due to not optimized fabrication process, it can be the key technology to broaden the possibility of ceramic materials.

Thermally-induced birefringence

Crystal with the cubic system indicates homogeneous distribution of the refractive index in the ideal condition. In practical situation, stress is accumulated during growing/fabrication processes, and is difficult to removed completely. Residual stress in crystal together with elasto-optic coefficients depends on the crystal axes introduce the different change of the refractive in-

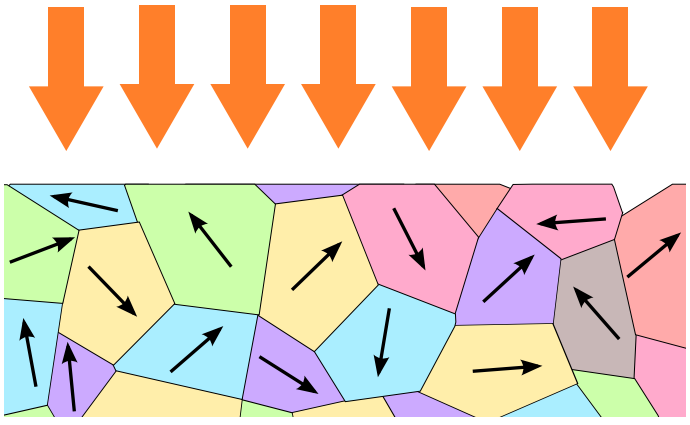

Fig. 2.4: Conceptual rendering of the orientation of the crystal axes inside the ceramic.

dices by crystal axes, i.e. static birefringence. This static birefringence is basically small enough to neglect in both single crystal and ceramic. Stress is not only occurred during growing/fabrication processes, but also induced thermally under laser operations. The temperature distribution inside the gain medium cause unequal thermal expansion which introduce thermal stress. Then birefringence is induced thermally. This thermal stress induced birefringence (thermally-induced birefringence [63]) can be a problem especially in the thin-disk shaped ceramic. Though the crystal axes are determined in single crystal, cannot be determined in ceramic due to its polycrystalline body (Fig. 2.4). Light passing through the ceramic experiences different birefringence grain by grain. It leads to the change of the polarization state (i.e. depolarization) of the light. If the thickness of the ceramic is enough thick, the depolarization effect can be averaged and is nearly the same as [111] direction of single crystal [63] . In case of the thin-disk shaped ceramic, the decrease of the thickness leads to the reduced number of the crystals which interact with the light. In such kind of cases, the spatial dependence of the polarization state can be appeared. When the ratio (thickness)/(average grain size) becomes smaller than 100, the probability to occur the spatial fluctuation of the polarization state becomes large [64]. This can lead to extra losses and the degradation of beam quality under polarization control, e.g. mode-locking and regenerative amplification.

2.3 Yb^{3+}-doped Lu-based oxides as gain media

In this thesis, Yb^{3+}-doped Lu-based oxides, especially Yb:LuAG and the Yb:Lu_2O_3 are chosen as the gain media due to their importances. Yb:LuAG is one of the most fascinating material because it indicates almost identical structure to that of Yb:YAG. Yb:Lu_2O_3 is another important material because its single crystal with the large aperture size and the high quality is quite difficult to grow. The properties and the current statuses of Yb:LuAG and Yb:Lu_2O_3 are compared to those of Yb:YAG.

2.3.1 Yb:$Y_3Al_5O_{12}$ versus Yb:$Lu_3Al_5O_{12}$ and Lu_2O_3

Crystal structure of YAG

Yb:YAG single crystal is the most traditional gain medium and is the most important gain medium for the many laser applications even now. Basic information of YAG are summarized in Table 2.3. Figure 2.5 is the crystal-

Table 2.3: Properties of single crystalline YAG, LuAG, and Lu_2O_3.

Material	$Y_3Al_5O_{12}$	$Lu_3Al_5O_{12}$	Lu_2O_3
Space group (Schönflies [65]/Hermann-Mauguin [66])	${O_h}^{10}$/Ia3d	${O_h}^{10}$/Ia3d	${T_h}^{7}$/Ia3
Symmetry [66]	Cubic	Cubic	Cubic
Site symmetry (Wycoff/Schönflies) for YAG & LuAG [67] for Lu_2O_3 [68]	Y^{3+} : 24(c)/D_2 $Al^{3+}1$: 16(a)/C_{3i} $Al^{3+}2$: 24(d)/ S_4 O^{2-} : 96(h)	Lu^{3+} : 24(c)/D_2 $Al^{3+}1$: 16(a)/C_{3i} $Al^{3+}2$: 24(d)/ S_4 O^{2-} : 96(h)	$Lu^{3+}1$: 8(b)/C_{3i} $Lu^{3+}2$: 24(d)/C_2 O^{2-} : 48(e)
Density (g/cm^3)	4.53 [69]	6.72 [69]	9.42 [66]
Lattice constant (Å)	12.008 [69]	11.916 [69]	10.391 [49]
Heat capacity (J/g·K)	0.603 [69]	0.411 [69]	0.256 [70]
Thermal diffusivity (10^{-6} m^2/s)	6.03 [69]	4.11 [69]	6.08 [71]
Thermal conductivity (W/m·K)	12.9 [69]	9.6 [69]	12.5 [49]
Melting point (K)	2,220 [66]	2,260 [66]	2,450 [49]
Mohs hardness	8.5 [72]	7.5 [66]	≈ 7 [49]
Elastic constants (10^{-11} N/m^2) [66]	C_{11} : 3.49 C_{12} : 1.21 C_{44} : 1.44	C_{11} : 3.39 C_{12} : 1.14 C_{44} : 1.13	N/A
Elasto-optic coefficient @633 nm [66]	p_{11} : -0.029 p_{12} : 0.0091 p_{44} : -0.0615 p_{12} : -0.038	N/A	N/A
Thermal expansion coefficient (10^{-6}/K)	6.14 [73]	6.13 [73]	5.5 [74]
Thermo-optic coefficient (10^{-6}/K)	7.8 [73]	8.3 [73]	8.18* [75]

* 1 at.% $YbLu_2O_3$ ceramic.

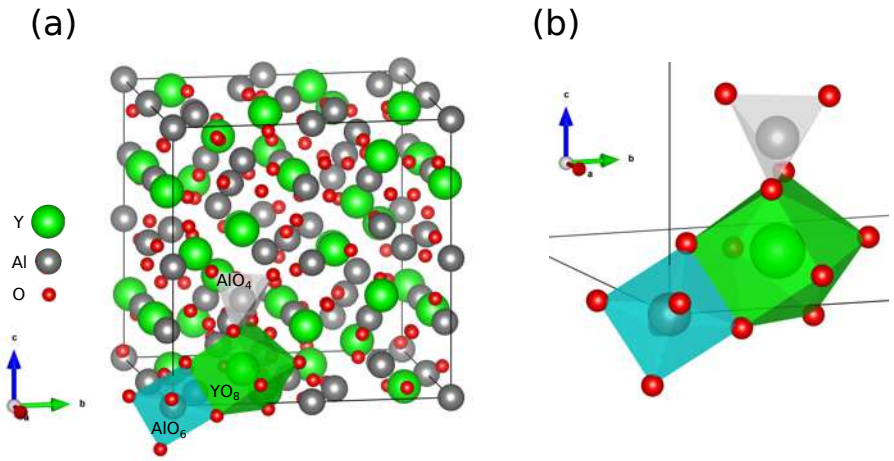

Fig. 2.5: Crystallographic structure of (a) unit cell of YAG and (b) three kinds of polyhedra.

lographic structure simulated using visualization for electronic and structural analysis (VESTA) [76] with the parameters described in Ref. [77] . YAG has the general garnet unit cell described as $A_3B^1{}_2B^2{}_3O_{12}$ with body-centered cubic structure (space group of Ia3d or $O^{10}{}_h$) with a lattice constant of 12.008 Å. 24 cations (Y^{3+}) locate at A site and occupy D_2 site. The Al^{3+} ions can be located at two different sites. 16 of which locate at $B^1{}_2$ site and occupy C_{3i} site, and 24 of which locate at $B^2{}_3$ site and occupy S_4 site. The oxygen anions (O^{2-}) occupy the remaining 96 positions, and thus the total number of atoms in the unit cell are 160.

State-of-art of Yb:YAG

The combination of the Yb:YAG single crystal and thin-disk geometry provides the many high power, high energy laser sources. In the CW regime, a maximum output power per one disk reaches 10 kW for multi-mode and 4 kW for near diffraction limited beam quality, and are commercially available [20]. The semiconductor saturable absorber mirror (SESAM) initiated passively mode-locked operation enables the direct extraction of the ulrtashort pulse with an energy level of μJ from the oscillator. Recently the SESAM mode-locking with an average power of 242 W and a pulse energy of 80 μJ has been demonstrated [22]. The Kerr-lens mode-locking in negative/positive dispersion regimes have also been demonstrated [38,39]. Very recently, the Kerr-lens mode locking with extremely high average power of 230 W and short pulsed duration of 330 fs have been demonstrated [37].

Crystallographic structure of LuAG

LuAG is also has the garnet structure, and thus indicates the same crystallographic structure as YAG with Y altered by Lu (see Fig. 2.5). The general properties of LuAG are summarized in Table 2.3.

State-of-art of Yb:LuAG

Yb:LuAG is one of gain materials with a great potential to alternate the conventional Yb:YAG due to its nearly identical spectroscopic and mechanical properties to Yb:YAG. The thermal management in Yb:LuAG can be more efficient compared with Yb:YAG due to its almost equal atomic mass of Lu (175 g/mol) to that of Yb (173 g/mol) [78]. Its tiny atomic mass difference leads to less phonon scattering compared with Yb:YAG whose substituted host atom of Y (88.9 g/mol), therefore high thermal conductivity under heavy doping situation can be achieved with Yb:LuAG. The first laser demonstration of Yb:LuAG single crystal was reported in 1976 [79]. Recently, Yb:LuAG single crystals with thin-disk geometry have recorded the output power of 5 kW in the multi-mode regime [2] and the output power of 742 W with a near diffraction limited beam quality [31]. The polycrystalline transparent Yb:LuAG ceramics have recently been investigated as novel gain media [80–82]. The highly efficient CW laser oscillation and the first femto-second mode-locked laser operation with bulk Yb:LuAG ceramic [81, 82], and the first demonstration and the highly efficient CW laser oscillation of the Yb:LuAG ceramic thin-disks [8, 9] have been reported. Here refs. [8, 9, 81, 82] are our reports. The multi-pass amplification has also been reported with the bulk-shaped Yb:LuAG ceramic [83].

Crystallographic structure of Lu_2O_3

Table 2.3 summarizes the general information and Fig. 2.6 shows crystallographic structure of Lu_2O_3 which also was generated using VESTA [76] with the parameters indicated in Ref. [84]. Lu_2O_3 has the body-centered cubic structure with two different cation (Lu^{3+}) sites and general anion (O^{2-}) sites. The lattice constant is 10.931 Å [49] with total numbers of atom of 80 per unit cell. Lu^{3+} can be located at C_2 site and C_{3i} with a ratio of 24:8. It means the electric dipole transition in quarter cation sites is inhibited, viz. Yb^{3+} ions located at the site cannot be luminescent (actually very weak transition can occur) due to the inversion-symmetry (C_{3i}) of the site.

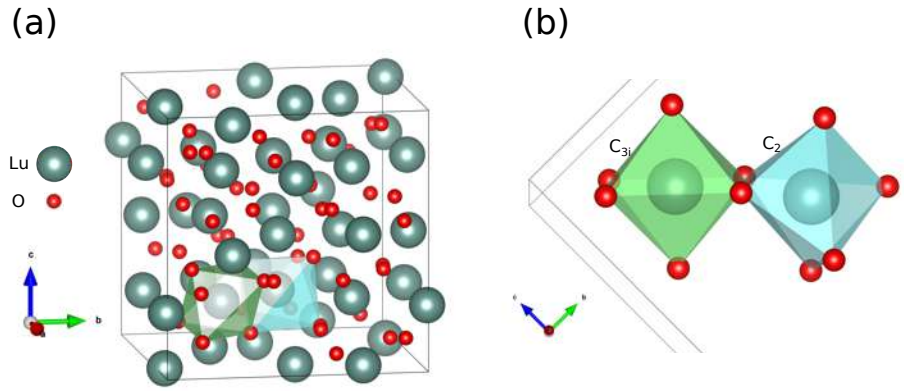

Fig. 2.6: Crystallographic structure of (a) unit cell of Lu_2O_3 and (b) two kinds of sites with C_2 and C_{3i} symmetries.

State-of-art of Yb:Lu_2O_3

Yb:Lu_2O_3, one of sesquioxides, is a suitable gain medium especially for ultrashort pulsed laser sources due to its broader gain bandwidth and higher thermal conductivity than those of Yb:YAG [3]. Due to the same reason as is the case in Yb:LuAG, Yb:Lu_2O_3 indicates high thermal conductivity at high Yb-doping concentration, and hence Yb:Lu_2O_3 have intensively been investigated in the thin-disk laser fields. For example, the SESAM-assisted mode-locking with the average power of 141 W [28], and the CW laser operation with the output power of 670 W [33] were demonstrated. The critical problem in Yb:RE_2O_3 is their high melting temperatures which summarized in Table 2.4. Those prevent the growth of Yb:RE_2O_3 single crystals with good optical qualities and large available aperture sizes. Recently, Yb:Lu_2O_3 single crystal grown with the optimized heat exchanger method demonstrated highly efficient thin-disk laser operation [10]. However, only small area of the grown single crystal can be used. The characteristic of the ceramic technology, i.e. lower sintering temperature than that of the melt growth, is an advantage in the fabrication of Yb:RE_2O_3 ceramics with high optical qualities and large available aperture sizes. Recently, Yb:Lu_2O_3 ceramics fabricated using not only our vacuum sintering and nanocrystalline technology [85], but also the hot-pressing have recorded the CW laser operation with high efficiencies [86].

Table 2.4: Melting points of sesquioxides and YAG [49].

	YAG	Y_2O_3	Sc_2O_3	Lu_2O_3
T_{melt} (°C)	1930	2430	2450	2430

Chapter 3

Theories

3.1 Quasi-four level scheme

3.1.1 Rate equations

Yb^{3+} ion has only two manifolds and thus the Yb^{3+}-doped gain medium exhibits quasi-three or quasi-four level performance. The Yb^{3+}-doped gain medium operates as a quasi-three level system if the pumping wavelength corresponds to the wavelength of the zero-phonon line of the gain medium. It operates as a quasi-four level system for other pumping wavelength typically 940 nm. Both quasi-three and quasi-four level system can be treated as the same rate equations.

Figure 3.1 shows the brief energy level structure of Yb^{3+} and the brief diagram of the quasi-four level system. The bold lines indicate the sub-levels which contribute the laser operation. The lower sub-levels $l1$ and $l2$ are the ground level and lower laser level, respectively. Likewise, $u2$ and $u1$ are the pump level and the upper laser level, respectively. The Yb^{3+} ions are exited to $u2$ by the pumping, then thermally relax to $u1$. After that, the exited ions emit the photons spontaneously if there is no photon which has the resonant frequency corresponds to the energy difference between upper manifold E_u and lower manifold E_l viz. $E_{ul} = E_u - E_l$, otherwise stimulated emission occurs if there are incident photons with the energy E_{ul}.

Let us consider the rate equation of the quasi-three level system with a total numbers of ions per an unit volume N_{tot}. Three transitions are assumed: the pump transition, the laser transition and the decay transition [87]. The

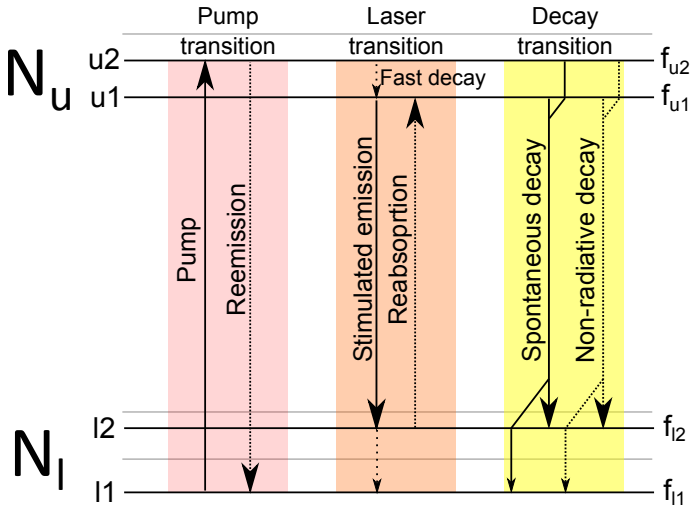

Fig. 3.1: Brief energy diagram of the quasi-three level system.

change of the upper state population N_u which equals to decrement of the lower state population N_l (since $N_{tot} = N_u + N_l$) can be written as

$$\frac{dN_u}{dt} = -\frac{dN_l}{dt} = W_{pump} - W_{laser} - W_{decay} \tag{3.1}$$

where W_{pump}, W_{laser}, W_{decay} describe the respective transition rates. Here, not only the transition process which are mentioned above, but also other transitions i.e. the reemission, the reabsorption and the non-radiative decay are assumed. Each transition rate is

$$W_{pump} = g_{abs,eff} \cdot \frac{P_p}{S_p} \cdot \frac{1}{h\nu_p} \tag{3.2}$$

$$W_{laser} = g_{emi,eff} \cdot \frac{P_l}{S_l} \cdot \frac{1}{h\nu_l} \tag{3.3}$$

$$W_{decay} = \frac{N_u}{\tau_{eff}} \tag{3.4}$$

where h is Planck's constant. P_p, S_p and ν_p are the power, the area and the frequency of the pump. Likewise, P_l, S_l and ν_l are the power, the mode area and the frequency of the laser. Therefore the term P_p/S_p and P_l/S_l describe the intensity of the pump I_p and that of the laser I_l, respectively. In Eqs. (3.2) and (3.3), the effective absorption gain coefficient $g_{abs,eff}$ and the

effective emission gain coefficient $g_{emi,eff}$ can be described as

$$\begin{aligned} g_{abs,eff} &= N_{tot} \cdot \sigma_{abs,eff} \\ &= \sigma_a^p N_l - \sigma_e^p N_u \qquad (3.5) \\ g_{emi,eff} &= N_{tot} \cdot \sigma_{emi,eff} \\ &= \sigma_e^l N_u - \sigma_a^l N_l \qquad (3.6) \end{aligned}$$

where $\sigma_{abs,eff}$ and $\sigma_{abs,eff}$ describe the effective absorption and emission cross sections, respectively. σ_a^p, σ_a^l, σ_e^p and σ_e^l are the absorption cross section at the pump and the laser wavelength, the emission cross section at the pump and the laser wavelengths. Each cross section is defined as an absorption cross section, a reabsorption cross section, a reemission cross section, and an emission cross section, respectively. In Eq. (3.4), τ_{eff} is the effective lifetime including the upper state lifetime (spontaneous lifetime) τ_{sp} and the non-radiative lifetime τ_{nr}. The inverse of the effective lifetime τ_{eff}^{-1} can be written as

$$\frac{1}{\tau_{eff}} = \frac{1}{\tau_{sp}} + \frac{1}{\tau_{nr}} \qquad (3.7)$$

In the case of Yb^{3+}, the probability of the non-radiative decay can be negligible ($\tau_{sp}^{-1} >> \tau_{nr}^{-1}$). Finally, Eqs. (3.2), (3.3), (3.4), (3.5), and (3.6) lead to

$$\begin{aligned} W_{pump} &= (\sigma_a^p N_l - \sigma_e^p N_u) \cdot \frac{I_p}{h\nu_p} \qquad (3.8) \\ W_{laser} &= (\sigma_e^l N_u - \sigma_a^l N_l) \cdot \frac{I_l}{h\nu_l} \qquad (3.9) \\ W_{decay} &= \frac{N_u}{\tau_{eff}} \qquad (3.10) \end{aligned}$$

3.1.2 Gain coefficient

In the steady state, Eqs. (3.1), (3.8), (3.10), and the steady state condition described as

$$\frac{dN_u}{dt} = 0 \qquad (3.11)$$

determines the population inversion factor $\beta = N_u/N_{tot}$ as a function of the pump and the laser power.

$$\beta(I_p, I_l) = \frac{\frac{I_l}{h\nu_l} \cdot \sigma_a^l + \frac{I_p}{h\nu_p} \cdot \sigma_a^p}{\frac{I_l}{h\nu_l}(\sigma_a^l + \sigma_e^l) + \frac{I_p}{h\nu_p}(\sigma_a^p + \sigma_e^p) + \frac{1}{\tau_{sp}}} \qquad (3.12)$$

By use of β, the gain coefficient $g(I_p, I_l) = g_{emi,eff}$ are given by

$$\begin{aligned} g(I_p, I_l) &= N_{tot}\{\beta\sigma_e^l - (1-\beta)\sigma_a^l\} \\ &= N_{tot}\left[\frac{(\frac{I_l}{h\nu_l}\cdot\sigma_a^l + \frac{I_p}{h\nu_p}\cdot\sigma_a^p)(\sigma_e^l - \sigma_a^l)}{\frac{I_l}{h\nu_l}(\sigma_a^l + \sigma_e^l) + \frac{I_p}{h\nu_p}(\sigma_a^p + \sigma_e^p) + \frac{1}{\tau_{sp}}} - \sigma_a^l\right] \end{aligned} \tag{3.13}$$

and the small signal gain coefficient $g_{ssg}(I_p, I_l \to 0)$ are given by

$$g_{ssg}(I_p, 0) = N_{tot}\left[\frac{\frac{I_p}{h\nu_p}\cdot\sigma_a^p(\sigma_e^l - \sigma_a^l)}{\frac{I_p}{h\nu_p}(\sigma_a^p + \sigma_e^p) + \frac{1}{\tau_{sp}}} - \sigma_a^l\right] \tag{3.14}$$

3.2 Thin-disk concept

3.2.1 Background

The thin-disk (sometimes called "active mirror") concept like Fig. 3.2, which was proposed in 1994 by Adolf Giesen [1], is nowadays the key technology especially for ultrashort pulsed laser/amplifier applications with high average power. The surface of the disk shaped gain medium with quite "thin"-thickness (typically 100 $\sim$ 300 μm) is contacted on the heat sink.

The difference between the thin-disk concept and conventional concepts (e.g. rod, slab) is the thermal treatment. In case of the rod- and the slab-shaped gain media, mainly the side cooling employed. It leads to the radial heat flow (Fig. 3.3). The length of the longitudinal direction of the gain

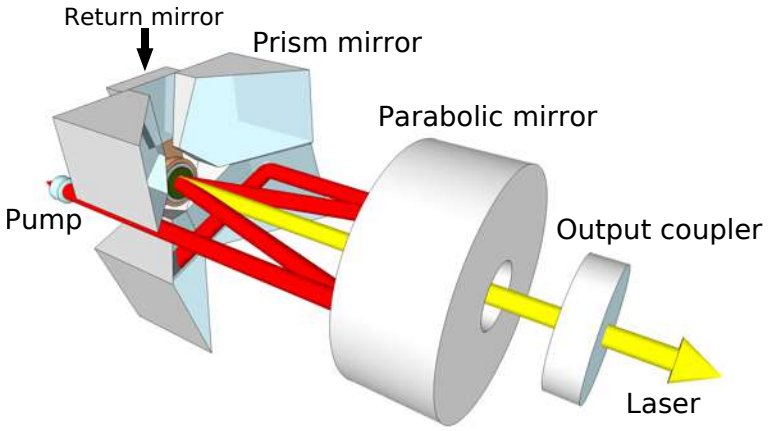

Fig. 3.2: Schematic of the thin-disk laser.

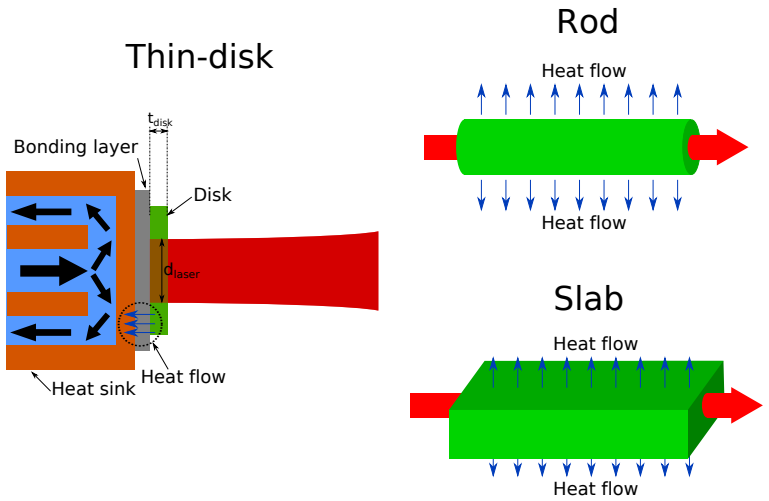

Fig. 3.3: Schematic of the thin-disk, rod, and bulk concepts.

medium becomes long (mm $\sim$ cm) compared with the pump diameter. Additionally, the pump beam has generally a Gaussian profile, and is focused inside the gain medium to increase the pump density. Then the strong thermo-optic distortions e.g. thermal lensing which are caused by the parabolic like thermal distribution inside the gain medium are occurred. These thermal issues always limit the maximum extractable power/energy, the beam quality and the maximum doping concentration of RE^{3+}.

In contrast, the thin-disk concept employs the end cooling. The cooling direction is parallel to the laser beam axis. It together with much shorter thickness of the disk than the diameter of the laser mode ($t_{disk} \ll d_{laser}$, see Fig. 3.3) and the almost flat-top (super-Gaussian shaped) pump spot distribution on the disk lead to the low temperature rising and the approximately one-dimensional temperature distribution in the gain medium.

Figure 3.4 describes the simple estimation of the temperature distribution inside the disk under an ideal condition with different thicknesses simulated using a Python codes. The disk with a diameter of 15 mm is assumed to be contacted on the copper heat sink without any additional coating layers and the contacting layer. The thermal conductivity and thermo-optic coefficient of 10 at.% Yb:LuAG ceramic described in Table. 2.3 are used as examples. The pump beam profiles is designed to be the 10th order super-Gaussian with the pump spot diameter of 10 mm and the pump density of 5 kW/cm^2. The pump power was assumed to be fully absorbed to the gain medium owing to the multi-pass pumping. 8% of the pump power, which corresponds to

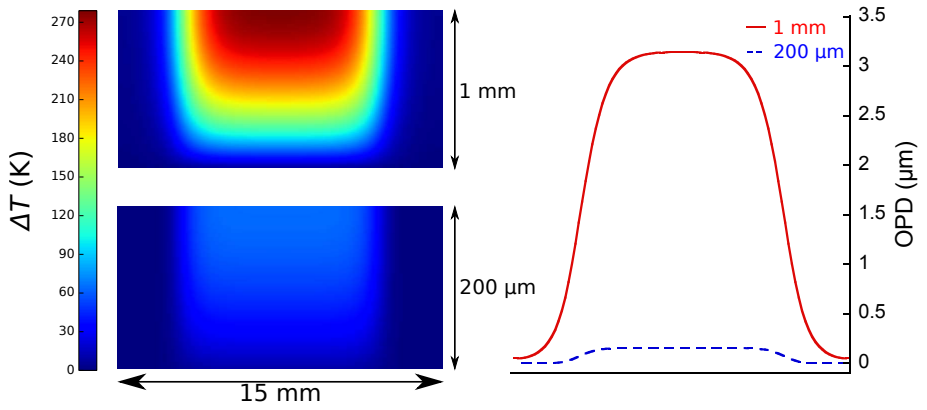

Fig. 3.4: Comparison of the temperature distribution inside the thin-disk with different thicknesses. The pump beam whose profile of 10th order super-Gaussian was assumed.

the quantum defect between the pump wavelength (940 nm) and the laser wavelength (1030 nm), is assumed to transfer to heat load.

The simulation derives the decrease of the thickness of the disk leads to the decline of the temperature rising and the rectangular like shape of the temperature distribution inside the disk. Likewise, the optical path difference (OPD) becomes smaller and rectangular like shape as a decrease of the thickness of the disk. Then the thermo-optic distortion can be greatly minimized with the thin-disk concept. Additionally, the thin-thickness (in other words, the short interaction length) of the gain medium and the relatively large pump spot or laser mode diameter introduces the small nonlinearity under high peak power operation. This is another advantage of the thin-disk concept for the high power/energy ultrashort pulsed laser operation.

The short thickness of the gain medium causes disadvantages, the small one pass pump absorption and gain. To improve the total pump absorption, usually a multi-pass pumping module is used (see Fig. 3.2) [88]. The collimated pump laser beam is focused on the disk by the parabolic mirror, then the incident pump laser beam is reflected by the HR coating on the back surface of the disk which is located at the focal point of the parabolic mirror, after that, the pump laser beam is re-collimated by the parabolic mirror. The pair of the prism mirrors reflect the re-collimated pump laser beam to rotate the position of the pump laser beam on the parabolic mirror. Repeating this

scheme, the pump laser beam is incident to the disk for many times (e.g. 24 passes) until the pump beam is completely absorbed. The multi-pass pumping leads to not only increase of the pump absorption, but also relaxation of the demands for the brightness of the pump source owing to the power scaling law in the thin-disk concept vis. increase the pump spot with keeping the pump density. Furthermore, the thin-disk concept enables easy extraction of the laser beam with near diffraction limited beam quality. Hence, the thin-disk concept can be recognized as a kind of brightness converter.

High RE^{3+}-doping is another way to improve not only the pump absorption but also the gain. However, the high RE^{3+}-doping has several serious problems. One is the rapid decline of the thermal conductivity. This phenomenon completely conflicts the thin-disk concept which aims to realize the efficient cooling and the minimization of the thermo-optic distortions. Another problem is increase of the nonlinear loss under the high doping and the high power pumping. Especially the single crystalline gain medium, currently mainly highly Yb^{3+}-doped YAG, suffers from the nonlinear loss maybe due to the increase of the Yb^{3+}-Yb^{3+} interaction rate. Above two problems can be avoided or relaxed with Lu-based ceramics due to the almost identical atomic mass of Lu^{3+} to Yb^{3+} and the possibility of the homogeneous doping concentration.

3.2.2 Contacting with disk and heat sink

The condition of the contacting layer between the disk and the heat sink is significantly affected to the various performances of the thin-disk laser. The contacting layer should have no defects (pores) and uniform thickness. Of course the thickness of the contacting layer should be as thin as possible. Now, two contacting schemes are mostly employed: the soldering and the gluing.

Soldering

The soldering method uses indium-based alloys such as gold-tin (Au-Sn) and indium-tin (In-Sn) as the solders. Since the disk itself is a non-metal material, an additional metal layer must be coated above the HR coating for the soldering. Generally, an Au layer is chosen as the additional metal layer because Au easily reacts with In [89].

Table 3.1 summarizes the properties of In-Sn solder and Au-Sn solder [90]. The shear strength which corresponds to the bond holding strength of the Au-

Sn is higher than that of the In-Sn. The thermal conductivity of the Au-Sn solder is also higher than that of the In-Sn. Hence, the better heat exhaustion and the more robust contacting can be possible with the Au-Sn solder. However, the Au-Sn solder would require the precise optimization and the control of the soldering process because it should not be flexible due to its high shear strength and thus the mitigation of the stress strain at the contacting layer can be difficult. In contrast, the In-Sn solder indicates the moderate shear strength and the low melting temperature. Therefore, the condition of the soldering process can be more relaxed with In-Sn solder. The disk soldered with In-Sn solder has the possibility to indicate large deformation by pumping, which causes the change of the TEM_{00} mode on the disk, and lower tolerance against to the temperature rising due to low melting temperature of the In-Sn solder.

Another point which should be noted is the chemical stability. In contrast to Au which is the stable metal, In is easily oxidized. When using the especially the In-Sn solder, a flux is necessary to remove the oxidized film and improve the solderability. Note that, some fluxes (especially acidity fluxes) have the possibility of corroding. Furthermore, avoiding evaporating of the flux which would introduce the pores and contaminates the disk and the contacting layer cannot be possible. From these point of view, the gluing method can be estimated to be much better than the soldering.

Table 3.1: Thermal and mechanical properties of the In-Sn and Au-Sn solders [90].

Solder	T_{melt} (°C)	K @ 85 °C (W/m·K)	Shear strength (PSI)
Au-Sn (80:20)	280	57	40,000
In-Sn (52:48)	118	34	1,630

Gluing

The gluing method uses the epoxy resin to contact the disk with the heat sink. The problems in the soldering can be avoided by using the epoxy resin. Its hardening process is driven by the cross-linking reaction which is accelerated by such as heating and lighting, then contacting a non-metal material with a metal material without additional layers becomes possible, and hence the contacting condition is further relaxed. Additionally, the hardening process is continuous and the hardening speed can be controlled by the temperature or the intensity of the light. It enables a fine tuning of the contacting condition

even during the hardening process, and further mitigation of the stress strain. The pollution of the disk should be also no problem in the gluing because now the epoxy resin for optical issues which has extremely low gas emission is commercially available.

One fatal problem is its very low thermal conductivity. The general epoxy resin indicate low thermal conductivity below 1 W/m·K [91]. However, it should not be a problem if the thickness of the contacting layer, the thermal resistance of the contacting layer in other words, becomes smaller than that of HR coating layer.

The thermal resistances R_{th}, defined as the ratio to the thickness of the material to the thermal conductivity of the material ($= l/K$ K/W), of the gluing layer and the soldering layer are calculated, and their dependences on the thickness are shown in Fig. 3.5. R_{th} of the HR coating, here 15 pairs of TiO_2/SiO_2 bi-layer are assumed, is indicated with the dotted line and cannot be reduced because decreasing the number of bi-layers causes decline of the reflectivity and narrowing of the reflection band. The used thermal

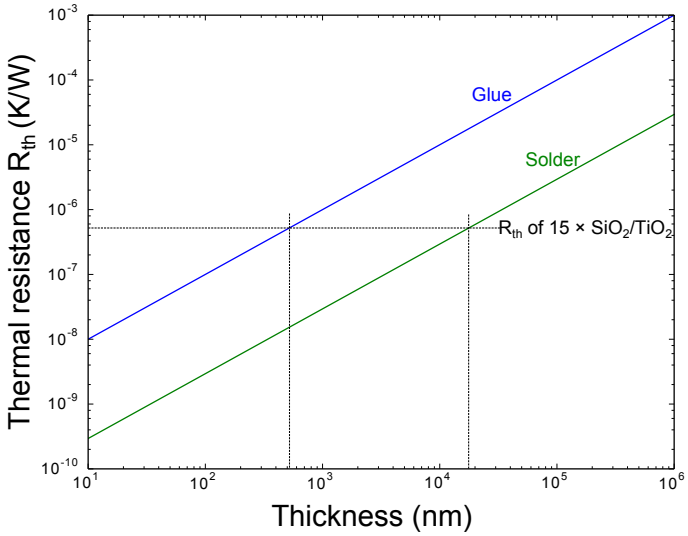

Fig. 3.5: Comparison of the thermal resistance between the HR coating and the contacting layers. Blue and green line indicate the thickness dependence of the thermal resistances of the gluing layer and the soldering layer. The thermal resistance of th HR coating (assumed 15 pairs of SiO_2/TiO_2 bi-layer) is shown in dotted line.

conductivity of the soldering layer is 34 W/m·K corresponding the thermal conductivity of the In-Sn solder, ant that of gluing layer is assumed to be 1 W/m·K. From this estimation, the HR layer becomes the thermal barrier if the thicknesses of the contacting layers are less than ≈20 μm and ≈ 500 nm, respectively.

Figure 3.6 shows again the simulated temperature profiles inside the whole disk with heat sink and using a Python code. The normalized heat flux profiles were calculated from simulated temperature profiles and are shown in Fig. 3.7. Different from Fig. 3.4, the coating layer and the contacting layer are included in the simulation. The thickness of the disk is set to be 200 μm. The coating layer is again 15 pairs of TiO_2/SiO_2 bi-layers. The thermal conductivities and thicknesses are averaged and summed and treated as one layer. Two cases of the thicknesses of soldering/gluing layers are shown: 50 μm and 10 μm for the soldering, and 1 μm and 300 nm for the gluing. As estimated from the calculation of the R_{th}, the soldered disk with 10 μm-thick soldering layer and the gluing disk with 300 nm-thick gluing layer, which have the almost same R_{th} as the coating layer, indicate similar temperature distributions. The reduction of the thickness of the contacting layer is effective to decrease the temperature rising. Further decrease of the thickness of the contacting layer than the thickness with the same thermal resistance as that of HR coating layer leads to the decline of the heat flux in the contacting layer and the heat sink. The HR coating layer becomes the thermal barrier after the thermal resistance of the contacting layer became smaller than that of HR coating.

Both soldering and gluing of course indicate similar temperature distribution under an ideal condition. In the practical situation, the gluing has the advantage in suppression of the temperature rising due to less extra absorption in the contacting layer. The absorption of the gluing layer is almost negligible due to the high optical transmittance together with the thin layer of the epoxy resin. For example, the epoxy resin named “301-2”which is used for the gluing in Chapter 5 has the transmittance of >99% with a spectral range of 400 ∼ 1200 nm. In contrast, the soldering requires the extra metal layers which has the absorption of an order of more than 10%. The metal layer increases not only the absorption, but also the thermal resistance.

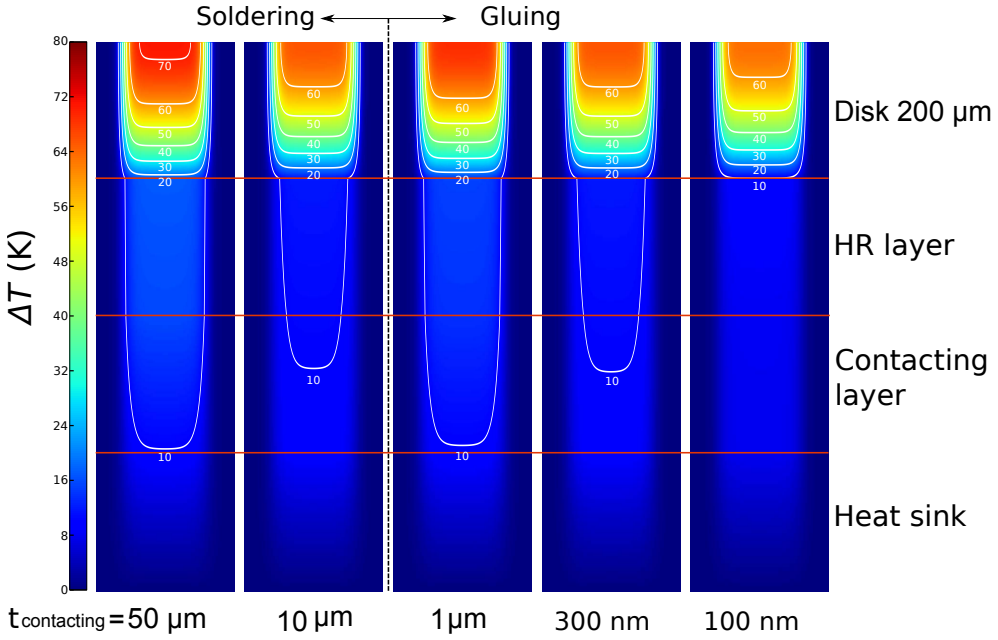

Fig. 3.6: Comparison of the temperature distribution with different thickness of the contacting layer.

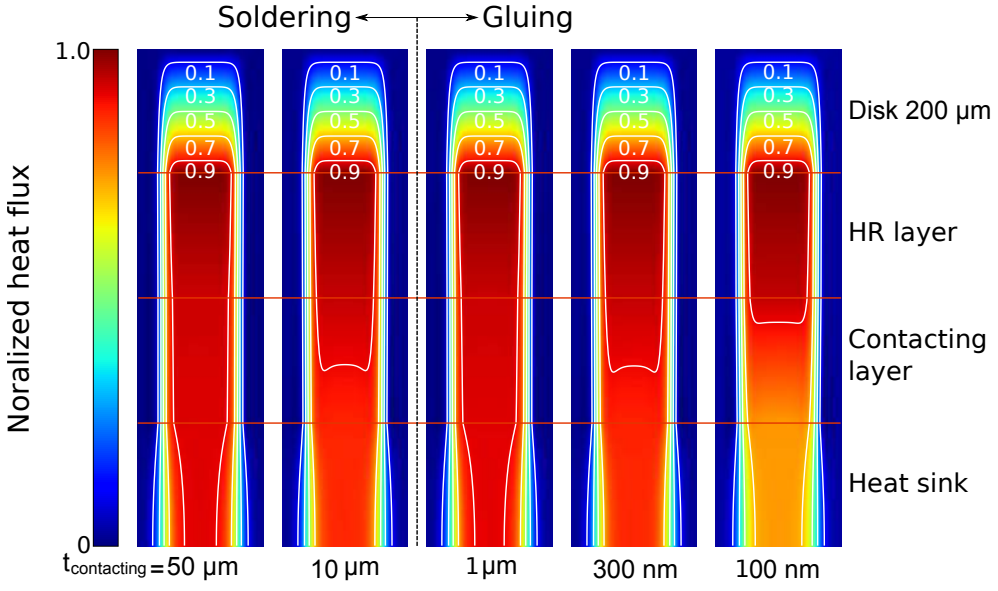

Fig. 3.7: Comparison of the normalized heat flux distribution with different thickness of the contacting layer.

3.3 Wavefront measurement

One simple way to test the bonding quality is trying the laser operation, and checking whether damages and instabilities occur or not. In terms of the main application for the thin-disk lasers, the laser mode on the disk is required to be controlled for a high brightness operation as mentioned in Section 3.5. The wavefront of a disk have to be clarified since the disk is also used as a mirror. The measurement method should be non-contact to avoid the damage to the disk. The interferometric measurement which is the most popular and reliable non-contact measurement would be the best choice. In this thesis, four interferometric techniques i.e. the Michelson interferometer (MI), the focus retro-collimated interferometer (FRCI), the phase shifting interferometer (PSI), and the Fourier-transform (FT) method are investigated to define which method is the most suitable for our requirement.

3.3.1 Interference

The MI which is the simplest and the most common interferometer is shown in Fig. 3.8 as an example. The probe light which has the temporal and spatial coherence is split by the beam splitter (BS), to one to the reference mirror and the other to the test surface. After both lights are reflected, these are overlapped and the interference pattern can be observed on the screen. Here, the electric field E_1 and E_2 on the screen from the reference mirror and the

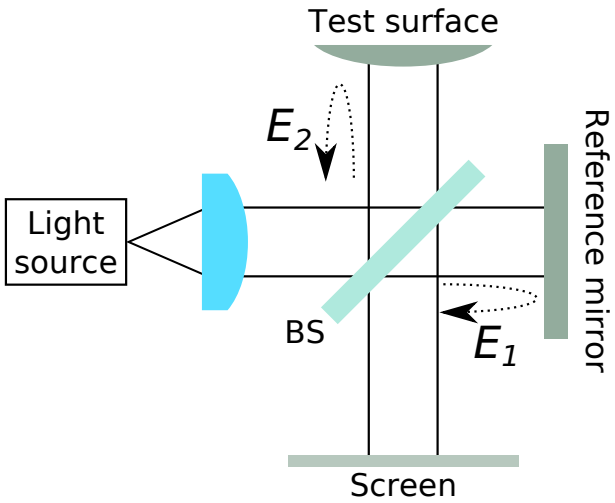

Fig. 3.8: Schematic of the Michelson interferometer.

test surface are respectively given by.

$$E_1 = A_1 \exp\{i(\phi_1 - \omega t)\} \tag{3.15}$$
$$E_2 = A_2 \exp\{i(\phi_2 - \omega t)\} \tag{3.16}$$

where A_1, A_2 are the amplitude of each electric field, ϕ_1, ϕ_2 are the phases, and ω is the angular frequency. The intensity of the interference pattern on the screen I can be calculated from the electric field on the screen $E = E_1 + E_2$

$$\begin{aligned} I &= \int E \cdot E^* dt \\ &= A_1^2 + A_2^2 + 2A_1A_2\cos(\phi_1 - \phi_2) \\ &= I_1^2 + I_2^2 + 2\sqrt{I_1 I_2}\cos(\phi_1 - \phi_2) \end{aligned} \tag{3.17}$$

where I_1, I_2 are the intensity of each electric field. Equation (3.17) indicates the pattern on the screen can be changed by the difference between ϕ_1 and ϕ_2. In other words, the phase information can be obtained from the interference pattern [92].

3.3.2 Michelson interferometer

Firstly, the MI shown in previous section was investigated to obtain the wavefront. One simplest way to characterize the disk is to obtain the radius of curvature (ROC) using Newton's rings shown in Fig. 3.9. The ROC R, the radial coordinate r, and the distance between the optical flat and the spherical surface d satisfy the approximately relation given by

$$d = \frac{r^2}{2R} \tag{3.18}$$

Additionally, the constructive and the destructive interference condition can be given by

$$\frac{r^2}{R} = \left(m + \frac{1}{2}\right)\lambda \tag{3.19}$$
$$\frac{r^2}{R} = m\lambda \tag{3.20}$$

$$\mathrm{m} = 0,\ 1,\ 2,\ \cdots$$

Using Eq. (3.18), (3.19), and (3.20), the ROC of the disk can be calculated [92]. However, this method should not be suitable for the measurement of the large ROC because at least two bright or dark rings are necessary. Additionally, it cannot be used if the disk has complicated surface.

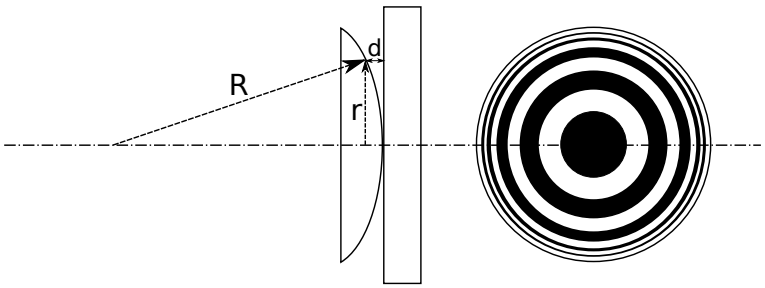

Fig. 3.9: Schematic of the Newton's ring.

3.3.3 Focus retro-collimated interferometer

The FRCI [93] is a more suitable technique for measurement of a long ROC. Its principle shown in Fig. 3.10 is based on Newton's formula. L is the lens whose focus points of F_1, F_2 with corresponding the focal length of f_1, f_2. The test surface which has the ROC R and the center of curvature O_2 is placed at the focus point F_2. Consider the case that the spherical wave with the ROC R is emitted from O_2. The beam is converged to O_1 where the slightly shifted point with the distance x from the focus point F_1, after passing through the lens. In the actual situation, the beam emitted from the O_1 focused on the test surface after passing through the lens. The beam is reflected by the test surface and focused at O_1 again after passing through the lens. Here, the relation ship between R, x, f_1, and f_2 can be given by

$$R = \frac{f_1 f_2}{x} \tag{3.21}$$

In practical situation, x is determined with an interferometer (see Fig. 3.11) and the below mentioned processes.

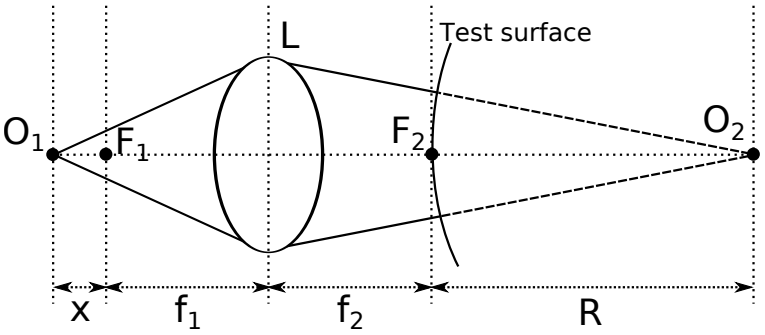

Fig. 3.10: Concept of the FRCI.

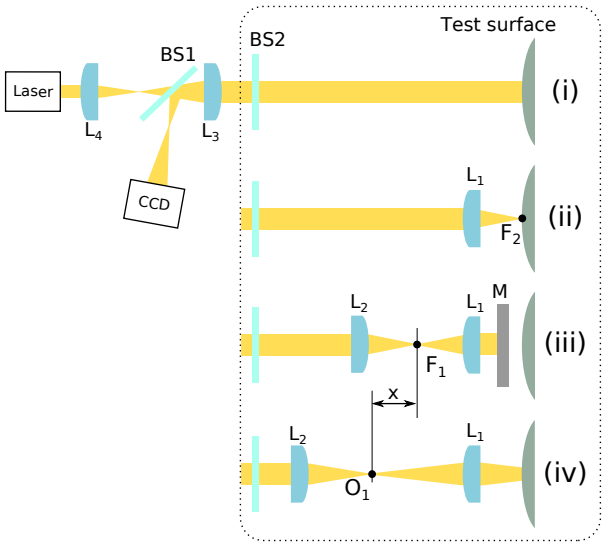

Fig. 3.11: Schematic drawing of the actual focus retro-collimated interferometer.

(i). The laser beam expanded by a pair of lenses L_3 and L_4 incident to the test surface without L_1 and L_2 to determine the position to be measured. A beam splitter BS1 reflects the interference pattern between the laser beam from a beam splitter BS2 as a reference surface and the test surface to the CCD.

(ii). A Lens L_1 is placed in front of the test surface with a same distance as the focal length f_1. The test surface is located at the position F_2 in Fig. 3.10. A cat's eye interference pattern should be observed.

(iii). A confocal system is formed by the plane mirror M inserted between L_1 and the test surface, lenses L_1 and L_2 to find the focus point F_1.

(iv). The retro-collimated point O_1 is then found by shifting L_2 to obtain the shift amount x.

Note that, the interference patterns on the CCD in process (ii) $\sim$ (iv) should indicates linearly-graded pattern if BS2 is slightly tilted.

In Fig. 3.11, both lenses L_1 and L_2 correspond to the lens L in Fig. 3.10. If the focal lengths f_1 and f_2 of L are the same ($f_1 = f_2 = f$), equation (3.21) can be modified as

$$R = \frac{f^2}{x} \tag{3.22}$$

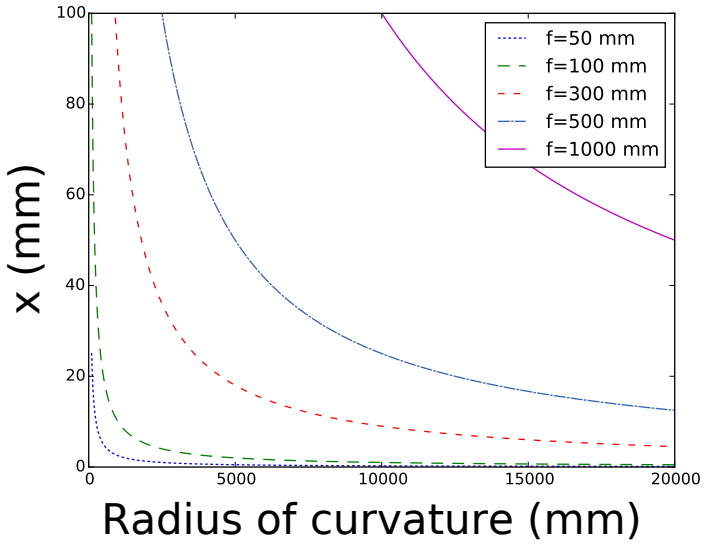

Fig. 3.12: Sensitivity and measurable radius of curvature with different lens pair.

The advantage of this measurement method is the flexibility of the the measurable range of the ROC and sensitivity by selecting f (Fig. 3.12). One obvious disadvantage of the method is the space management on the optical bench. The lens with a long focal length enables measurement of the long ROC while the large space is required. Another disadvantage is difficulty in observation of the wavefront other than the local ROC. Same as in the case of the MI, this method is not promising to measure the disk with a complicated surface.

3.3.4 Phase shifting interferometer

Observing the information other than the local ROC is difficult with FRCI. Therefore, the PSI [94] which enables the direct measurement of the phase is considered. In Eq. (3.17), when the further phase delay ϕ_i is introduced, Eq. (3.17) can be given by

$$\begin{aligned} I_i(x,y) &= I_1^2 + I_2^2 + 2\sqrt{I_1 I_2}\cos\left(\phi_1 - \phi_2 - \phi_i\right) \\ &= I_0 + I'\cos\left(\phi(x,y) - \phi_i\right) \end{aligned} \tag{3.23}$$

where $I_0 = I_1^2 + I_2^2$, $I' = 2\sqrt{I_1 I_2}$, and $\phi(x,y) = \phi_1 - \phi_2$ are introduced for simplicity. Four interference patterns with phase difference $\phi_i = 0, \frac{\pi}{2}, \pi, \frac{3\pi}{2} (i =$

$1, 2, 3, 4$) are assumed. Equation (3.23) can be written as

$$
\begin{aligned}
I_1 &= I_0 + I' \cos\left(\phi(x,y) - 0\right) && (3.24)\\
I_2 &= I_0 + I' \cos\left(\phi(x,y) - \frac{\pi}{2}\right) && (3.25)\\
I_3 &= I_0 + I' \cos\left(\phi(x,y) - \pi\right) && (3.26)\\
I_4 &= I_0 + I' \cos\left(\phi(x,y) - \frac{3\pi}{2}\right) && (3.27)
\end{aligned}
$$

The trigonometric terms can be changed as

$$
\begin{aligned}
I_1 &= I_0 + I' \cos\left(\phi(x,y)\right) && (3.28)\\
I_2 &= I_0 - I' \sin\left(\phi(x,y)\right) && (3.29)\\
I_3 &= I_0 - I' \cos\left(\phi(x,y)\right) && (3.30)\\
I_4 &= I_0 + I' \sin\left(\phi(x,y)\right) && (3.31)
\end{aligned}
$$

The intensity bias term I_0 can be eliminated by $I_4 - I_2$ and $I_1 - I_3$. Then, the phase $\phi(x, y)$ can be obtained by taking the ratio of the subtracted equations which can be written as

$$
\begin{aligned}
\frac{I_4 - I_2}{I_1 - I_3} &= \frac{\sin\left(\phi(x,u)\right)}{\cos(\phi(x,y))} \\
&= \tan(\phi(x,y)) && (3.32)
\end{aligned}
$$

Consequently, the phase $\phi(x, y)$ can be given by

$$
\phi(x,y) = \arctan\left(\frac{I_4 - I_2}{I_1 - I_3}\right) \tag{3.33}
$$

From the observed $\phi(x, y)$, the optical path difference (OPD) is given by

$$
\mathrm{OPD}(x,y) = \frac{\lambda}{2\pi}\phi(x,y) \tag{3.34}
$$

In this thesis, the algorithm which aims to reduce the phase error called Class B 5 bucket method [95] written as the below equation was employed.

$$
\phi(x,y) = \arctan\left(\frac{I_1 - 2I_2 - 2I_3 + 2I_4 + I_5}{I_1 + 2I_2 - 2I_3 - 2I_4 + I_5}\right) \tag{3.35}
$$

where I_5 is an additional interference pattern with a phase delay of 2π.

The serious problem in this method is accuracy of the phase shift. The actual measured interference pattern in Chapter 5 is a two-dimensional array

with the cross sectional size of 1000 pixel × 1000 pixel. The phase difference between each five interference pattern needs to be completely $\pi/2$ over all the pixels, otherwise, phase errors are introduced. A part of the interference pattern can be fluctuated due to such as the atmospheric turbulence, the vibration, and the hot pixel. Furthermore, the fluctuation can be significant and more active when measure the interference pattern under pumping. Therefore, the measurement method which is insensitive to the error of the phase shift, in other words, the one-shot measurement should be most promising for our requirement.

3.3.5 Fourier-transform method

The combination of the spatial heterodyne method and FT method [96] is considered as the one-shot wavefront measurement. The heterodyne method in the time domain which uses the temporal signal is commonly used method in the telecommunications field. In contrast to that, the spatial heterodyne method uses the spatial signal, viz. interference pattern. It introduces the spatial carrier frequency f_{0x} and f_{0y} instead of the phase delay ϕ_i. Equation (3.23) is modified as

$$\begin{aligned} I(x,y) &= I_0(x,y) + I' \cos(\phi(x,y) + 2\pi(f_{0x}x + f_{0y}y)) \\ &= I_0(x,y) + c\exp(2\pi i(f_{0x}x + f_{0y}y)) \\ &\qquad + c^* \exp(-2\pi i(f_{0x}x + f_{0y}y)) \\ c &= \frac{1}{2} I' \exp(i\phi(x,y)) \end{aligned} \tag{3.36}$$

Equation (3.36) means the reference mirror in the interferometer should be slightly tilted when the interference pattern is measured. Converting the interference pattern from the spatial domain to the frequency domain with Fourier-transformation, Eq. (3.36) can be converted as

$$\begin{aligned} I_{FT}(f_x, f_y) &= I_{0,FT}(f_x, f_y) + C(f_x - f_{0x}, f_y - f_{0y}) \\ &\qquad + C^*(-(f_x + f_{0x}), -(f_y + f_{0y})) \end{aligned} \tag{3.37}$$

Equation (3.37) indicates the bias component and the carrier components are separated. After the frequency domain spectrum is obtained, the unnecessary components such as the bias component, conjugation component, and additional noises are filtered, viz.

$$I_{FT}(f_x, f_y) = C(f_x - f_{0x}, f_y - f_{0y}) \tag{3.38}$$

Then the carrier frequencies f_{0x} and f_{0y} are removed by shifting the peak of the filtered spectrum to the original point. Finally, the phase $\phi(x, y)$ can be

obtained by inverse Fourier-transform (IFT) of Eq. (3.38)

$$I_{IFT}(x,y) = \frac{1}{2} I' \exp(i\phi(x,y)) \tag{3.39}$$

$$\phi(x,y) = \arctan\left[\frac{\Im(I_{IFT})}{\Re(I_{IFT})}\right] \tag{3.40}$$

This method can not only realize the highly accurate one-shot measurement, but also exclude the unnecessary noise components by the filtering.

3.4 Aberration analysis with Zernike circle polynomials

The next step after measurement of the wavefront is the quantification of the wavefront. One effective approach is analysis of the higher order aberrations using Zernike polynomials.

3.4.1 Definition

The Zernike circle polynomials $Z_n^m(\rho,\theta)$ [92] are described as the below equation

$$Z_n^m(\rho,\theta) = \begin{cases} \sqrt{\frac{2(n+1)}{1+\delta_{m0}}} R_n^{|m|}(\rho)\cos(m\theta) & : for\ m \geq 0 \\ -\sqrt{\frac{2(n+1)}{1+\delta_{m0}}} R_n^{|m|}(\rho)\sin(m\theta) & : for\ m < 0 \end{cases} \tag{3.41}$$

where $R_n^{|m|}(\rho)$ is given by

$$R_n^{|m|}(\rho) = \sum_{s=0}^{(n-|m|)/2} \frac{(-1)^s (n-s)!}{s!(\frac{n+|m|}{2}-s)!(\frac{n-|m|}{2}-s)!} \rho^{n-2s} \tag{3.42}$$

where n is the highest order of the radial polynomial and m is the azimuthal frequency. n and m are integers including zero, and always have to satisfy $n-m \geq 0$ and even. δ_{m0} is the Kronecker delta, i.e. $\delta_{m0} = 1$ when $m = 0$, otherwise $\delta_{m0} = 0$. ρ describes the radial coordinate. Here, the polynomial ordering number j is introduced for simplicity [97]. Then Eq. (3.41) can be modified as

$$Z_{j,even}(\rho,\theta) = \sqrt{2(n+1)} R_n^{|m|}(\rho)\cos(m\theta) : m \neq 0 \tag{3.43}$$

$$Z_{j,odd}(\rho,\theta) = \sqrt{2(n+1)} R_n^{|m|}(\rho)\sin(m\theta) : m \neq 0 \tag{3.44}$$

$$Z_j(\rho,\theta) = \sqrt{n+1} R_n^0(\rho) \quad : m = 0 \tag{3.45}$$

$$j = \frac{n(n+2)+m}{2}$$

Using above equations, each Zernike mode is generated with a Python code. Generated 1st $\sim$ 21st Zernike modes are indicated in Fig. 3.13

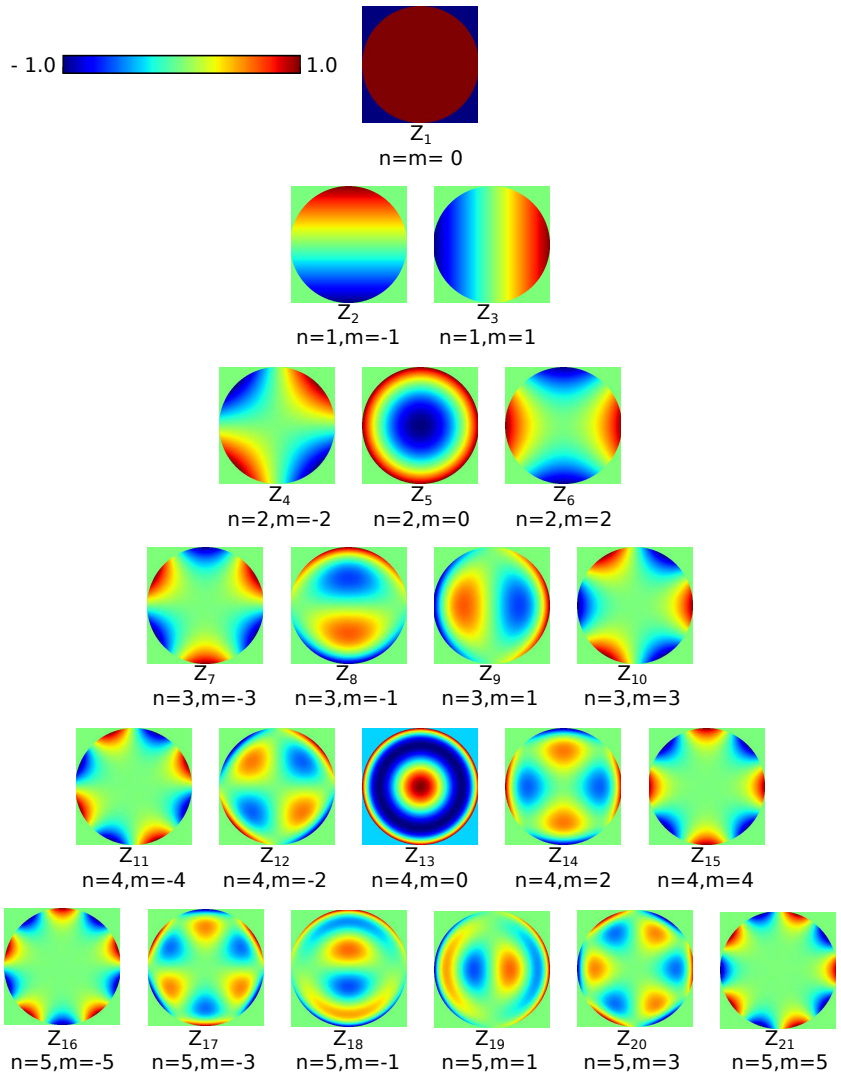

Fig. 3.13: Computer generated Zernike modes.

3.4.2 Zernike fitting

Using above discussed Zernike circle polynomials, the wavefront (the aberrations) can be described as the linear combination of each Zernike circle

polynomials

$$\begin{aligned}\phi(\rho,\theta) &= \sum_{n=0}^{N}\sum_{m=0}^{n} a_{nm} Z_n^m(\rho,\theta) \\ &= \sum_{j}^{N} a_j Z_j \end{aligned} \tag{3.46}$$

The quantification of the aberrations can be possible by obtaining the amplitude a_j which is only the unknown value because $\phi(\rho,\theta)$ is already observed as the two dimensional numerical map and Z_j can be programmatically generated. Taking the inner products of both sides of Eq. (3.46) with the generated Zernike circle polynomials $Z_1 \sim Z_N$

$$\begin{aligned} <\phi, Z_1> &= a_1 <Z_1, Z_1> \\ &\vdots \\ <\phi, Z_N> &= a_N <Z_N, Z_N> \end{aligned}$$

Because the above equation can be considered as a matrix equation described as

$$\begin{pmatrix} <\phi, Z_1> \\ \vdots \\ <\phi, Z_N> \end{pmatrix} = \begin{pmatrix} a_1 \\ \vdots \\ a_N \end{pmatrix} \begin{pmatrix} <Z_1, Z_1> \\ \vdots \\ <Z_N, Z_N> \end{pmatrix} \tag{3.47}$$

Then a_j can be calculated by making the inverse matrix of the latter part of the right side in Eq. (3.47)

$$\begin{pmatrix} a_1 \\ \vdots \\ a_N \end{pmatrix} = \begin{pmatrix} <\phi, Z_1> \\ \vdots \\ <\phi, Z_N> \end{pmatrix} \begin{pmatrix} <Z_1, Z_1> \\ \vdots \\ <Z_N, Z_N> \end{pmatrix}^{-1} \tag{3.48}$$

3.5 Resonator design

In SSLs, the propagation of the transverse mode in the resonator, especially inside the gain medium is important because the oscillated laser mode can be determined by the overlapping between the pump laser beam and the transverse mode determines the output laser mode.The propagation of the TEM_{00} mode (viz. the fundamental-mode) in the resonator is calculated with the ABCD-law [19]. In the transverse mode with the rectangular symmetry

(Hermite-Gaussian mode), the radius of the TEM_{mn} mode for the horizontal direction ω_m or for the vertical direction ω_n at the waist point is described as

$$\omega_i = \omega_0\sqrt{2i+1} \tag{3.49}$$

where i indicates m or n $(= 0, 1, 2\cdots)$ and ω_0 indicates the calculated radius of the fundamental-mode at the waist point. The radius of the TEM_{mn} mode at the arbitrary position in the resonator z is given by

$$\begin{aligned}\omega_i(z) &= w_i \cdot \sqrt{1+\left(\frac{z}{z_0}\right)^2} \\ &= \omega_0\sqrt{2i+1}\cdot\sqrt{1+\left(\frac{z}{z_0}\right)^2}\end{aligned} \tag{3.50}$$

where z_0 is the Rayleigh length defined as

$$z_0 = \frac{\pi\omega_0^2}{\lambda} \tag{3.51}$$

where λ is the wavelength of the laser [98]. Equations (3.49) $\sim$ (3.51) describe the higher order transverse mode has $\sqrt{2i+1}$ times larger radius than that of the fundamental-mode around the waist point (inside the gain medium).

In case of most SSLs with rod-shaped gain media, the Gaussian-shaped pump laser beam is generally employed to maximize the gain for the fundamental-mode.. The thin-disk concept uses the pump laser with the beam profile of nearby the top-flat (the super Gaussian) in terms of the thermal management. The radius of the fundamental-mode on the disk-shaped gain medium should be slightly smaller than that of pump spot diameter to improve the gain for the fundamental-mode. Figure 3.14 indicates the beam profiles for the pump laser (10th order super-Gaussian shape is assumed), the fundamental-mode, and the TEM_{10} mode as an example. If the profile of the pump laser is completely top-flat and the diameter of the fundamental-mode at $1/e^2$ is equal to the pump spot diameter, the overlapping ratios of the fundamental-mode and the TEM_{10} mode with the pump spot are $\approx 96\%$ and $\approx 75\%$, respectively. The gain for the TEM_{10} mode is expected to be enough low to suppress the oscillation. The gain for the fundamental-mode is considered to be not optimum because there are the skirt parts without the gain. In addition to that, the actual profile of the pump beam is super-Gaussian as indicated in Fig. 3.14. In terms of the improvement of the gain for the fundamental-mode, the optimum radius of the fundamental-mode is considered to be $\approx 80\%$ of the radius of the pump spot. It leads to the increased overlapped areas of $\approx 99\%$ and $\approx$

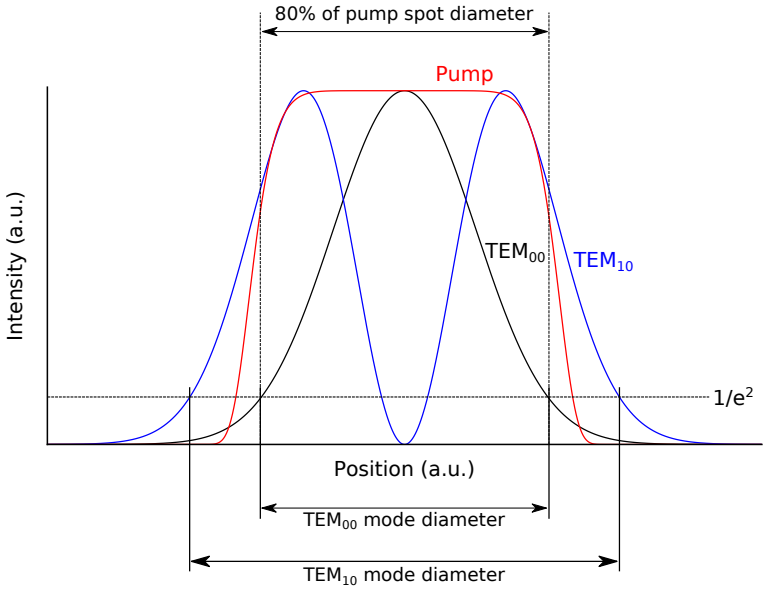

Fig. 3.14: Beam profiles for the pump laser (red curve, 10th order super-Gaussian shape is assumed), TEM_{00} mode (black curve), and TEM_{10} mode (blue curve).

90% for the fundamental-mode and the TEM_{10} mode, respectively. Further shrinking of the fundamental-mode size will increase the risk to oscillate the higher order modes.

The opposite procedure of above method is adopted to the design of the multi-mode resonator. Smaller size of the fundamental-mode on the disk allows to oscillate the higher order modes. The general ways to reduce the size of the fundamental-mode are shorten the resonator length or using the concave optics with the small ROC as the resonator optics. Note that sometimes larger resonator modes than the pump spot appear due to enough gain for the modes to oscillate. Such kinds of modes cannot contributed to the efficient laser operation due to no gain for the outer part of the modes. The resonator length or the ROC of the concave optics should be determined experimentally to explore the optimum size of the fundamental-mode on the disk which well suppresses TEM_{mn} modes with larger size than the pump spot. The designs for all of the thin-disk laser resonators operating in the multi-mode regime in this thesis are based on the above mentioned recipe.

3.6 Cavity-dumped active Q-switching

Q-switching which first demonstration was reported in 1961 [99] is one of the techniques to generate a short pulse with high energy (giant pulse) by intra-cavity loss modulation, i.e. modulation of the cavity Q [100]. Compared with the mode-locking technique, the Q-switching mainly covers the pulse duration in a nano-second regime and a repetition rate in Hz $\sim$ kHz regime. Its lower repetition frequency enables easy generation of a pulse with an energy level of mJ $\sim$ J, and hence Q-switched laser sources have a large benefit in industrial applications such as laser deposition [101], laser peening [102], laser ablation [103], and so on. However, due to the high level of the pulse energy, heat removal from the gain medium, which is the most serious problem in conventional SSLs, should become most important subject not only to avoid the damage, but also for stable operation. The thin-disk concept should be the solution to realize the high energy pulsed operation with a excellent thermal treatment. In this thesis, active Q-switching, especially a cavity-dumped active Q-switching technique is employed because it can become a regenerative amplifier by introducing a seed pulse.

3.6.1 Active Q-switching

The brief diagram of the active Q-switching is described as below and in Fig. 3.15.

1. The gain medium is pumped, but the laser cannot be oscillated due to large intra-cavity loss (low Q state) introduced by a combination of a PC and a quarter-wave plate (QWP).

2. During the low Q state, the gain reaches the saturation.

3. When the induced loss is suddenly removed or reduced to very small level (high Q state), the quick builds up of the pulse is initiated from the spontaneous emission noise.

4. The gain is reduced with the growth of the pulse, and the pulse reaches to the peak when the gain becomes equal to the total resonator loss.

5. The pulse is diminished quickly because the total resonator loss becomes larger than the gain.

The active loss modulation is generally introduced by a mechanical switch such as a mechanical chopper [104], a rotating prism [105] and a rotating mirror [106], or by inserting a modulator such as an acousto-optic modulator

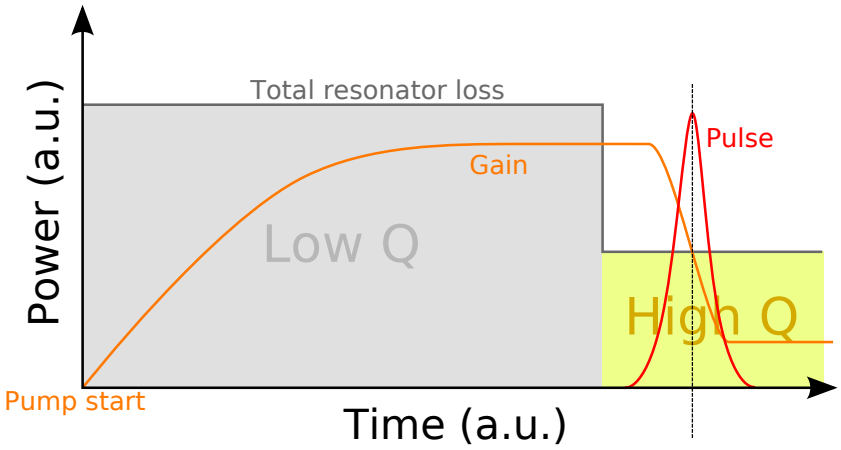

Fig. 3.15: Brief diagram of active Q-switching.

(AOM) [107] and an eletctro-optic modulator (EOM) [108]. In Chapter 4, the EOM is chosen since the EOM is more suitable for a high energy operation, and constructing a thin-disk regenerative amplifier is planed after evaluating the performances of the Q-switched thin-disk laser operation.

3.6.2 Q-switch

Since the main applications of the pulsed thin-disk laser such as Q-switch and regenerative amplifier are high energy (high average power) laser sources, a β-BaB_2O_4 (BBO) Pockels-cell (PC) is selected. It offers a high damage threshold of $>$ 3 GW/cm^2 for the pulse width of 1 ns at 1064 nm and the average power levels of hundreds of watts (several kW/cm^2 in power density) [110]. However, the low electro-optic coefficient of BBO requires high quarter or half wave voltage has to be applied. In addition, expanding the beam diameter is necessary for power scaling. It means, the aperture size of the Pockels-cell should also be increased, and hence further increase of the applied voltage is required because the necessary voltage is proportional to the aperture size.

In this thesis, a β-BBO (provided by LEYSOP LTD.) with the cross section of 8 mm $\times$ 8mm and the length of 20 mm whose quarter-wave voltage of $\approx$ 9 kV was chosen. To generate such kind of high voltage, the bipolar push-pull (bpp) circuit was offered. Figure 3.16 shows the principle of the offered bpp circuit (PCD-bpp, BME Bergumann) [109]. On A and On B switches are connected to the positive side (+HV) and negative side (-HV) of the high voltage, respectively, and both Off A and Off B are connected to the ground (GND). If On A switch is tuned on, the Off A switch is turned off

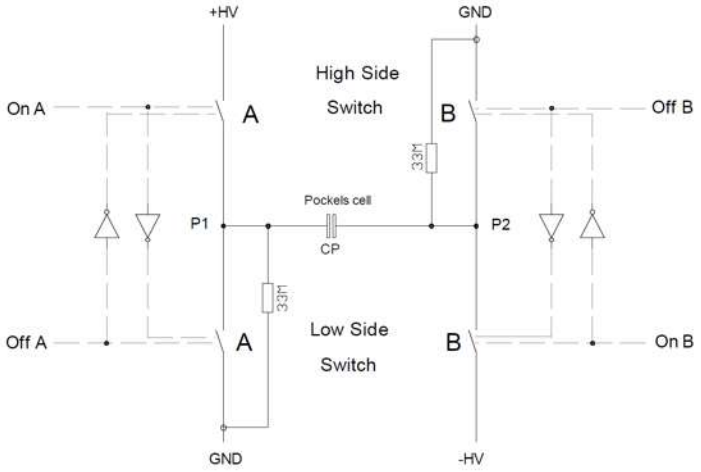

Fig. 3.16: Circuit diagram of the bpp circuit [109].

synchronously. Likewise, On A switch is turned on when Off A switch is turned off. On B and Off B switches operate as the switches on the A side. At least 3 V (> 4 V is better) with the pulse width of > 100 ns is required to turn on each switch. The input impedance should be 50 Ω. Here, the shortest time difference between On A and Off A (On B and Off B) is allowed to be 30 ns. The switch might be damaged if the time difference is set to be shorter time difference. With this configuration, the circuit enables to apply a doubled voltage (2HV) on to the terminals of the Pockels-cell by closing On A and On B, Off A and Off B switches at the same time. This operation scheme has advantages of not only the generation of the high voltage but also the relaxation of the stress on the terminals due to the high voltage.

3.6.3 Cavity dumping

The cavity dumping [111] is one of the techniques for pulse generation systems such as Q-switching, mode-locking, and regenerative amplification. It is achieved by controlling the polarization state of the intra-cavity pulse with the combination of a QWP, a thin-film polarizer (TFP), and a PC. The diagram of the cavity dumping is described as below, and its schematic is shown in Fig. 3.17.

1. No voltage is applied to the PC (Fig. 3.17 (a)).
   The PC just acts as the transmitting material. Only the QWP introduces a phase retardation. A horizontally polarized light is rotated to a vertically polarized light and vise versa. This introduces the transmit-

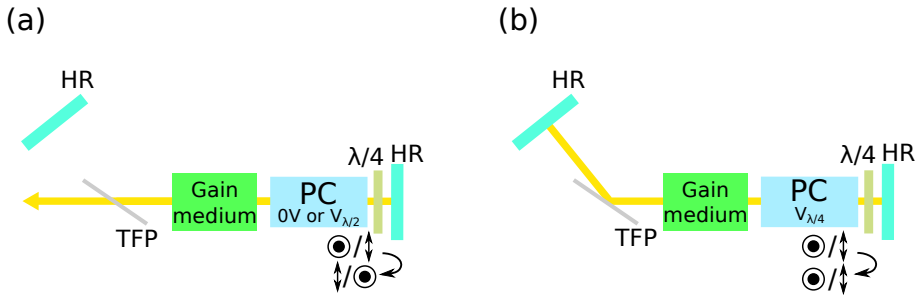

Fig. 3.17: Schematic of the cavity dumping. (a) 0 or half-wave voltage is applied. These lead to a dumping phase. (b) Quarter-wave voltage is applied. This leads to an amplification phase.

tance at the TFP of ≈ 100% (low Q state).Therefore the pulse cannot circulate inside the resonator due to the polarization selection at the TFP.

2. Quarter-wave voltage is applied to the PC (amplification phase, Fig. 3.17 (b)).
   Additional quarter-wave retardation is introduced by the PC. The transmittance at the TFP is decreased to ≈ 0% (high Q state).Then the linearly polarized light, generally the s-polarized light, is reflected and circulating inside the resonator. The pulse started from the noise is amplified during the quarter-wave voltage is applied. The time is called "amplification time" in this thesis.

3. No voltage or half-wave voltage is applied to the PC (Fig. 3.17 (a)).
   The phase retardation introduced by the PC becomes 0° or 90°. The transmittance at the TFP is again increased to ≈ 100%(low Q state).The amplified pulse is extracted from the resonator.

Chapter 4

Yb:$Lu_3Al_5O_{12}$ ceramics

4.1 Basic properties of Yb:$Lu_3Al_5O_{12}$ ceramic

Yb:LuAG ceramic is a promising gain medium for high energy applications due to its high thermal conductivity at high doping concentration and its high gain. The general properties and the laser performances in the bulk-concept are discussed.

4.1.1 Mechanical properties

Un-doped and Yb^{3+}-doped $Lu_3Al_5O_{12}$ (LuAG) ceramics were fabricated using the vacuum sintering and nano-crystalline technology [58,59]. The fabrication was the collaboration work with Konoshima Chemical Figure 4.1 shows the scanning electron microscope (SEM) images of the un-doped LuAG ceramics. Clear LuAG nano-crystals with tiny, and almost uniform size are densified.

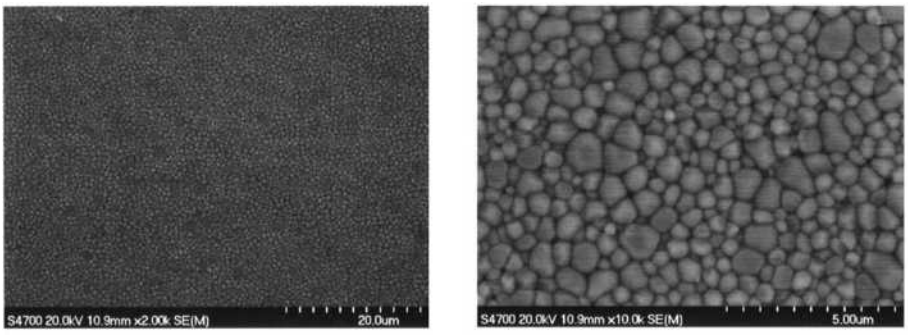

Fig. 4.1: SEM images of un-doped LuAG ceramics.

Table 4.1: Average grain size, microhardenss and fracture toughness of the LuAG and YAG.

	Grain size (μm)	Microhardness (GPa)	Fracture toughness (MPa $m^{1/2}$)
LuAG ceramic	1-2	22.8	2.2
LuAG single crystal	-	16.5	1.78
YAG ceramic	1-2	16.8	4.3
YAG single crystal	-	14.5	1.8

Table. 4.1 indicates the average grain size, microhardness H and fracture toughness K_{1C}, which can be calculated with eq. (4.1) and (4.2), of the Yb:LuAG and Yb:YAG single crystals and ceramics [112].

$$H = K\frac{P}{d^2} \tag{4.1}$$

$$K_{1C} = 0.016\left(\frac{E}{H}\right)^{1/2}\frac{P}{C^{3/2}} \tag{4.2}$$

where K is the shape factor of indenter (=1.854), P is the indenter load, d is the indentation diagonal, E is Young's modulus, and $C^{3/2}$ is the linear size of radial crack. Un-doped LuAG ceramic has the measured average grain size of 1-2 μm two-dimensionally and thus the actual average grain size can be estimated to be $\approx$ 3 μm ($\times$ 1.56 larger [113]). The microhardness and the fracture toughness of un-doped LuAG ceramic are higher than those of LuAG single crystal.

4.1.2 Thermal properties

The thermal properties, especially thermal conductivity are key parameters to characterize the performance of the gain medium. The thermal conductivity K (W/m $\cdot$ K) is described as

$$K = \alpha \cdot C_p \cdot \rho \tag{4.3}$$

where α (m^2/s) is the thermal diffusivity, C_p (J/m·K) is the heat capacity, and ρ (g/m^3) is the density.

Measurement of thermal diffusivity

The flash method which used a Xe flash lamp as the light source (LFA 447 NanoFlash, NETZSCH) was employed for the measurement of the α. Figure

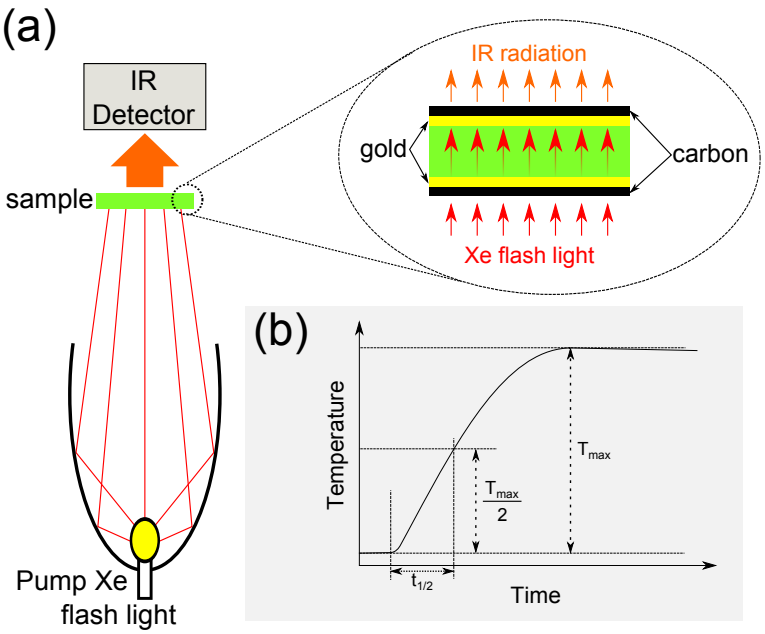

Fig. 4.2: Schematic of the flash method. (a) Measurement setup, inset shows the drawing of the coating of the sample. (b) Temperature evolution.

4.2 (a) indicates the brief schematic of the flash method. Both sides of the sample has the layers of Au with a thicker thickness than the skin depth to prevent the penetration of the pump light, and sprayed carbon which enhances the absorption of the heat and the radiation. The light source heats up the backside of the sample. The heat migrates from the backside to the topside, and then emits the infrared (IR) radiation from the topside. The IR detector measures the time dependence of the IR radiation as the temperature rise of the topside (Fig. 4.2 (b)). By using the above temperature behavior and the thickness of the sample l, α can be determined by the following equation [114].

$$\alpha = 0.1388 \cdot \frac{l^2}{t_{1/2}} \tag{4.4}$$

where $t_{1/2}$ (s) is the time to the half maximum of the highest temperature $T_{max}/2$.

Calculation of heat capacity

When measuring the thermal diffusivity, not only the sample to be measured, but also the reference sample whose thermal properties (α, C_p, and K) are already known is also measured simultaneously. Here, Pyroceram9606 was

used as a reference. By use of each measured constants, the heat capacity of the sample is given by

$$C_p^{test} = \frac{T_\infty^{ref.}}{T_\infty^{test}} \cdot \frac{Q^{test}}{Q^{ref.}} \cdot \frac{V^{test}}{V^{ref.}} \cdot \frac{\rho^{ref.} \cdot D^{ref.}}{\rho^{test} \cdot D^{test}} \cdot \frac{d_{orifice}^{2,test}}{d_{test}^{2,ref.}} \cdot C_p^{ref.}(T) \tag{4.5}$$

$T_\infty^{ref.}$: Voltage increase of the detector signal at the reference. (a.u.)
T_∞^{test} : Voltage increase of the detector signal at the sample. (a.u.)
$Q^{ref.}$: Energy on the reference. (a.u.)
Q^{test} : Energy on the sample. (a.u.)
$V^{ref.}$: Amplification factor of the reference.
V^{test} : Amplification factor of the sample.
$\rho^{ref.}$: Density of the reference. (g/cm^3)
ρ^{test} : Density of the sample. (g/cm^3)
$D^{ref.}$: Thickness of the reference. (mm)
D^{test} : Thickness of the sample. (mm)
$d_{orifice}^{ref.}$: Area of the orifice for the reference. (mm^2)
$d_{orifice}^{test}$: Area of the orifice for the sample. (mm^2)
$C_p^{ref.}$: Heat capacity of the reference. (J/g $\cdot$ K)

Measured thermal properties

The thermal properties of an un-doped LuAG ceramic with a thickness of 1.31 mm and 10 at.% Yb:LuAG ceramic with a thickness of 1.31 were measured with the flash method. The measured thermal properties are summarized in Table 4.2. The thermal conductivity of un-doped LuAG ceramic (8.8 W/m·K) is lower than that of un-doped YAG single crystal (9.5 W/m·K [2]). After doping the $Yb^{3+}$of 10 at.%, Yb:LuAG ceramic indicates higher thermal conductivity (8.1 W/m·K) than that of Yb:YAG single crystal (6.1 W/m·K [2]). Yb:LuAG ceramic indicates high thermal conductivity even in heavy doping situation like single crystal. The thermal conductivities of un-doped and

Table 4.2: Thermal properties of un-doped and 10 at.% Yb^{3+}-doped LuAG ceramic.

	Thermal diffusivity (mm^2/s)	Heat capacity (J/g ·K)	Density (g/cm^3)	Thermal conductivity (W/m·K)
LuAG	2.53 ± 0.09	0.54 ± 0.03	6.65 ± 0.07	8.8 ± 0.5
10 at.% Yb:LuAG	2.67 ± 0.08	0.46 ± 0.02	6.67 ± 0.07	8.1 ± 0.5

10 at.% Yb^{3+}-doped single crystals are , for example, 7.7 W/m·K and 7.4 W/m·K, respectively [2]. It is very difficult to rating the thermal conductivities of our un-doped and Yb^{3+}-doped LuGA ceramics are higher than those of un-doped and Yb^{3+}-doped single crystals because the thermal conductivity itself depends on the fabrication/growing methods, the measurement methods, and so on. One useful comparison would be the drop rate of the thermal conductivity because the large drop in thermal conductivity means the increase of the phonon scattering, i.e. the decrease of the quality of the sample. The drop of the thermal conductivity by Yb^{3+}-doping in above mentioned LuAG single crystal is $\approx 4\%$ whereas that of our LuAG ceramic is $\approx 8\%$. Our Yb:LuAG ceramic indicates twice larger decline of the thermal conductivity. The reason should be originated in the ceramic itself. The result suggests there is the room for improvement of the optimization of the fabrication process.

4.1.3 Spectroscopic properties

Measurement of the absorption spectrum

The collimated white light source (YOKOGAWA AQ-4305) and the optical spectrum analyzer (YOKOGAWA AQ-6370B) were used for the measurement of the transmission spectrum. Consider the intensity of the white light source before (I) and after passing trough the sample under test (I'). I' can be written as

$$I' = I \exp\left(-\alpha(\nu) L_g\right) \tag{4.6}$$

where $\alpha(\nu)$ (cm^{-1})is the absorption coefficient and L_g is the length of the sample. By use of the transmittance T which is determined as $T \equiv I'/I$, $\alpha(\nu)$ can be given by

$$\alpha(\nu) = -\frac{1}{L_g} \ln(T) \tag{4.7}$$

Since the absorption coefficient equals to the negative gain, $\alpha(\nu)$ can be described as below by use of the N_{tot} and $\sigma_{abs,eff}$ without pumping in Eq. (3.5)

$$\alpha(\nu) = N_{tot} \sigma_{abs} \tag{4.8}$$

Here σ_{abs} is determined as the absorption cross section without pumping. From Eq. (4.8), the absorption cross section can be determined if N_{tot} is known. It can be obtained using the molecular weight M (g), the density ρ (g/cm^3), doping concentration C (at.%), Avogadro's number N_A, and the substitution ratio r.

$$N_{tot} = \frac{\rho}{M} \cdot \frac{C}{100} \cdot N_A \cdot r \tag{4.9}$$

In this thesis, an absorption coefficient spectrum is used as the absorption spectrum because it is more useful when estimating the total pump absorption of a thin-disk gain medium mounted in the multi-pass pumping module.

Absorption spectrum

Figure 4.3 indicates the absorption spectrum of the 10 at.% Yb:LuAG ceramic. Its zero-phonon absorption peak is located at 968 nm with a narrow bandwidth. There is a broad absorption band around 940 nm. Since its zero-phonon line has the narrow bandwidth and slight blue shifted wavelength compared with those of Yb:YAG, the special wavelength stabilized laser diode (LD) should be required for the zero-phonon pumping. Here the broad absorption band around 940 nm was chosen as the pumping wavelength, and it enables the pumping with conventional non-wavelength stabilized LDs operating at 940 nm.

Measurement of the emission spectrum

The emission cross section was calculated with Füchtbauer-Ladenburg equation [115] given by

$$\sigma_{emi} = \frac{\lambda^4}{8\pi c n^2} \frac{\beta}{\tau} \frac{I(\lambda)}{\int I(\lambda) d\lambda} \tag{4.10}$$

where β is the branching ratio which should be 1 in case of the Yb^{3+}-doped material, $I(\lambda)$ is the emission spectrum which was measured with a fiber-

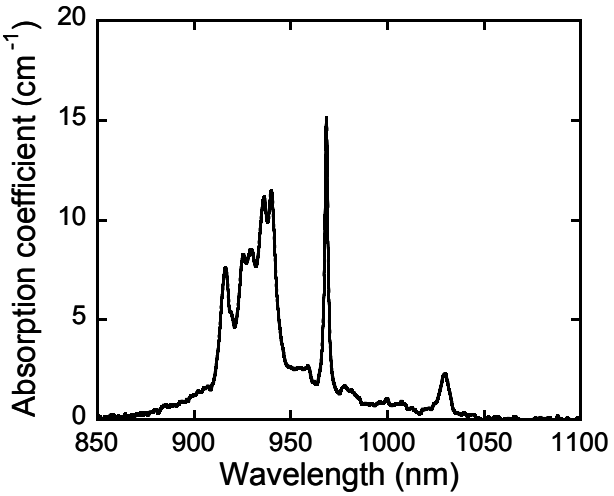

Fig. 4.3: Absorption spectrum of 10 at.% Yb:LuAG ceramic.

coupled LD operating at 915 nm (FITEL FOL0911R30-117-915) and the same optical spectrum analyzer as in the measurement of the absorption spectrum.

Emission spectrum

The emission spectrum of the Yb:LuAG ceramic is shown in Fig. 4.4. A main emission band of the Yb:LuAG is centered at 1030 nm with a maximum emission cross section σ_{emi} of 2.5×10^{-20} cm^2 and a full width half maximum (FWHM) of 6.1 nm. There is also the small emission band with the center wavelength of 1046 nm corresponding to σ_{emi} of 3.6×10^{-21} cm^2. The bandwidth of Yb:LuAG ceramic is narrower than that of Yb:YAG of $\approx$ 8 nm whereas the emission cross section at 1030 nm is 25% larger than that of Yb:YAG. Though the narrow gain bandwidth limits short pulse generation, the large emission cross section is the great advantage for thin-disk laser/amplifier architectures which requires high gain.

Luminescence lifetime

The luminescence lifetime was measured with the pulsed operation mode (the repetition rate of 200 Hz and the pulse duration of 10 μs) of the same fiber-coupled LD used in the measurement of the emission spectrum and an InGaAs PIN photo-diode (HAMAMATSU photonics G8370-03). Figure 4.5 shows the measured fluorescence decay. There is no fast decay which is attributed to the non-radiative transition. Yb:LuAG ceramic has only the single exponential decay and its fluorescence lifetime was calculated to be 1.07 ms.

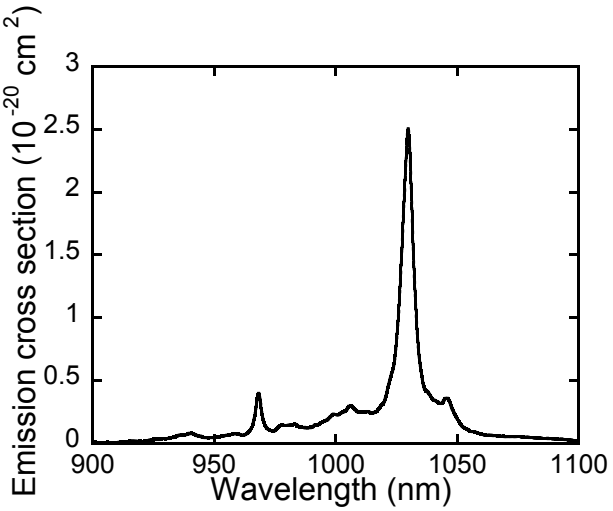

Fig. 4.4: Emission spectrum of 10 at.% Yb:LuAG ceramic.

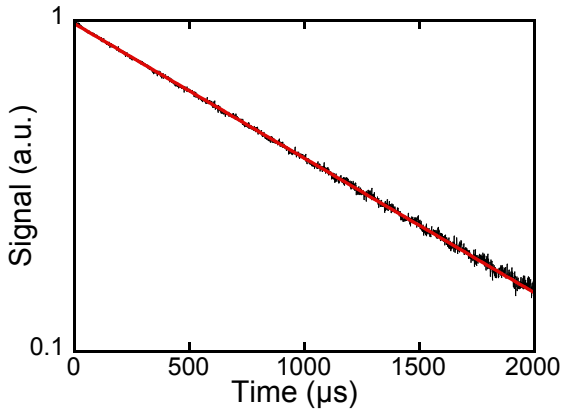

Fig. 4.5: Fluorescence decay of 10 at.% Yb:LuAG ceramic.

4.1.4 Laser performances of bulk-shaped Yb:$Lu_3Al_5O_{12}$ ceramic

The laser performances of bulk-shaped Yb:LuAG ceramic in both the CW and the pulsed regime were evaluated. For the experiments, a non-coated 10 at.% Yb:LuAG ceramic with a thickness of 1.24 mm was prepared.

CW laser operation

The schematic of the setup for the CW laser operation is shown in Fig. 4.6 The I-shaped resonator consisted of a plane dichroic mirror (DM) and a concave output coupler (OC) with a ROC of 100 mm. The DM has a high transmission (HT) coating for the pump wavelength, and a high reflection (HR) coating for the laser wavelength. To compare the laser performances, three OCs with different transmittances of 1%, 3%, and 5% were used. The pump source was a fiber-coupled laser diode (FCLD) with a center wavelength of 940 nm and a maximum output power of 35 W (LIMO GmbH, LIMO35-F100-DL940). The core diameter and the numerical aperture (NA) of the delivery fiber are 100 μm and 0.22, respectively. The pump laser bean was collimated and focused in the Yb:LuAG ceramic with a focal spot diameter of $\approx$ 130 μm by the combination of lenses with focal lengths of 40 mm and 50 mm. The Yb:LuAG ceramic was placed near the DM to achieve an optimum mode overlapping between the pump beam at the focus point and the TEM_{00} mode. The mode propagation inside the resonator was calculated based on the ABCD-law, and then the optimum resonator length was estimated and set to be $\approx$ 100 mm.

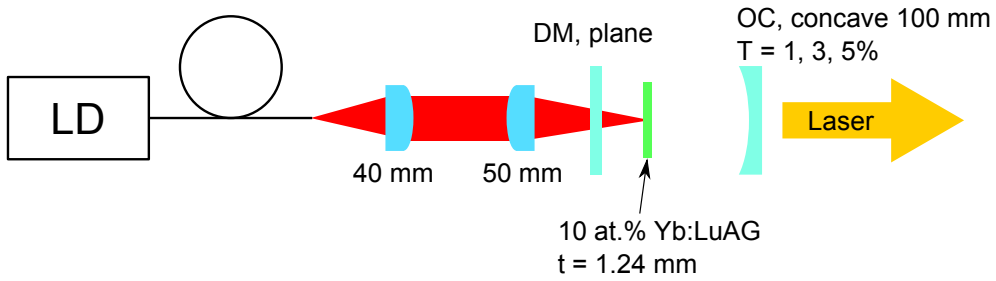

Fig. 4.6: Schematic of the setup for the bulk-shaped Yb:LuAG ceramic laser in CW regime.

The laser performances are shown in Fig. 4.7 and are summarized in Table 4.3.

Here, P_{abs} is calculated with the equation described below.

$$P_{abs} = P_{pump} - (P_{sum} - P_{laser}) \tag{4.11}$$

where P_{pump} is the incident pump power, P_{sum} is the summation of the unabsorbed pump power under lasing and the output laser power, and P_{laser} is the output laser power. In the above equation, the pump saturation effect is taken into account to estimate the actual absorbed pump power P_{abs}. In this resonator configuration, the unabsorbed pump power and the output laser power were measured simultaneously because the direction of both beams are coaxial. P_{laser} was measured firstly by canceling the pump beam using the low pass filter, then the unabsorbed pump power was estimated.

A maximum output power of 1.73 W with an optical and a slope efficiencies of 42% and 45%, respectively, were obtained with 1% of output coupling. In case of 3% of output coupling, a maximum output power of 2.09 W was obtained with an optical efficiency of 53% and a slope efficiency of 61% . The best performance was obtained with 5% of output coupling. A maximum output power reached 2.14 W with an optical efficiency of 55% and a slope efficiency of as high as 72%. The highest slope efficiency of 72% is the same as

Table 4.3: Summary of the laser performances of bulk-shaped Yb:LuAG ceramic.

T_{OC} (%)	P_{out} (W)	η_{o-o} (%)	η_{slope}(%)
1	1.73	42	45
3	2.09	53	61
5	2.14	55	72

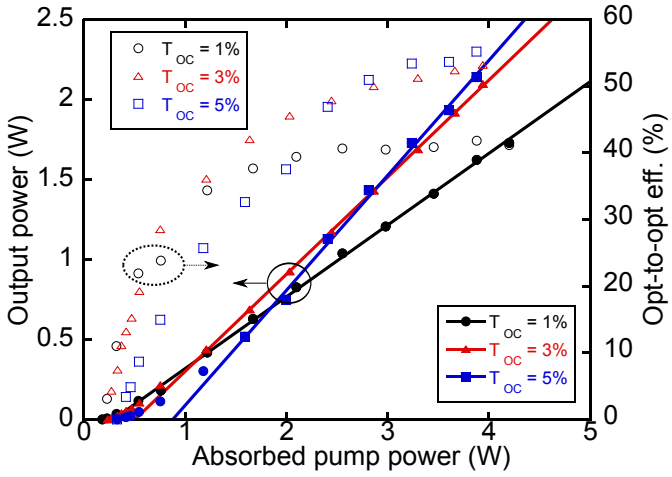

Fig. 4.7: Laser performances of bulk-shaped Yb:LuAG ceramic laser.

that demonstrated with Yb:LuAG single crystal [116]. The Yb:LuAG ceramic indicated the efficient CW laser operation even it has no AR coating.

Mode-locking

The laser oscillation of Yb:LuAG ceramic in the CW regime was successfully observed without any problems. The next subject is investigating the laser performances under a high peak power operation. The passively mode-locked laser resonator was constructed and is shown in Fig. 4.8. The same Yb:LuAG ceramic used in the CW laser experiment was used for the mode-locking, and was pumped by the broad stripe LD operating at 930 nm. The pump laser beam was shaped and focused in the Yb:LuAG ceramic with the cross sectional size of $\approx$ 20 (vertical) $\times$ 90 (horizontal) μm by the four lenses. The Yb:LuAG ceramic was inserted between the two HR mirrors with ROC of 100 mm (M1 and M2) under the Brewster's angle of 61.2°. The group delay dispersion (GDD) was compensated by a pair of SF 10 prisms with a separation of 45 cm and a Gires-Tournois interferometer (GTI) mirror with the GDD of -250 fs^2. These ledto the total negative GDD per a round trip of $\approx$ -3000 fs^2. The mode-locking was initiated by a SESAM (BATOP GmbH) with a modulation depth (ΔR) of 1% at 1030 nm, a saturation fluence of 120 $\mu J/cm^2$, and a relaxation time constant of 500 fs. The TEM_{00} laser mode was focused on the SESAM by a concave HR mirror with a of 300 mm (M3) to increase the fluence on the SESAM. The plane output coupler has

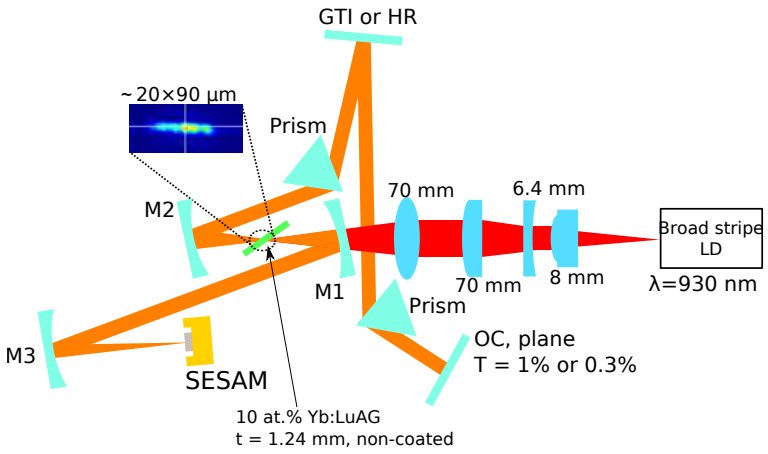

Fig. 4.8: Schematic of the setup for the mode-locked Yb:LuAG ceramic laser.

a transmittance of 1% and a wedge angle of 30′ to get rid of negative effects caused by the residual reflection from the back side of the OC.

The first demonstration of the passively mode-locked Yb:LuAG ceramic have been successfully realized. Figure 4.9 (a) indicates the output power evolution. A self Q-switched mode-locking (Q-ML) was initiated in a lower pump power region. At a pump power of 2.3 W, a CW mode-locked operation (CW-ML) was obtained. The maximum average output power in the single-pulsed CW-ML was 200 mW with a center wavelength of 1032.3 nm at the pump power of 3.86 W. Figure 4.9 (b) and (c) indicate the pulse trains recorded by an oscilloscope with a bandwidth of 500 MHz (Tektronix, Inc., TDS3052B) in the long time scale of 4μs/div and in the short time scale of 2 ns/div, respectively. The repetition rate was 96.6 MHz corresponding a resonator round trip frequency. The pulse trains show the slight floated zero-level. It is obvious that the floating from the ground-level is not due to the CW component because the lasing spectrum (Fig. 4.10 (b)) has an almost ideal sech^2 shape. It would be due to the stray light because the detector was not covered. The sech^2-fit pulse duration of 699 fs (Fig. 4.10 (a)) and the spectral bandwidth of 1.7 nm (Fig. 4.10 (b)) which resulted in the time bandwidth product of 0.334 (0.315 for the Fourier transform limited pulse) were obtained. When the pump power was further increased, the multi-pulsed mode-locked operation due to lower effective gain for the single pulse than that of double or more pulse was observed.

To obtain more shorter pulse duration, one effective way is increase of the intracavity pulse energy. Here, the transmittance of the OC in Fig. 4.8 was

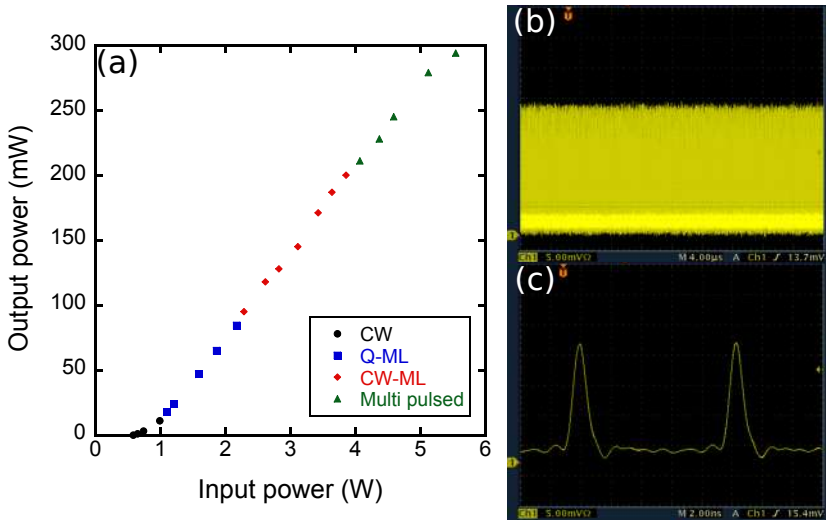

Fig. 4.9: Mode-locked laser performances of bulk-shaped Yb:LuAG ceramic. (a) Power evolution. (b) Recorded pulse train in a long time span (4 μs/div) and (c) short time span (2 ns/div).

changed to 0.3%, and the GTI mirror was replaced to the HR mirror for the dispersion management. A maximum output power of 53 mW in the single pulsed CW-ML regime was obtained with the shortest pulse duration of 541 fs and a spectral bandwidth of 2.5 nm which resulted in the time bandwidth product of 0.380. Compared with Yb:YAG, Yb:LuAG is expected to have more strong tendency of the pulse splitting due to the narrow gain bandwidth which lead quite sharp shape of the effective gain. A more deeper modulation depth by, for example, Kerr effect is necessary to obtain more shorter pulse duration.

4.2 Thin-disk laser experiments of soldered Yb:$Lu_3Al_5O_{12}$ ceramics

In this Section, the demonstrations of the thin-disk laser with soldered Yb:LuAG ceramics are discussed. The results include the first demonstration of the thin-disk laser operation using Yb:LuAG ceramic. The experiments shown in this Section have been demonstrated at the IFSW.

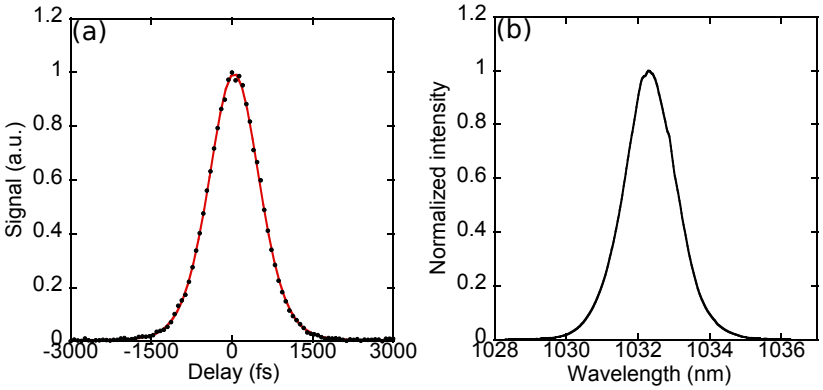

Fig. 4.10: (a) SH autocorrelation trace and (b) lasing spectrum

4.2.1 Disk information

Yb:LuAG ceramics with a doping concentration of 10 at.% and a 6 mm × 6 mm cross section were prepared for the experiments. The ceramics were polished down to different center thicknesses of 150 μm, 200 μm, and 300 μm to compare laser efficiencies which can be degraded by re-absorption. Figure 4.11 describes the brief cross sectional drawing of the Yb:LuAG ceramic thin-disk with its coatings supplied by Okamoto Optics Works, Inc.. The front surface of the disk had an AR coating for both the pump and the laser wavelengths. The AR coating side of the disk was polished with a wedge angle of 30 minutes for the elimination of the negative effects which could be triggered by the residual reflection from the AR coating. The opposite surface had the HR coating for the same wavelengths as in the AR coating. Further metal layers, the chromel (the alloy of Ni and Cr with a ratio of 90:10) and the gold, were over-coated on the HR coating for the soldering.

After the coating, each disk was bonded on the oxygen-free Cu heat sink with the In-Sn solder at the IFSW. The ROC of the disks for the major

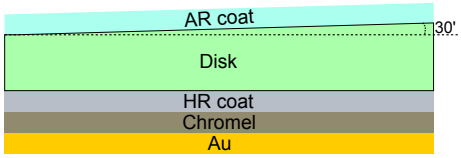

Fig. 4.11: Cross sectional drawing of the Yb:LuAG disk with coatings.

Table 4.4: Radii of curvatures of the disks.

Thickness (μm)	R_{ma} (m)	R_{mi} (m)
150	5.64	4.37
200	20.07	10.04
300	9.13	4.82

axis R_{ma} and for the minor axis R_{mi} were measured with the PSI and are summarized in Table. 4.4. The discrepancy between the ROC for the major axis and the minor axis is not so large in case of the disk with the thickness of 150 μm. However, disks with the thicknesses of 200 μm and 300 μm have nearly twice differences of the ROC which might be due to the bad matching between the metal layers and the bonding process. It can be a fatal problem especially in the fundamental-transverse-mode laser operation which requires the control of the TEM_{00} mode size on the disk.

4.2.2 First thin-disk laser demonstration with 300 μm-thick disk

Unfortunately, the 200 μm-thick disk was broken at a pump density of 4.6 kW/cm^2 when the laser oscillation was stopped instantaneously. Hence the first laser demonstration have been realized with the 300 μm-thick disk. Figure 4.12 shows the schematic of the setup of the laser resonator. The disk with heat sink was mounted in a multi-pass pumping module with 24 pump beam passes provided by IFSW (B1 module [117]). Note that, the module was used for all of the thin-disk laser experiments in this Chapter. A V-shaped resonator, which was formed by a plane HR mirror and a concave OC with a transmittance of 3% and the ROC of 1000 mm, was constructed to operate in a multi-mode regime. The disk was pumped by a FCLD (LDM1000-1150, Laserline GmbH) with an operating wavelength of 940 nm. The maximum pump power and the pump spot diameter on the disk were 216 W and 2.6 mm, respectively, with the corresponding maximum pump power density of $\approx$ 4.1 kW/cm^2.

The laser performance is shown in Figure 4.13. At a maximum pump power of 216 W, a maximum output power of 101 W was successfully demonstrated with an optical efficiency of 47% and a slope efficiency of 45%. This is the first result of the thin-disk laser operation based on the Yb:LuAG ceramic. However, an anomalous behavior was observed in the low pump power regime ($0 \sim 50$ W) in Fig. 4.13. The optical efficiency is already the maximum value

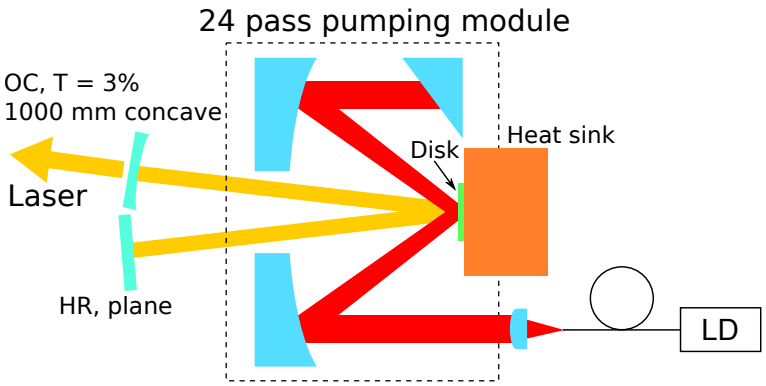

Fig. 4.12: Schematic of the setup for the thin-disk laser experiment with the 300 μm-thick disk. The detailed configuration is described in the text.

at the minimum pump power, and then followed by the rapid decline up to the pump power of 50 W. After that, the optical efficiency increases gradually as an increase of the pump power. The reasons would be the measurement error in the low pump power regime. The pump source and the water-cooled power meter used in the experiment have the potential to emit/measure the power up to 1 kW. Hence, it would be possible to indicate accidentally some small fluctuation of the pump powers which cause the large errors in the optical efficiency in the low pump power regime.

Re-checking the powers was tried, but, unfortunately the disk was broken during the experiment. Figure 4.14 (a) is the image on the disk observed with a CCD camera and Fig. 4.14 (b) is an actual photograph of the damaged disk . A bright spot (dotted circle in Fig. 4.14 (a)) appeared suddenly during the experiment. Its brightness was increased with time, and then the disk was suddenly broken at the pump power density of 3 kW/cm^2. This would be caused by the bad bonding. The soldering process developed at the IFSW is well optimized when the metal layer coating is by their own. In this experiment, the metal layers of the disks were coated in Japan. Hence the non-optimum parameters would initiate some defects in the bonding layer.

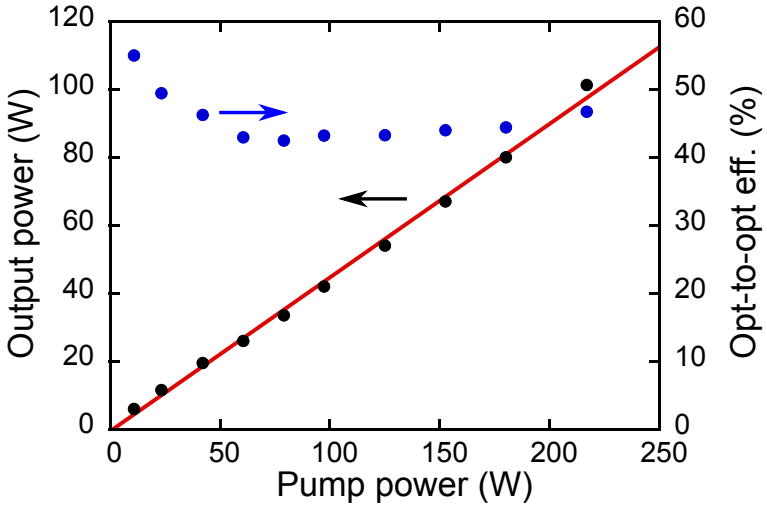

Fig. 4.13: The first laser result of the 10 at.% Yb:LuAG ceramic disk with the thickness of 300 μm. The output power of above 100 W were successfully demonstrated. However, anomalous behavior was observed in the low pump power regime. The details are described in the text.

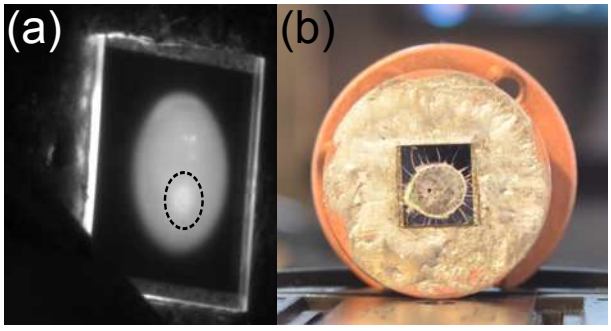

Fig. 4.14: (a) Image of the pumped disk recorded with a CCD. The bright spot which was marked with a dotted circle appeared during the experiment, and initiated the destruction of the disk. (b) Photograph of the broken disk.

4.2.3 Thin-disk laser operation with 150 μm-thick disk

The thin-disk laser oscillation with the Yb:LuAG ceramic disk with a thickness of 150 μm was check whether the disk was broken or not. The schematic of the setup of the laser resonator operating in a multi-mode regime is shown in Fig. 4.15 In this experiment, the pump spot diameter was limited up to $\approx$ 2 mm due to a small damage on the disk. The components of the resonator other than the transmittance and the ROC of the OC are the same as the resonator shown in Fig. 4.12. Because the pump spot diameter on the disk of 1.8 mm was smaller than the pump spot diameter of 2.6 mm in Fig. 4.12, the concave OC with the smaller ROC than the OC in Fig. 4.12 was chosen. Owing to the smaller pump spot diameter, the maximum pump power was limited up to 93 W which corresponds to the maximum pump power density of $\approx$ 3.7 kW/cm^2.

Figure 4.16 shows the laser performance. A maximum output power of 50 W was obtained at a pump power of 93 W. A maximum optical efficiency and a slope efficiency of 56% and 58%, respectively, were obtained. The higher efficiencies than the case of the 300 μm-thick disk were obtained even the maximum pump density in this experiment was slightly lower. While the bright spot which was observed in the 300 μm-thick disk did not appear, the laser oscillation was a bit instable. Furthermore, no lasing was obtained when the laser operation in the fundamental-mode regime was tried.

The ROC of the disk were again measured since the fundamental-mode laser oscillation is sensitive to the change of the ROC of the disk. Table 4.5 indicates the measured ROC before and after the laser experiment. The ROC

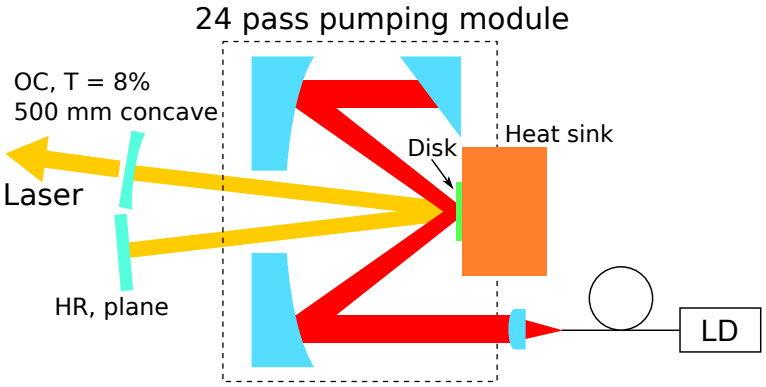

Fig. 4.15: Schematic of the setup for the thin-disk laser experiment with the 150 μm-thick disk. The detailed configuration is described in the text.

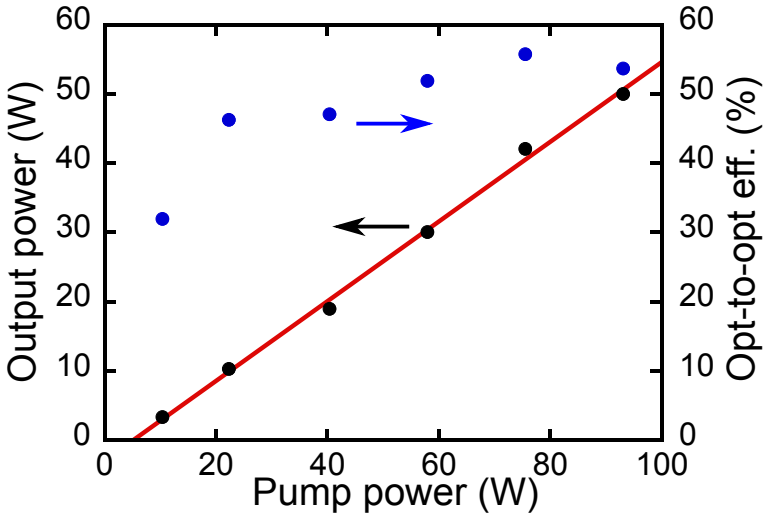

Fig. 4.16: Thin-disk laser performances of 150 μm-thick 10 at.% Yb:LuAG ceramic disk.

for the major axis is slightly increased, and that for the minor axis became larger value than that in initial state. This is the reasonable evidence to explain why any laser oscillation could not be observed.

Table 4.5: Radii of curvatures of the disk before and after the laser experiment.

	R_{ma} (m)	R_{mi} (m)
Initial	5.64	4.37
Last	7.5	4.5

4.3 Thin-disk laser experiments of glued Yb:$Lu_3Al_5O_{12}$ ceramics

In the previous Section, the first thin-disk laser operation has been demonstrated with the soldered Yb:LuAG ceramic disk. However, the stable laser oscillation and the fundamental-mode oscillation could not be obtained due to the damage or the deformation of the disk. In this Section, the thin-disk laser operation of the Yb:LuAG ceramics which were contacted on the heat sink by another contacting method using an epoxy resin is discussed.

4.3.1 Disk information

The disks with the same dimensions, thicknesses, and wedge angles as the soldered disks, but without metal layers were prepared to confirm that the instability, the damage, and the deformation did not originate in the Yb:LuAG itself. The polishing and the coating were again supplied by Okamoto Optics Works, Inc., and the gluing processes were again done at the IFSW. The ROC of the disks are summarized in Table 4.6. As is the case in the soldered disk, the glued disk with a thickness of 150 μm indicates the most smallest (in this case, no difference) discrepancy of the ROC between the major axis and minor axis. The discrepancies of the ROC in other two disks are quite small compared with those of the soldered disks. It can be one of the proofs that the coated metal layers were not optimized for the soldering process at the IFSW and the gluing indicates much relaxed contacting condition.

Table 4.6: Radii of curvatures of the glued disks.

Thickness (μ m)	R_{ma} (m)	R_{mi} (m)
150	16	16
200	2.6	2.1
300	5.2	4.2

4.3.2 Thin-disk laser operation with 200 μm-thick disk

For the first experiment, the 200 μm-thick disk was selected. Firstly, the multi-mode operation was demonstrated to evaluate the maximum laser performances. After that, the first fundamental-mode operation was demonstrated. A linearly polarized operation was also challenged to evaluate the depolarization effect of the disk. These experiments have been demonstrated at the ILS.

Multi-mode operation

Figure 4.17 shows the schematic of the setup of the thin-disk laser experiment with the 10 at.% Yb:LuAG ceramic disk with the thickness of 200 μm. The disk with a heat sink was installed to the 24 pass multi-pass pumping module provided by the IFSW, and was pumped by the fiber coupled LD with the available pump power of 180 W and the operating wavelength of 940 nm (F300-940-4, Apollo Instruments, Inc.). The pump spot diameter was chosen to be

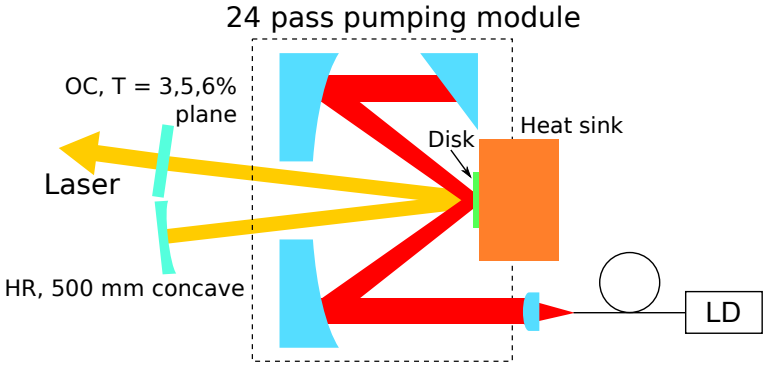

Fig. 4.17: Schematic of the setup of the thin-disk laser operation with the glued 200 μm-thick disk. The detailed configurations are described in the text.

2.5 mm which corresponds to the maximum pump density of ≈ 3.7 kW/cm^2. The resonator operated in the multi-mode regime was the V-shaped resonator which composed of a HR concave mirror with the ROC of 500 mm and a plane OC. To find the optimum output coupling, OCs with different transmittances of 3, 5, and 6% were used.

The laser performances are shown in Fig. 4.18, and are summarized in Table. 4.7. A maximum output power, an optical efficiency, and a slope efficiency of 94 W, 52% and 60%, respectively, were obtained with 3% of output coupling. In case of 6% of output coupling, an output power of 94 W, an optical efficiency of 52%, and a slope efficiency of 62% were achieved. The best performance was recorded when the output coupling was 5%. A maximum output power reached 101 W with a maximum optical efficiency of 56% and a slope efficiency of 64%. The lasing wavelength was always around 1031 nm for all experiments. For measurement of the beam quality factors M^2, a slit scanning beam profiler (BP 109-ir, Thorlabs Inc.) was used. The measured M^2 values were 24, 30 and 27 for 3, 5 and 6% of output coupling, respectively, at a maximum pump power .

Table 4.7: Summary of the laser performances for the glued 200 μm-thick disk.

T_{OC} (%)	P_{out} (W)	η_{o-o} (%)	η_{slope}(%)	M^2
3	94	52	60	24
5	101	56	64	30
6	94	52	62	27

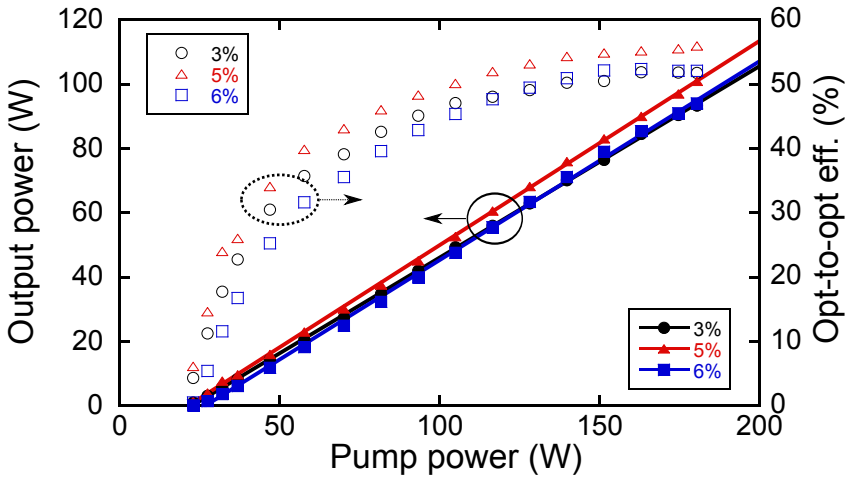

Fig. 4.18: Thin-disk laser performances of the glued 200 μm-thick disk.

During the experiment, any damages and instabilities were not observed. The 200 μm-thick disk indicates higher slope efficiency than that demonstrated with the soldered disk of 58%. These results proved the the damages or the deformation in the soldered disks were originated in the non-optimum parameters in the soldering.

Fundamental-mode operation

The thin-disk laser operation with a near diffraction limited beam quality, which is the advantage in the thin-disk concept, was evaluated for the Yb:LuAG ceramic. The schematic of the setup is shown in Fig. 4.19. The resonator consisted of a convex HR mirror with a ROC of -2000 mm and a plane OC with a transmittance of 5% which derived from the previous experiment as the optimum output coupling. For saving the space, a plane HR mirror was inserted between the disk and the OC. The diameter of the TEM_{00} mode on the disk was designed to be $\approx$ 80% of the pump spot size of 2.5 mm to optimize the mode overlapping between the TEM_{00} mode and the pump spot profile as mentioned in Section 3.5. This led to a relatively long over all resonator length of 2200 mm. Here the ROC of the disk are taken into account in the resonator design. The calculated propagation of the TEM_{00} mode in the resonator is shown in Fig. 4.20. In this resonator layout, the higher order transverse modes are suppressed mainly by the convex HR mirror. Note that,

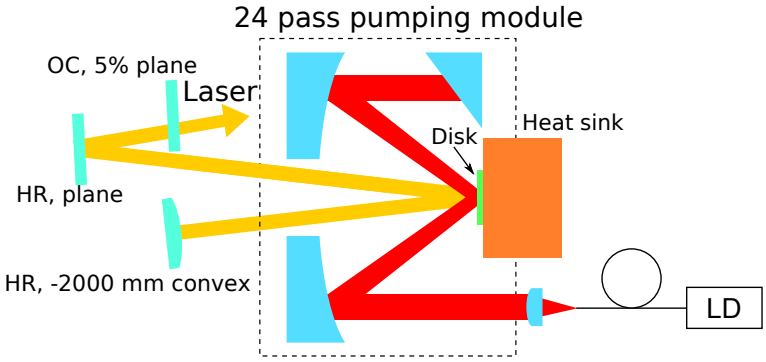

Fig. 4.19: Experimental setup for the fundamental-mode laser operation.

the resonator needs to be covered during the experiment to protect from the disturbance induced by the air conditioning system due to its long resonator length.

Figure 4.21 shows the performance of the fundamental-mode laser operation. A maximum output power was 49 W with an optical efficiency of 31%, and a slope efficiency of 44% were demonstrated. The drop in the optical efficiency at the powers exceeding 150 W maybe attributed to the thermally induced shift towards the stability limit of the resonator. The output power can be improved by adjusting the position of the convex HR mirror. To confirm the resonator was successfully working in the fundamental-mode regime, M^2 at the maximum pump power of 150 W was measured.

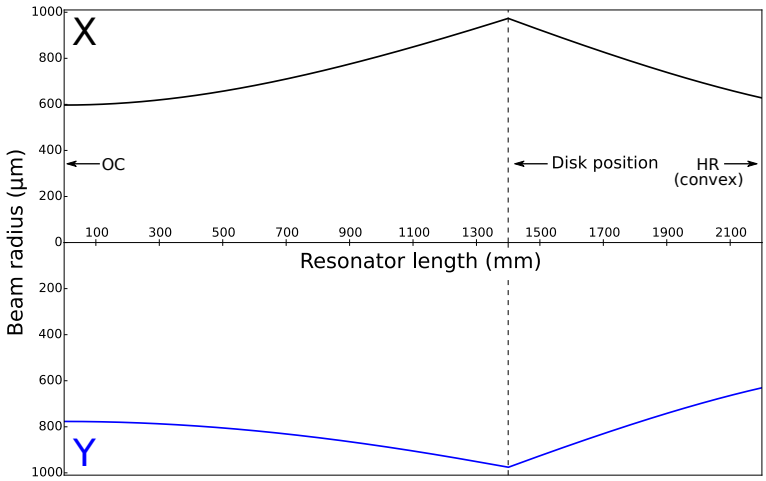

Fig. 4.20: TEM_{00} mode propagation in the resonator.

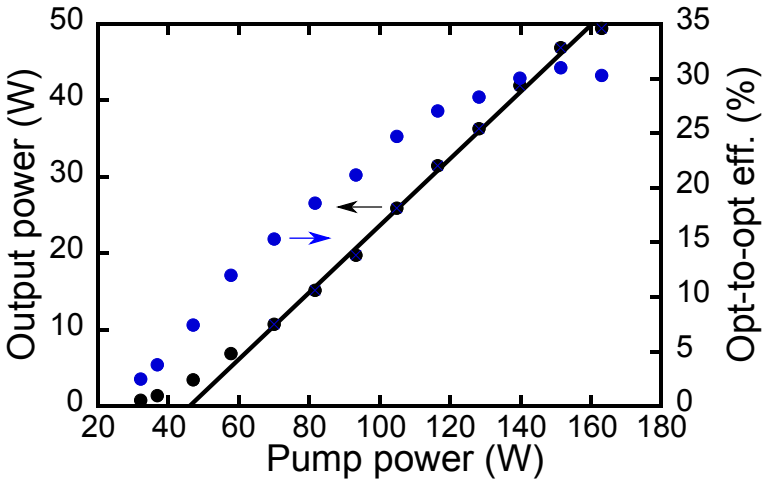

Fig. 4.21: Laser performances of the fundamental-mode operation.

A caustic measurement is shown in Fig. 4.22. M^2 values were calculated to be 1.09 for ${M^2}_x$ and 1.36 for ${M^2}_y$ which resulted in an average beam quality factor ${M^2}_{mean} = 1.22$. The discrepancy in the M^2 between x and y direction is attributed to the difference of the ROC of the disk as measured and summarized above. The inset in Fig. 4.22 shows the beam profile recorded at the maximum pump power. Though it is slightly deformed, it shows the nearly ideal Gaussian shape.

The first thin-disk laser operation of the Yb:LuAG ceramic in the fundamental-mode regime have successfully been demonstrated. The efficiencies in the fundamental-mode operation (η_{o-o} of 31% and η_{slope} of 44%) is lower compared with those in the multi-mode operation (η_{o-o} of 56% and η_{slope} of 64%) due to the suppression of other higher order modes. Currently, the Yb:LuAG single crystal thin-disk demonstrates the highest optical efficiency in the fundamental-mode regime of 58.5% with M^2 of 1.55 [31]. Though employing the zero-phonon line pumping is the one of the reason of the high optical efficiency in the demonstration, the optical efficiency of our fundamental-mode thin-disk laser oscillation is almost half of them. There should be some reasons other than the condition of the resonator which lower the efficiency. One possible reason is the non-optimum thickness of the gain medium. As discussed in the latter Subsection 4.3.3, the optimum thickness of the gain medium seems to be around 150 μm. Another reason is the scratch flaws on the surface of the disk. As mentioned in Section 4.4, the polished disk already has the scratch flaws. While other higher order modes can cooperate for the laser oscillation in the multi-mode regime, only one mode is allowed to oscil-

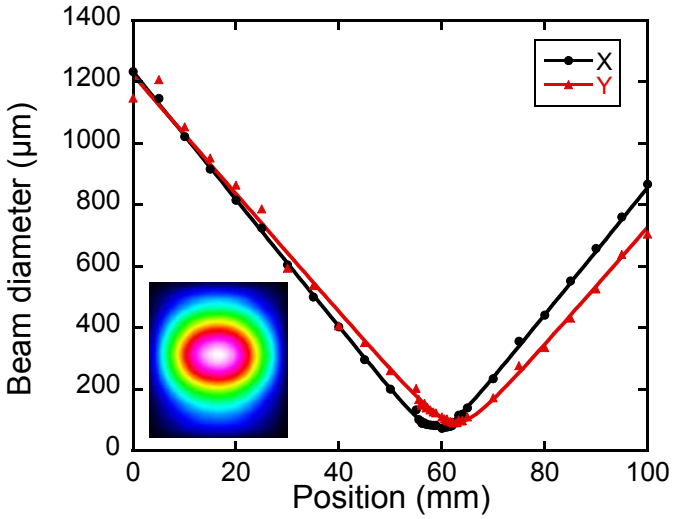

Fig. 4.22: Caustic measurement at the pump power of 150 W. Inset shows the recorded beam profile.

late in the fundamental-mode resonator. The loss induced by scratch flaws can be decrease the efficiency. The efficiency should be improved by optimizing the thickness of the disk, polishing process, and of course the fabrication process to improve the quality of the ceramic itself.

Linearly polarized operation

As discussed in Subsection 2.2.2, thermally-induced birefringence can be a serious problem especially in the thin-disk shaped ceramic. The increase of a depolarization loss degrades the efficiencies of the laser/amplifier architectures under a polarization control, e.g. mode-locked lasers and regenerative amplifiers. The depolarization loss of the ceramic thin-disk with a thickness of 200 μm was measured with the resonator operated in a linear polarization regime. The disk had the possibility to indicate the large depolarization loss due to its smaller ratio of the thickness per grain size of the disk (≈ 67) than 100. The schematic of the setup is shown in Fig. 4.23. The I-shaped resonator was formed by a plane OC with the transmittance of 3% and the HR coating backside of the disk. A fused silica Brewster's plate (BP) with a thickness of 2 mm was inserted in the multi-mode resonator to achieve the linearly polarized operation. Output powers with BP and without BP were measured by a power meter to check the power degradation. A part of the output laser beam was reflected by a wedged plate, and its extinction ratio was measured

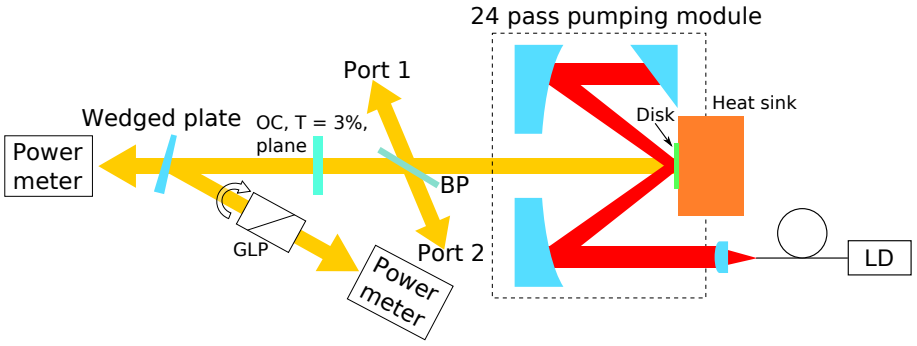

Fig. 4.23: Laser resonator for the linearly polarized operation. The polarization selection is achieved by inserting the fused silica plate under the Brewster's angle in the I-shaped resonator. The degree of polarization is measured by the combination of the power meter and the Glan-laser prism polarizer. More details are described in the text.

by the combination of the power meter and a rotated Glan-laser prism (GLP) polarizer. The powers of the reflected intra-cavity laser beams (from port1 and port2) were also measured.

The results are shown in Fig. 4.24. The black and red dots indicate the output power without and with Brewster plate, respectively. The blue and green crosses show the reflected laser powers from port1 and port2, respectively. The degradation of the output power at a pump pump power density of 3.7 kW/cm^2 (the point (iii) in Fig. 4.24) was only 3% which is almost corresponding to the summation of the output powers of port1 and port2. The corresponding depolarization loss was measured to be as low as 0.15% per a round trip.

The extinction ratio measured at the points (i), (ii), and (iii) in Fig. 4.24 are shown in Fig. 4.25. Each dot and cross in Fig. 4.25 indicates the dependence on the angle of the Glan-laser prism polarizer with and without the Brewster plate, respectively. The power dependence measured at the point (iii) indicates slight different behavior from those at the points (i) and (ii). The reason will be that a different power meter was used when measuring the powers at the point (iii). Because the maximum reflected output power by the wedged plate at the point (iii) was beyond the maximum measurable power of the power meter used at the the points (i) and (ii). Another power meter which had a slightly higher maximum measurable power with slightly poor sensitivity was used. The laser operation with a high degree of linear polarization ($\approx$ 99.5%) was obtained by inserting the Brewster plate. The

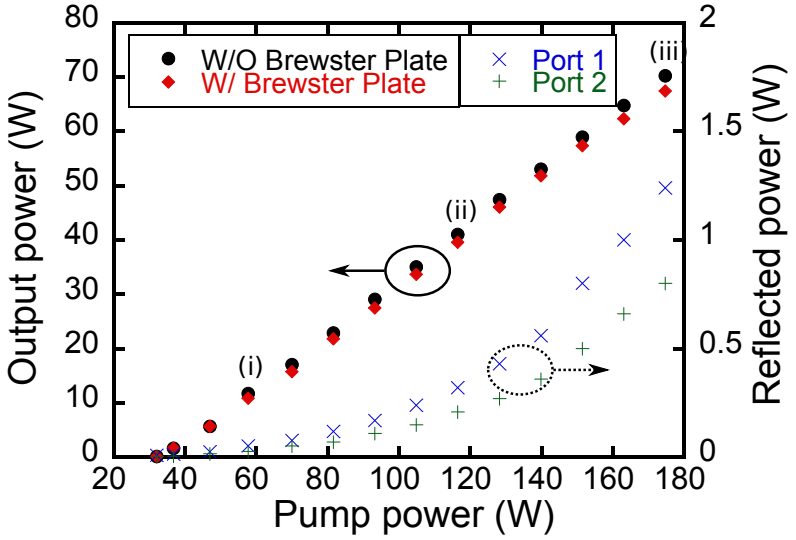

Fig. 4.24: Laser performances of the resonator with and without Brewster plate. The notation (i), (ii), and (iii) in the figure are the points where the polarization extinction ratios were measured. The details are discussed in the text.

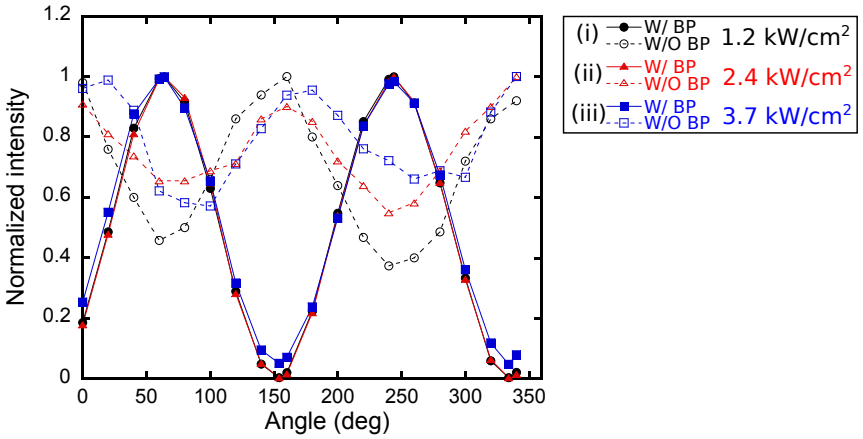

Fig. 4.25: Extinction ratio measured at the point (i), (ii), and (iii) in Fig. 4.24. The dots indicate the extinction ratio with Brewster plate at each pump power density level, the crosses indicate those without Brewster plate.

results show the depolarization loss caused by the thermally induced birefringence in our Yb:LuAG ceramic thin-disk is small enough to be used in the laser/amplifier architectures which require the polarization control.

4.3.3 Thin-disk laser operation with 150 μm-thick disk

The glued Yb:LuAG ceramic disk with a thickness of 150 μm was tested. The 150 μm-thick was expected to be indicate higher thin-disk laser performances than those of the 200 μm-thick disk because the thinner disk indicated the higher efficiencies in case of the soldered disks. A thin-disk laser operation in a multi-mode regime was firstly evaluated to compare the maximum laser performances. After that, a cavity-dumped active Q-switched thin-disk laser operation, which is the previous step to a regenerative amplifier, was challenged.

multi-mode operation

The parameters of the disk other than the size is the same as the disk with the thickness of 200 μm. The schematic of the setup was also the same as Fig. 4.17 except the pump source. Since the pump source was broken, a new fiber coupled LD with the maximum pump power of 1 kW and the operating wavelength or 940 nm (LDM1000-60, Laserline GmbH) was prepared. The previous pump LD had a short length of a delivery fiber (5 m) which led the pump distribution on the disk to the lower order super-Gaussian. The new LD has the delivery fiber with a core diameter of 600 μm and a longer fiber length of 10 m to homogenize the pump distribution. The almost top-flat profile of the pump spot distribution on the disk can be obtained. The change of the core diameter of the delivery fiber of the new pump LD caused the change of the pump spot diameter. Here, the pump spot diameter was 2.9 mm, and the maximum pump power was limited up to 280 W. The corresponding maximum pump power density was ≈ 4.2 kW/cm^2.

Figure 4.26 indicates the power performances and Table 4.8 summarizes the laser performances. A maximum output power of 158 W was obtained with a maximum optical efficiency of 57% and a slope efficiency of 64% with 3% of output coupling. When the output coupling of 6%, a maximum output power was 164 W with an optical and a slope efficiencies of 60% and 69%, respectively. The highest output power of 166 W was achieved with the maximum optical efficiency of 60% and the maximum slope efficiency of 72% in case of 5% of output coupling. The M^2 was measured at the maximum pump

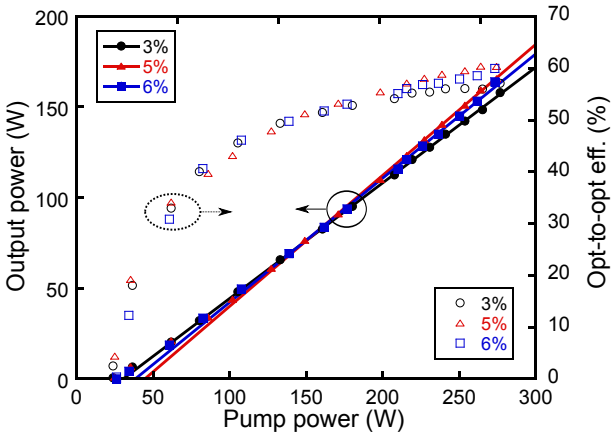

Fig. 4.26: Laser performances of the 150 μm-thick disk.

power with the same slit scanning beam profiler as the previous experiments to be 21 for 3% and 5% of output couplings and 22 for 6% of output coupling.

The 150 μm-thick disk indicates higher efficiencies than those obtained with the 200 μm-thick disk. Additionally, the highest optical and slope efficiencies in this experiment are almost the same as the current records for the thin-disk lasers with Yb:LuAG single crystals (62% for η_{o-o} and 71% for η_{slope} [2]). From these results, the thickness of Yb:LuAG ceramic of 150 μm is estimated to be near the optimum. There is a possibility to improve the efficiencies further by changing the thickness of the disk.

Table 4.8: Summary of the laser performances for the glued 150 μm-thick disk.

T_{OC} (%)	P_{out} (W)	η_{o-o} (%)	η_{slope}(%)	M^2
3	158	57	64	21
5	166	60	72	21
6	164	60	69	22

4.4 Cavity-dumped active Q-switched thin-disk laser operation

In Subsection 4.3.2, the multi-mode operation, the fundamental-mode operation, and the linearly polarized operation with a high degree of polarization were demonstrated with the 200 μm-thick disk. The previous experiments revealed the optimum thickness of the disk was near 150 μm. The 150 μm-thick disk was expected to indicate high laser performances in a pulsed regime. The cavity dumped Q-switched thin-disk laser operation which can be modified to the regenerative amplifier was challenged.

4.4.1 Preliminary results

Figure 4.27 indicates the schematic of the setup for the cavity-dumped active Q-switched resonator. The thickness of the Yb:LuAG ceramic disk used was 150 μm. The voltage of 8.8 kV which leads to the transmittance at the TFP of $\approx$ 100% by combination with the QWP was applied to the PC with the repetition rate of 10 kHz and the amplification time of 5 μs. Two photo diodes (PD1 and PD2) were placed in front of a part of the output beam reflected by the wedged plate and behind the convex mirror. PD1 and PD2 have the roles to measure the output pulse profile and the intra-cavity pulse growth, respectively.

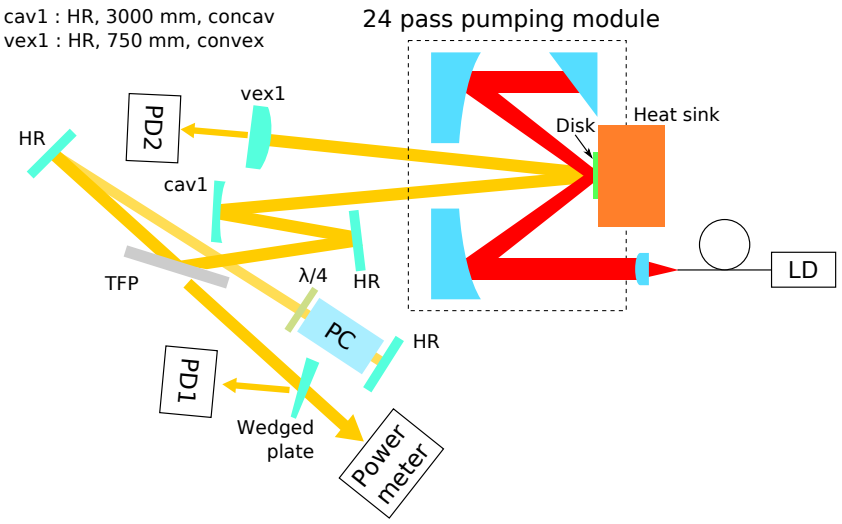

Fig. 4.27: Schematic of the setup for the cavity-dumped Q-switched operation of 150 μm-thick Yb:LuAG ceramic disk.

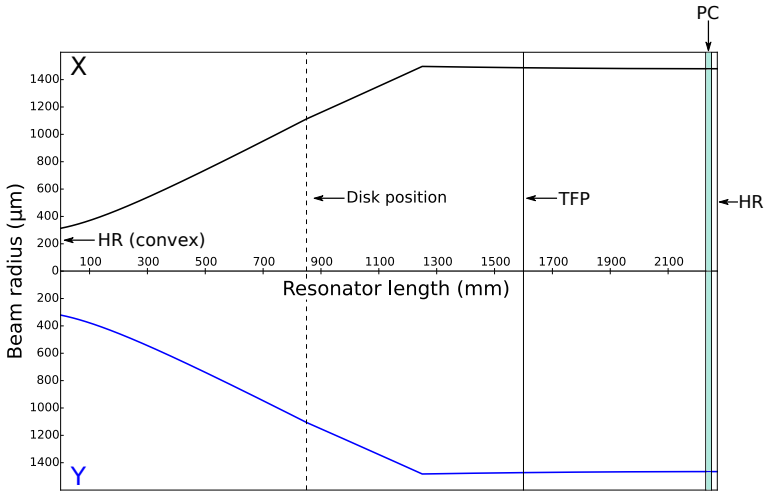

Fig. 4.28: TEM_{00} mode propagation in the cavity-dumped Q-switched resonator. The ROC of the disk for both directions were included in the calculation of the TEM_{00} mode propagation.

In this experiment, the maximum pump power density was limited up to 2 kW/cm^2, corresponding to the maximum pump power of 130 W, because the laser oscillation is terminated during the quarter-wave voltage is not applied to the PC. Exceeding the pump power density of 2 $\sim$ 3 kW/cm^2 without lasing is not desirable to avoid the damage of the disk. The damages of the optics become additional problems under the high energy operation. Figure 4.28 indicates the TEM_{00} mode propagation in the resonator described in Fig. 4.27. The resonator was designed to not only operate in the fundamental-mode regime but also have as large as possible radii at the positions of the TFP, the QWP, and the PC. The smallest radius of the TEM_{00} mode is $\approx$ 300 μm at the position of the convex mirror with the radius of curvature of -750 mm. The expected extractable pulse energy from the resonator of few mJ together with the smallest radius of TEM_{00} mode in the resonator lead to the highest pulse fluence of a few J (e.g. the fluence of 1.7 J/cm^2 for the pulse energy of 5 mJ). It is obviously lower than the damage threshold of the optics and the coatings of a few tens J/cm^2 level.

Figure 4.29 shows the measured pulse train with the oscilloscope. The green curve, the yellow curve, and the purple curve indicate the output pulse, the leak pulse from the convex HR mirror, and the noise from the PC induced by turning on/off of the switches in the bpp-circuit, respectively. In the long time scale (Fig. 4.29 (a)), the pulsed operation with the repetition rate of 10 kHz was observed. The purple curve proved the cavity-dumping were initiated

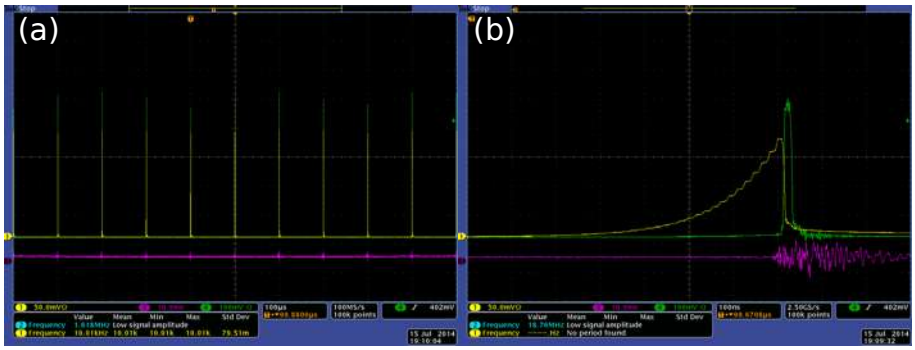

Fig. 4.29: Recorded waveforms in (a) long time span (100 μs/div.) and (b) short time span (100 ns/div.). Green, yellow and purple curve indicate the signal from PD2, PD1, noise of the Pockels-cell, respectively.

by the PC. The waveform in the short time scale (FIg. 4.29) (b)) shows that the pulse evolution inside the resonator and the output pulse. The length of the step-like waveform in the yellow curve corresponding to a round trip time of the resonator of $\approx$ 18 ns. The pulse circulating inside the resonator was growing gradually during the quarter-wave voltage was applied to the PC. The grown pulse was diminished when the quarter-wave voltage was terminated (the point the noise appeared in the purple curve), and then the pulse was extracted from the resonator (green curve). Here, the transmittance at the TFP was $\approx$ 100% since the quarter-wave voltage was applied. The pulse width of the output pulse was correspond to the one round trip time of the resonator of $\approx$ 18 ns. The average output power was 15.4 W at the pump power of 80.2 W (the pump power density 1.2 kW/cm^2) which leads to an optical efficiency of 19%. This is the the first demonstration of the active Q-switched operation of the Yb:LuAG ceramic thin-disk laser.

During the above experiments, the improvement of the average output power was difficult, and the laser operation was a bit instable. The Q-switched laser operation was tested in the multi-mode regime to exclude the possibility of the low gain and instability due to the poor mode matching in the fundamental-mode resonator. Figure 4.30 shows the cavity-dumped active Q-switched resonator operating in the multi-mode regime. The multi-pass resonator was constructed for further improvement of the gain. The TEM_{00} mode propagation in the resonator is indicated in Fig. 4.31. The radii of the TEM_{00} mode on the disk were designed to be the same as possible. The smallest radius of the TEM_{00} inside the resonator of $\approx$ 380 μm leads to lower maximum fluence than that in the previous experiment. The repetition rate and the applied voltage to the PC were the same as the previous experiment.

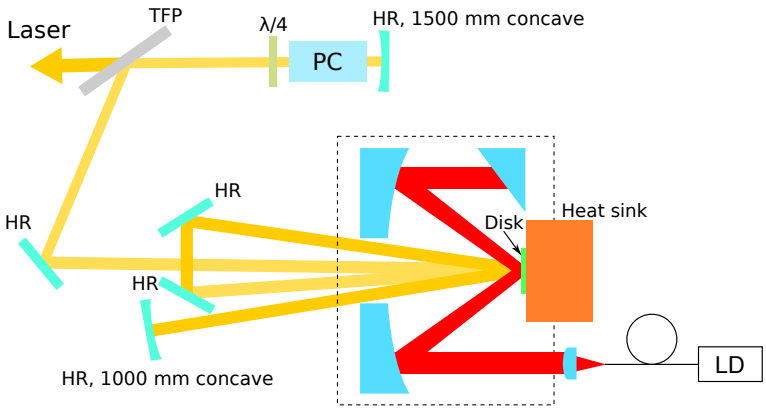

Fig. 4.30: Schematic of the setup for the cavity-dumped Q-switched multi-pass resonator.

The amplification time was set to be 3 μs. With this configuration, a maximum average output power of 36 W at the pump power of 140 W (maximum pump power density 2.6 kW/cm^2). The optical efficiency is calculated to be $\approx$ 26%.

After measuring thee above results were obtained, the average power was suddenly decrease to a few W level due to the damage of the disk. The examples of the magnified photographs which were recorded using a microscope and a CCD camera are shown in Fig. 4.32. Almost all of the damages occurred (Fig. 4.32 (a)) on the front surface of the disk. There is only one damage

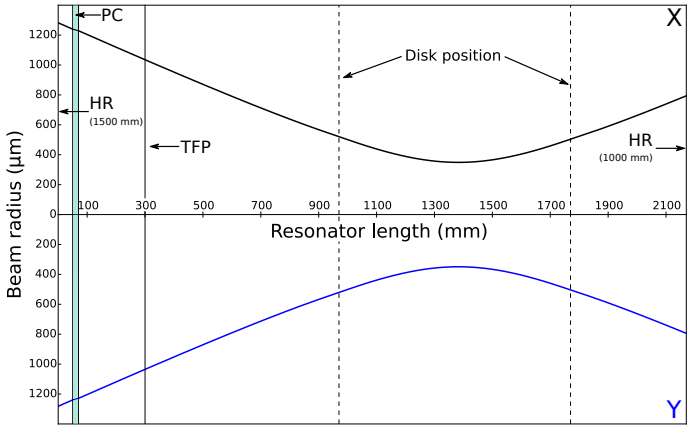

Fig. 4.31: TEM$_{00}$ mode propagation in the cavity-dumped Q-switched multi-pass resonator. The ROC of the disk for both directions were included in the calculation of the TEM$_{00}$ mode propagation.

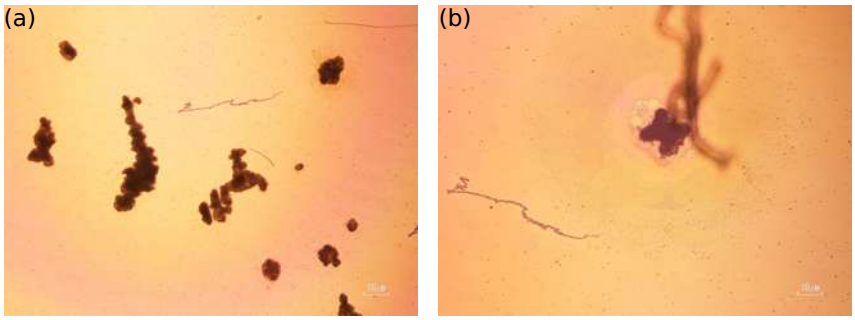

Fig. 4.32: Microscope images of damaged 150 μm-thick disk. (a) Damages occurred on the front surface. (b) A damage occurred in the back surface.

seems to be occurred in the back surface of the disk (Fig. 4.32 (b)). To check whether the damage occurred accidentally or not, the Q-switched laser operation was again tested with the 200 μm-thick disk. The same damages as shown in Fig. 4.32 were again appeared.

The highest pulse energy obtained in this Section was 3.6 mJ (36 W / 10 kHz) from the 150 μm-thick disk tested with the multi-pass resonator. The fluence on the disk led by the pulse energy and the TEM_{00} mode on the disk was roughly 500 mJ/cm^2. It is far from the damage threshold of all of the coatings used in the Q-switching. The damages were expected to be initiated by defects of scratches of the gain medium and coating. The surface of a 5 at.% Yb:LuAG ceramic plate after polishing was checked with the microscope. Figure 4.33 shows the examples of the microscope image of the Yb:LuAG ceramic plate. Though the Yb:LuAG ceramic plate have never used in any experiments, it has large polishing flaws with a size of a few μm $\sim$ a few tens of μm order. The damages are considered to be originated in the scratches on the disk surface. Developing the special polishing technique

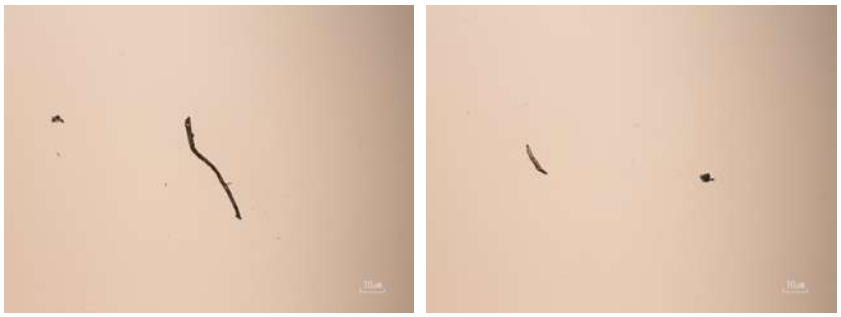

Fig. 4.33: Microscope images of a fresh 5 at.% Yb:LuAG ceramic plate.

to avoid the flaws of the disk has to be necessary to achieve a high energy operation.

4.5 Summary

The potentials of Yb:LuAG ceramic as the gain medium for the thin-disk laser are investigated. The Yb:LuAG ceramic indicates higher microhardness and fracture toughness than those of single crystal. Ther thermal conductivity and the emission cross section at 1030 nm of Yb:LuAG ceramic are high than those of Yb:YAG. Two times larger drop in the thermal conductivity of Yb:LuAG ceramic than that of Yb:LuAG single crystal suggests slight low quality of Yb:LuAG ceramic.

At first, the laser performances of bulk-shaped 10 at.% Yb^{3+}-doped LuAG ceramic were evaluated. In the CW operation regime, the efficient laser oscillation with the slope efficiency of as high as 72% was obtained without AR coating. The slope efficiency is comparable to the current highest slope efficiency obtained with Yb:LuAG single crystal. In the SESAM mode-locking, the first passive mode-locking with a pulse duration of 699 fs and a spectral bandwidth of 1.7 nm was demonstrated when the resonator was optimized to maximize the average output power. The pulse duration can be down to 541 fs with a spectral bandwidth of 2.5 nm by increasing the intra-cavity pulse energy. These results proved the Yb:LuAG ceramic can proceed to the thin-disk laser as the next step.

The first thin-disk laser demonstration has been successfully demonstrated with the 300 μm-thick Yb:LuAG ceramic disk. Results in the multi-mode regime for both soldered and glued disks are summarized in Table 4.9. During the experiment, the disk was broken maybe due to the bad contacting. Then the Yb:LuAG disk with a thickness of 150 μm was tested to check the soldering

Table 4.9: Summary of the laser performances for Yb:LuAG ceramic disks.

Disk	$P_{out,max}$ (W)	η_{o-o} (%)	η_{slope} (%)	Damage
150 μm, solder	50	56	58	Deformed
200 μm, solder	-	-	-	@ 4.6 kW/cm^2
300 μm, solder	101	47	45	@ 3.6 kW/cm^2
150 μm, glue	166	60.3	72.2	-
200 μm, glue	101	56	64	-

quality. Though it indicated higher laser performances than the 300 μm-thick disk without damages and instabilities was observed and the fundamental-mode oscillation could not be observed. The re-measurement of the ROC revealed that the disk was deformed largely, and hence it can be one of the evidence that the our metal layer coating were not optimized for the soldering process at the IFSW.

The thin-disk laser performances of the glued disk with a thickness of 200 μm were evaluated. The first thin-disk laser operation in the multi-mode regime indicated superior performances than those of soldered disks without any damages and instabilities. It is confirmed that the not optimized metal layer coating for the soldering process caused the damages and the instabilities. The first fundamental-mode operation was successfully demonstrated with M^2 of 1.22. The optical efficiency is lower than that demonstrated with Yb:LuAG single crystal. The reason is expected to be the non-optimal thickness of the disk, the scratch flaws on the surface of the disk, and the quality of the Yb:LuAG ceramic. The linearly polarized operation was checked to estimate the depolarization loss which can be a serious problem especially in the thin-disk shaped ceramic. The laser oscillation with the high degree of polarization ($\approx$99.5%) and the low depolarization loss ($\approx$ 0.15% per a round trip) were obtained. This indicates the Yb:LuAG ceramic thin-disk can be used for the laser/amplifier architectures which require the polarization control.

The thin-disk laser operations of the glued 150 μm-thick disk were demonstrated. The multi-mode laser operation indicated the current maximum slope efficiency of as high as 72%. It is almost the same as the highest slope efficiency obtained with the Yb:LuAG single crystal. The optimum thickness is expected to be around 150 μm. Since the high potentials of Yb:LuAG ceramic as the gain medium for the thin-disk laser were revealed from the results demonstrated in the CW regime, the high laser performances were expected under the high energy operation. The cavity-dumped active Q-switched laser operation, which can be modified to the regenerative amplifier, was challenged. The average power of 36 W with the repetition rate of 10 kHz which resulted in the pulse energy of 3.6 mJ was obtained with the 150 μm-thick disk. However, I found surface damages occurred during Q-switching at a much larger fluence than the damage thresholds of coatings. The reason for the damage is consider to be the scratch flaws during the polishing process.

Though the thermal conductivity measurement suggests slight poor quality of the Yb:LuAG ceramic, the thin-disk laser operation of the glued Yb:LuAG ceramic in the multi-mode regime indicate high potential of Yb:LuAG ce-

ramic as the thin-disk gain medium. Currently, the efficiencies with under a diffraction limited beam quality and energy extraction with are expected to be degraded/limited by the surface scratches on the disk. Resolving these problems will led to a regenerative amplifier based on Yb:LuAG ceramic with high energy and high repetition rate (i.e. high average power).

Chapter 5

Yb:Lu_2O_3 ceramics

5.1 Basic properties of Yb:Lu_2O_3 ceramic

Although Yb:LuAG ceramic has the potential for the high energy application due to its high thermal conductivity and large gain, its narrow gain bandwidth makes it difficult to operate in the shorter pulse duration regime below $\approx$ 500 fs with high average output power. Among Yb^{3+}-doped sesquioxides (Yb:RE_2O_3, RE = Y, Lu, Sc), Yb:Lu_2O_3 is especially an attractive gain medium for the high power short pulsed thin-disk laser due to its high thermal conductivity in the heavy doping situation, broad gain bandwidth due to its disordered nature, and possibility to fabricate large-sized Yb:Lu_2O_3 ceramic with high optical quality because of its lower sintering temperature than that of the melting temperature (also phase transition temperature). In this Chapter, the potential of the Yb:Lu_2O_3 ceramic as the gain medium for the thin-disk laser, and the development of our original pump module and bonding processes are discussed.

5.1.1 Mechanical properties

Table 5.1 summarizes the grain size, the microhardness and the fracture toughness of un-doped Lu_2O_3 ceramic and single crystal [74,112]. The average grain size of un-doped Lu_2O_3 ceramic is also controlled to be 1$\sim$2 μm (in two dimensionally), similar to that of un-doped LuAG ceramic. Only the estimated fracture toughness is available for un-doped Lu_2O_3 is available single crystal. Lu_2O_3 ceramic indicates two times larger fracture toughness than that of single crystal.

Table 5.1: Average grain size, microhardness and fracture toughness of un-doped Lu_2O_3 .

	Grain size (μm)	Microhardness (GPa)	Fracture toughness (MPa $m^{1/2}$)
Lu_2O_3 ceramic [112]	1-2	12.5	4.1
Lu_2O_3 single crystal [74]	-	-	2 (estimated)

5.1.2 Thermal properties

The thermal properties of 3 at.% Yb^{3+}-doped Lu_2O_3 ceramic were also measured using the flash method described in Subsection 4.1.2. Table 5.2 summarizes the thermal properties. 3 at.% Yb:Lu_2O_3 ceramic indicates the thermal conductivity of almost 14 W/m·K. Table 5.3 shows the comparison of the thermal conductivities of RE_2O_3s and YAG. Un-doped RE_2O_3s indicate the higher thermal conductivities than un-doped YAG. When Yb^{3+} is doped, the thermal conductivities of both the single crystalline and the ceramic Yb:RE_2O_3s other than Yb:Lu_2O_3 are decreased to almost the same level as that of Yb:YAG. Only Yb:Lu_2O_3 single crystal and ceramic indicate high thermal conductivities. While single crystalline Yb:Lu_2O_3 indicates lower thermal conductivity than that of un-doped Lu_2O_3 with a moderate decline of the thermal conductivity, 3 at.% Yb:Lu_2O_3 ceramic indicates even a higher thermal conductivity than that of un-doped Lu_2O_3 ceramic. The different behavior from single crystall will be ascribed to the different measurement methods for single crystal and ceramic. The un-doped Lu_2O_3 was measured using temperature wave method **??**. There is no available un-doped Lu_2O_3 ceramic sample. I could not measure the thermal conductivity using flash method..

Table 5.2: Thermal properties of 3 at.% Yb^{3+}-doped Lu_2O_3 ceramic.

	thermal diffusivity (mm^2/s)	heat capacity (J/g ·K)	density (g/cm^3)	thermal conductivity (W/m·K)
Yb:Lu_2O_3	4.8 ± 0.1	0.31 ± 0.02	9.42 ± 0.09	13.9 ± 0.8

5.1.3 Spectroscopic properties

Absorption spectrum

Figure 5.1 shows the absorption spectrum of 3 at.% Yb:Lu_2O_3 ceramic measured with the same method as mentioned in Subsection 4.1.3. Yb:Lu_2O_3

Table 5.3: Comparison of the thermal conductivities.

	Thermal conductivity (W/m·K)			
	Un-doped		Yb^{3+}-doped	
	Single crystal	ceramic	Single crystal	ceramic
Sc_2O_3	16.5 [49]	12.5	6.6 (3 at.%) [49]	-
Y_2O_3	13.6 [49]	12.6	7.7 (3 at.%) [49]	7.9 (2 at.%)
Lu_2O_3	12.5 [49]	10.9	11.0 (3 at.%) [49]	13.9 (3 at.%)
YAG	11.0 [49]	9.9	6.8 (3 at.%) [49]	7.76 (1 at.%) [12]

ceramic has its zero-phonon absorption peak at 976 nm with a FWHM of 3 nm, and has a broad absorption band from 900 nm $\sim$ 950 nm. The pump wavelength was chosen as the wavelength of the zero-phonon line to improve the pump absorption.In this Chapter, a thin-disk shaped Yb:Lu_2O_3 ceramic with a heat sink was mounted in our hand-built pumping module (16 passes, the detail will be given in Subsection 5.4.1). The absorption coefficient at 940 nm ($\approx$ 3.2 cm^{-1}) together with the number of the pump beam passes of 16 requires at least a thickness of $\approx$ 1 mm to absorb all of the pump power. For the zero-phonon line pumping, an wavelength stabilization is required. The narrow linewidth of the zero-phonon line makes the total absorption ef-

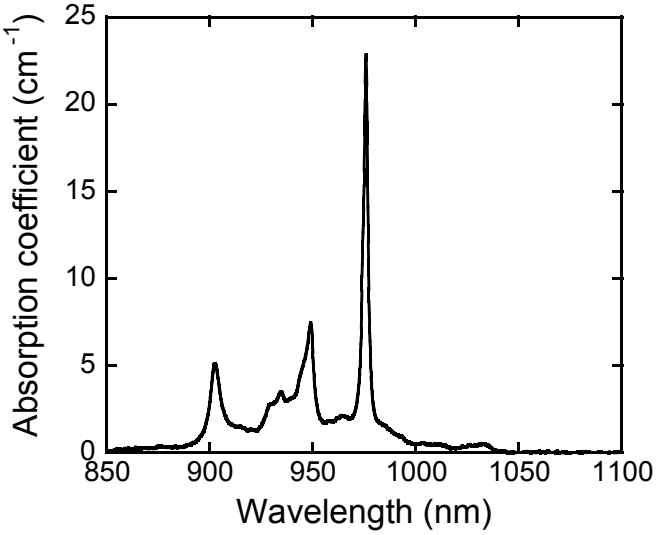

Fig. 5.1: Absorption spectrum of 3 at.% Yb:Lu_2O_3 ceramic.

ficiency sensitive to the wavelength shift caused by heating up and individual differences of the wavelength of diode bars in a LD module. In this Chapter, a volume-bragg grating (VBG) was chosen as the wavelength stabilizer which can provide the sharp emission spectrum with almost no shift of the wavelength.

Emission spectrum

Figure 5.2 shows the emission spectrum of Yb:Lu_2O_3 ceramic calculated with the same method as mentioned in Subsection 4.1.3. The wavelength of the main peak which contributes to the laser operation is 1032 nm with a FWHM of 13 nm. Another peak is located at 1080 nm with a FWHM 15 nm. The gain bandwidth at 1032 nm of Yb:Lu_2O_3 ceramic is broader than that of Yb:YAG (8 nm). While this is the large advantage for the ultrashort pulsed operation, the broader gain bandwidth leads to the smaller emission cross section. Actually, the emission cross section at 1032 nm ($\sigma_{emi} \approx 1.35 \times 10^{-20}$ cm^2) of the Yb:Lu_2O_3 is narrower than that of Yb:YAG ($\sigma_{emi} \approx 2.0 \times 10^{-20}$ cm^2). The luminescence lifetime is measured to be ≈ 820 μs.

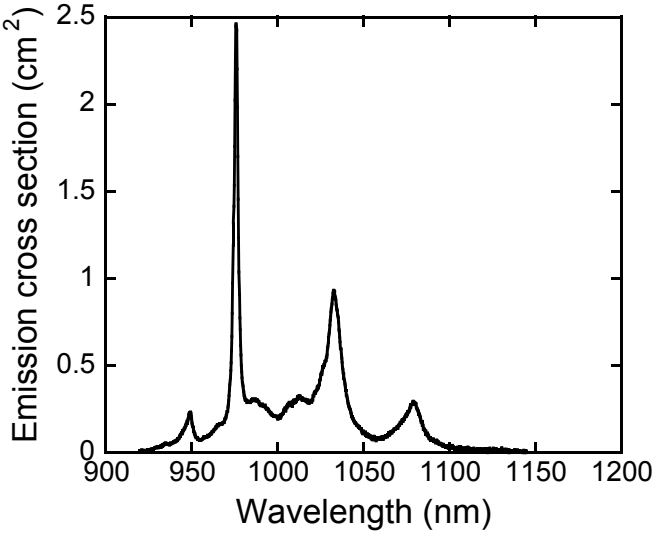

Fig. 5.2: Emission spectrum of 3 at.% Yb:Lu_2O_3 ceramic.

5.1.4 Laser performances of bulk-shaped Yb:Lu_2O_3 ceramics

The investigation of the laser operation of the bulk-shaped Yb:Lu_2O_3 ceramic has been started in 2005. Here, the results are summarized briefly. In the CW regime, a maximum output power of 700 mW with a slope efficiency of 36% at 1035 nm and a maximum output power of 950 mW with a slope efficiency of 53% were demonstrated [85]. In 2006, SESAM-initiated passively mode-locked operation with a shortest pulse duration of 357 fs with an average power of 352 mW and a spectral bandwidth of 3.2 nm was demonstrated [118]. Recently, Kerr-lens mode-locked operation (un-doped Y_2O_3 ceramic was inserted to increase the nonlinearity) with a shortest pulse duration of 65 fs and the spectral bandwidth of 18.9 nm was demonstrated [119]. Though the first report regarding the CW laser operation suggests a bit low quality of Yb:Lu_2O_3 ceramic, the SESAM and the Kerr-lens mode-locked laser demonstrations point out the potential of Yb:Lu_2O_3 ceramic in the mode-locked thin-disk laser operation.

5.2 Contacting

5.2.1 Soldering

The foil type In-Sn (52:48) with a thickness of 50 μm produced by Indium corp. was used for the soldering. A circle-shaped 3 at.% Yb:Lu_2O_3 ceramic disk was prepared with ta diameter and a thickness of 6.3 mm and 300 μm, respectively, without a wedge angle. The coating design of the disk was the same as Yb:LuAG ceramic thin-disk (see Fig. 4.11). The gold coated heat sink was made from oxygen-free copper. It was placed on the hotplate (Pasolina HP-300) to heatup to 150 °C. Then the standard resin based flux was applied on the heat sink to remove the oxidized layer.

The In-Sn foil with a cross sectional size of 5 mm × 5 mm was placed on the heat sink. After the solder was melted, the heat sink with solder was dismounted from the hotplate and cleaned using acetone. The cleaned heat sink with solder was placed on the hotplate and heated again. When the solder was melted, the disk was put on the solder after the flux was applied. Then the heat sink with solder and disk was removed from the hotplate, and cooled naturally.

Figure 5.3 indicates the photograph of the soldered disk. The thickness was measured using a micrometer to be around 30 μm which would led to a

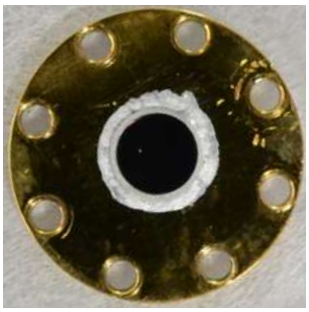

Fig. 5.3: Photograph of soldered Yb:Lu_2O_3 ceramic disk.

bit larger R_{th} than that of HR coating (see Fig. 3.5). After the soldering, the OPD profile and the ROC of the disk were measured with the interferometric technique (details will be discussed in Section 5.3).

5.2.2 Gluing

A 3 at.% Yb:Lu_2O_3 ceramic with a diameter of 6.3 mm, thickness of 250 μm without wedge and the same coating design as the soldered disk was used for the gluing. Because the disk was prepared for the soldering, an unnecessary metal layers existed. The two-pack epoxy resin (301-2, Epoxy Technology [120]), whose basic properties are summarized in Table 5.4, was used. Its low viscosity would accelerate the removal of the bubbles, and make the gluing layer thinner. The heat load by light absorption at the gluing layer should be almost not exist due to a high optical transparency around the pump and the lasing wavelengths (>99%). The recommended cure condition is 80 °C/3 hrs or 23 °C/2 days. It is of course possible to control the hardening speed by changing the surrounding temperature.

The gluing process is much simple compared with the soldering. The oxygen-free copper heat sink without Au coting was placed on the same hotplate as used for the soldering. The temperature of the hotplate was set to be around 100 °C. The mixed epoxy resin with a volume of ≈0.1 μl was dropped on the heat sink, and then the disk was put on it.

Table 5.4: Properties of epoxy resin [120].

Viscosity	Cure condition	Thermal conductivity	Transmittance
225 - 425 cps	80 °C / 3 hrs	N/A	> 99%
@ 100 rpm	23 °C / 2 days		@400-1200 nm

Fig. 5.4: Photograph of glued Yb:Lu_2O_3 ceramic disk.

Figure 5.4 shows the photograph of the glued disk. Checking the gluing layer was not be possible due to existence of the metal layer. The thickness of the gluing layer was too thin to be measured with a micrometer. It was estimated from dropped volume of the epoxy resin to be around 300 nm. It means the R_{th} of the gluing layer is expected to be at least the same or lower than that of the HR coating (see Fig. 3.5). As is the case in the soldered disk, the OPD profile and the ROC of the disk were measured and with the method which will be discussed in Section 5.3.

5.3 Profile and curvature measurement of contacted disks

The profile of the disk affects in the TEM_{00} mode propagation inside the resonator since the disk is used as not only the gain medium, but also one of the resonator mirrors. The disk is desired to have a plane or a spherical profile (concave or convex) because the wavefront distortion introduced by the other surface profiles are difficult to compensate with standard optics. The OPD profile and the ROC of the disk were tried to measured with four interferometric technique. The local ROC and the OPD profile of the disk were measured with the FRCI method and the Fourier-transform method, respectively. The ROC of the disk was calculated from the OPD profile with the Zernike aberration analysis. In this Section, above mentioned techniques will be discussed. The results with other methods will be shown in Appendix A.

5.3.1 Measurement with focus retro-collimated interferometer

Experimental setup

The experimental setup is shown in Fig. 5.5. The probe laser was a fiber-pigtailed distributed feedback LD (DFB-LD) operating at 1061 nm. The beam was collimated by a lens L_5 with the focal length of 11 mm, and was expanded by a pair of lenses L_4 and L_3 whose focal lengths were 150 mm and 200 mm, respectively. The first 50:50 beam splitter (BS1) was placed between the L_4 and the L_3 to reflect the beams which were reflected back from the second 50:50 beam splitter (BS2) as a reference and from the test surface. The focal lengths of both lens L_1 and L_2 were defined to be 300 mm from Fig. 3.12. The measurement process mentioned in Subsection 3.3.3.

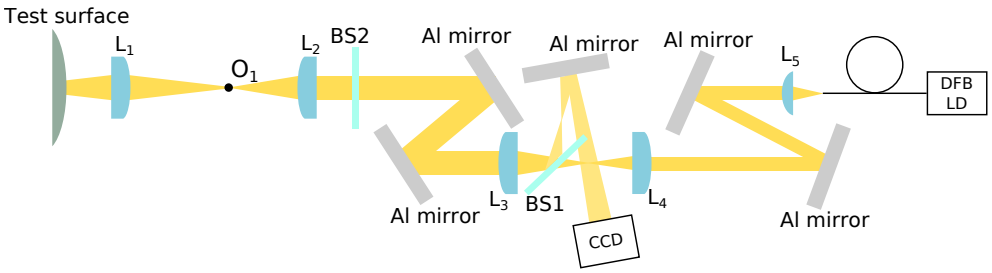

Fig. 5.5: Experimental setup of the FRCI.

Soldered disk

The interference patterns on the CCD at the retro-collimated point are shown in Fig. 5.6. Here, the BS2 was slightly tilted vertically Fig. (5.6 (a)) or horizontally (Fig. 5.6 (b)). The shift amounts x were -9 mm and -11 mm in the horizontal and the vertical directions, respectively. Then the local ROC can be calculated with Eq. (3.22) to be $R_{horizontal} = 10$ m and $R_{vertical} \approx 8.2$ m.

Glued disk

Figure 5.7 indicates the interference patterns of the glued disk. The BS2 was slightly tilted same as is the case in the measurement of the soldered disk (Fig. 5.7 (a) and (b)). The shift amounts x were emasured to be -5 mm for both the horizontal and vertical directions. The ROC for both directions were calculated with Eq. (3.22) to be 18 m.

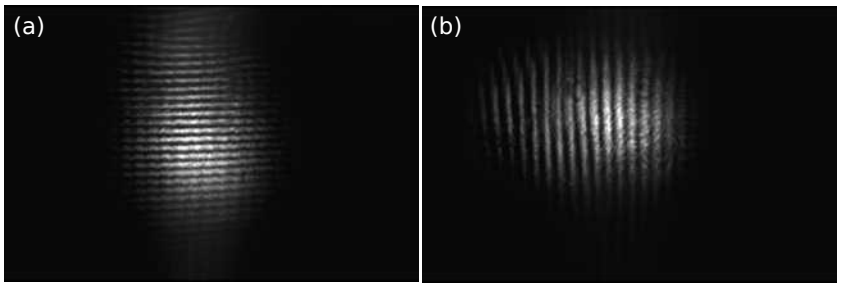

Fig. 5.6: Interference patterns of the soldered Yb:Lu_2O_3 ceramic disk. (a) The reference mirror was slightly tilted in the vertical direction and (b) horizontal direction.

In both disks, the interference patterns indicate incomplete linear fringe patterns. These are estimated to be due to the irregular deformation of the disks. The local ROC of each disk should depend on the measured position. The FRCI method can measure the local ROC whereas cannot measure the profile of the disk directly.

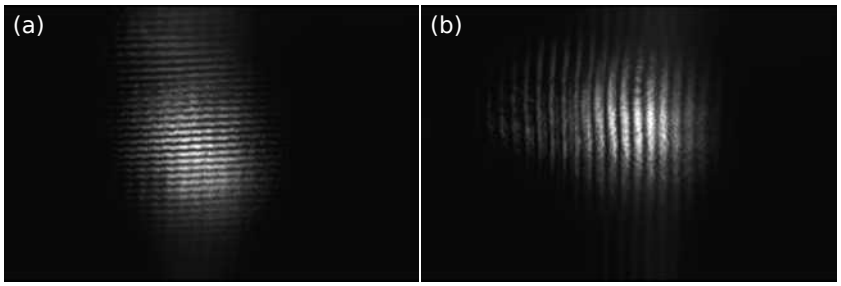

Fig. 5.7: Interference patterns of the glued Yb:Lu_2O_3 ceramic disk. (a) The reference mirror was slightly tilted in the vertical direction and (b) horizontal direction.

5.3.2 Measurement with Fourier-transform method

According to the results obtained with the FRCI method, the profile of the disk was needed to be measured to clarify the deformation of the disk. The FT method was employed to obtain the OPD profile of the disk. Its simple concept, just introducing the spatial carrer frequency, and the capability as the one-shot measurement are the large advantage.

The reference mirror in the MI (see Fig. 3.8) was slightly tilted for both horizontal and vertical directions to introduce the spatial carrier frequencies.

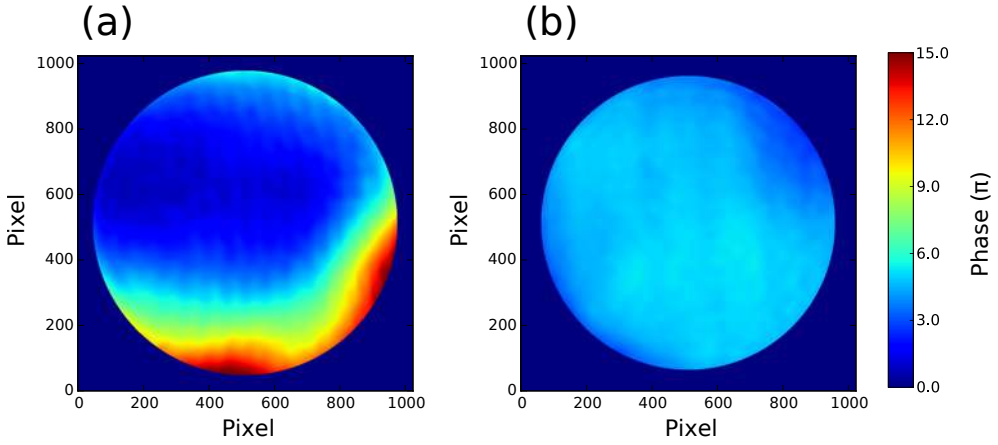

Fig. 5.8: Constructed phase images of (a) soldered disk and (b) glued disk.

The same DFB-LD used in the FRCI was used as the probe laser. The measured interference patterns were converted from the spatial domain to the frequency domain via the discrete Fourier-transform (DFT) to unmerge the spatial carrier components and the signal components. The wrapped phase maps were recovered via the inverse DFT after the spatial carrier components and other noises were filtered out from the frequency map. The phase maps were constructed after the phase unwrapping based on "sorting by reliability following a noncontinuous path algorithm" [121], and are indicated in Fig. 5.8. The phase maps can be converted to the OPD profiles via Eq. (3.34) with a λ of 1061 nm. As expected in Subsection 5.3.1, both disks have deformations.

5.3.3 Zernike fitting

The aberrations of the calculated OPD profiles were analyzed with the Zernike fitting. The amplitudes (a_j) of the Zernike circle polynomials were calculated with Eq. (3.48) and are shown in Fig. 5.9. Using a_j without the piston (Z_1) term and the tilting terms (Z_2, Z_3), the OPD profiles were reconstructed. Figure 5.10 (a) and (b) indicate the reconstructed OPD profiles of the soldered disk and the glued disk, respectively. The ROC of both disks are possible to calculate using a_4, a_5, a_6 corresponding the astigmatism term for $\pm$ 45° directions, the defocus term, and the astigmatism term for 0° and 90° directions, respectively. The angle dependence of the ROC described as

$$R(\theta) = \frac{r_{max}^2}{2[2\sqrt{3}a_5 + \sqrt{6}(a_6 \cos 2\theta + a_4 \sin 2\theta)]} \tag{5.1}$$

where θ is angle and r_{max} is the maximum radial extent [122]. The calculated angle dependences of the ROC are shown in Fig. 5.11 The major and the minor

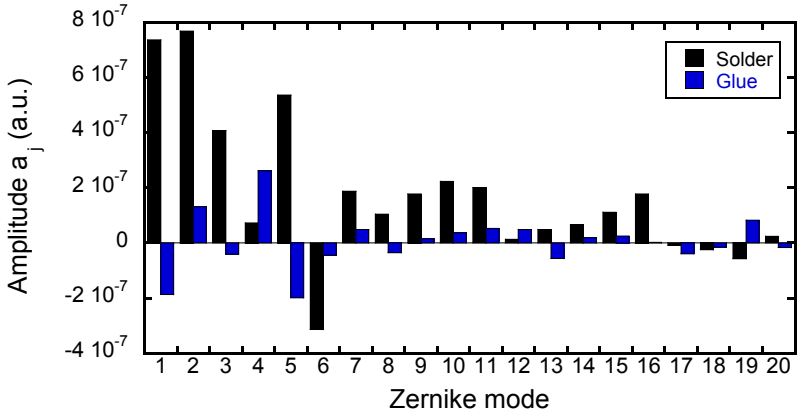

Fig. 5.9: Amplitudes of the Zernike circle polynomials of the soldered disk and the glued disk.

ROC of the soldered disk are ≈ 19 m and ≈ 7.5 m, respectively. Those of glued disk are estimated to be almost flat (≈ -520 m) and ≈ -15 m, respectively. Here, the positive ROC corresponds to the concave surface and vice versa.

The RMS value of both soldered and glued disks is calculated with the below equation for a comparison.

$$RMS_{m,n} = \sqrt{\sum_{m}^{n} a_j^2} \tag{5.2}$$

where a_j is the amplitude of the Zernike circle polynomials (see Fig. 5.9), m and n were order of the Zernike circle polynomials, i.e. $m, n = 1 \sim 20, m < n$. The ratios of "RMS value of the glued disk" divided by "RMS value of the soldered disk" for the spherical aberration terms ($RMS_{4,6}$), the other higher order aberration terms ($RMS_{7,20}$) are ≈ 0.5 and ≈ 0.3, respectively. The glued disk indicates small wavefront aberration than the soldered disk. The higher order aberrations other than the plane terms (1st ∼ 3rd) and the spherical terms (4th ∼ 6th) are difficult to compensate with the standard commercially available optics such as a concave and a convex mirrors. The less aberration in the glued disk would have advantage in the resonator design compared with the soldered disk.

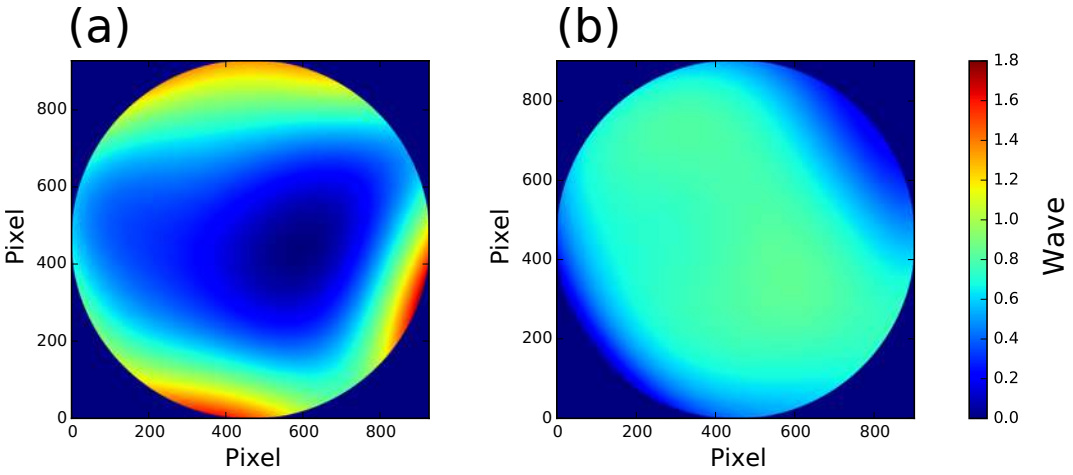

Fig. 5.10: Reconstructed OPD profiles of (a) soldered disk and (b) glued disk without piston and tilting terms. Z_1, Z_2, Z_3 are removed.

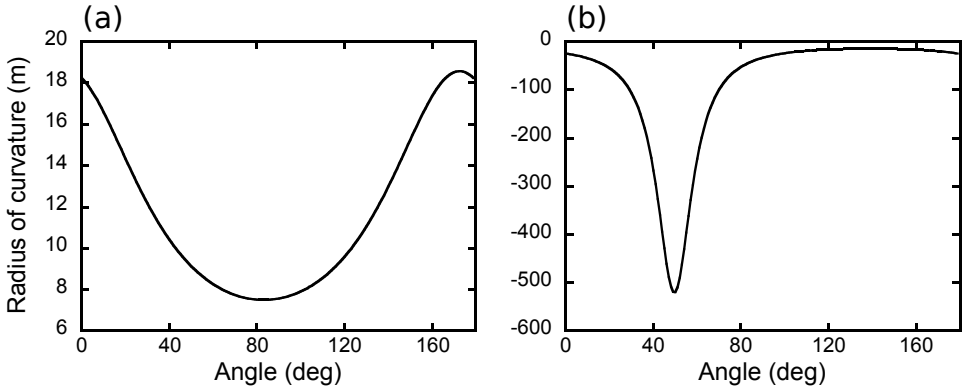

Fig. 5.11: Angle dependence of the radius of curvature for (a) soldered disk and (b) glued disk.

5.4 Thin-disk laser experiments of Yb:Lu_2O_3 ceramic

5.4.1 Multi-pass pumping module

A multi-pass pumping module with the number of passes of 16 was constructed by ourselves. Figure 5.12 shows a design drawing of for the multi-pass pumping module. It is composed of a parabolic mirror with a hole at the center part for the resonator, right angled prism mirrors, and the disk with the heat sink placed at the focal point of the parabolic mirror. The heat sink mentioned in Subsection 5.2.1 is water cooled, and has micro-channels on its water cooled side to achieve efficient heat removal. The temperature of the cooling water is set to be 20 °C with a flow rate of 1.5 l/min.. The prism mirrors with numbers of $N_{pass}/2-1$ are placed in a circle with an angular difference calculated as

$$360^\circ \div \frac{N_{pass}}{2} \tag{5.3}$$

where N_{pass} is the total number of passes. In our case, the required number of prism mirrors are seven (named $P_1 \sim P_7$ in Fig. 5.13), and the angular difference is 45° because N_{pass} is 16. The incident pump beam (initially collimated) is focused onto the disk by the parabolic mirror. The HR coating at the backside of the disk reflects the pump laser beam to the opposite position on the parabolic mirror. The pump beam is then re-collimated and rotates the position on the parabolic mirror via pair of prisms mirrors P_1 and P_2. For the rotation, a tilting angle for the prism mirrors respect to the line connecting the center of the disk and the corresponding prism mirror is described as

$$\frac{180^\circ - 360^\circ \div \frac{N_{pass}}{2}}{2} \tag{5.4}$$

Same processes are repeated during until the pump beam is reached to the P_7. Because the number of passes are limited by the diameter of the pump laser beam on the parabolic mirror or the engineering issue, that is, the clearance between the prism mirrors, there is the case that the pump absorption of the gain medium is still insufficient. The effective way to increase the pump absorption is reflected back the pump laser beam with P_7 as a returning mirror. Based on the design, the hand-build 16 pass pumping module was constructed. The photographs of the actual multi-pass pumping module is shown in Fig. 5.13. The diameter and the focal length of the parabolic mirror is 3 inches and 75 mm, respectively. All of the prism mirror used have a length of 10 mm each side.

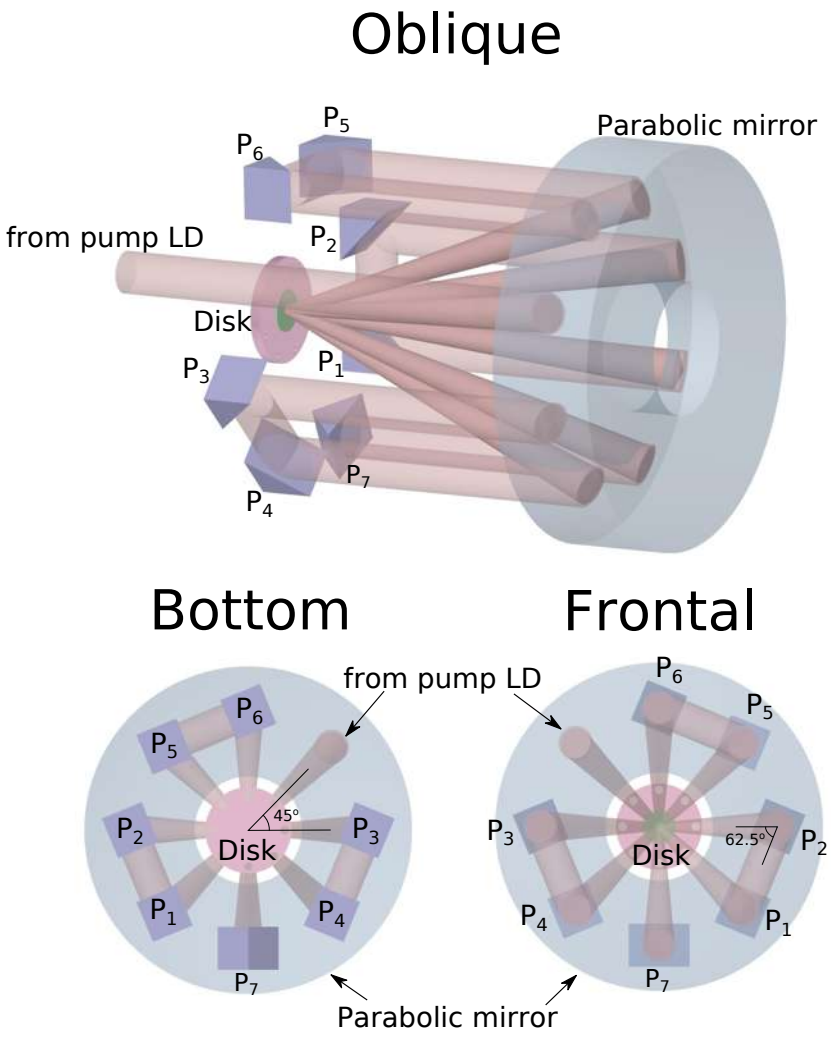

Fig. 5.12: Design drawings of the multi-pass pumping module.

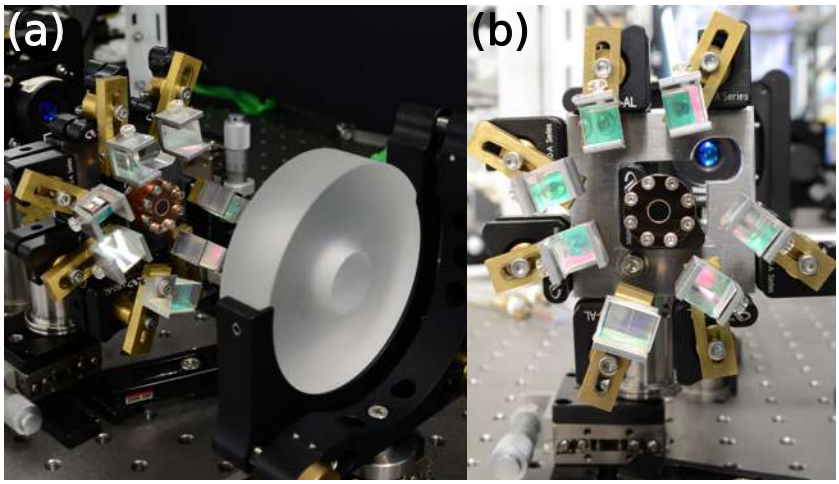

Fig. 5.13: Photographs of hand built multi-pass pumping module. (a) perspective image and (b) frontal image.

5.4.2 Thin-disk laser operations of soldered Yb:Lu_2O_3 ceramic disk

Figure 5.14 indicates the schematic of the setup of the thin-disk laser operation with the soldered disk. The disk with the heat sink was mounted in the 16 pass pumping module. The pump source was the VBG-locked FCLD operating at 976 nm with a maximum pump power of 100 W. Here the pump spot diameter was 1.7 mm which leads to the maximum pump power density of 4.4 kW/cm^2. The I-shaped resonator was composed by a concave OC with a ROC of 500 mm and a transmittance of 3%. To evaluate the maximum laser performance,

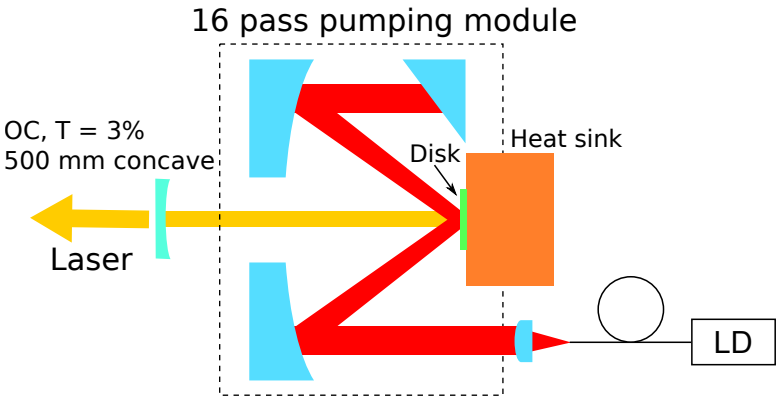

Fig. 5.14: Schematic of the setup for the soldered Yb:Lu_2O_3 ceramic thin-disk laser.

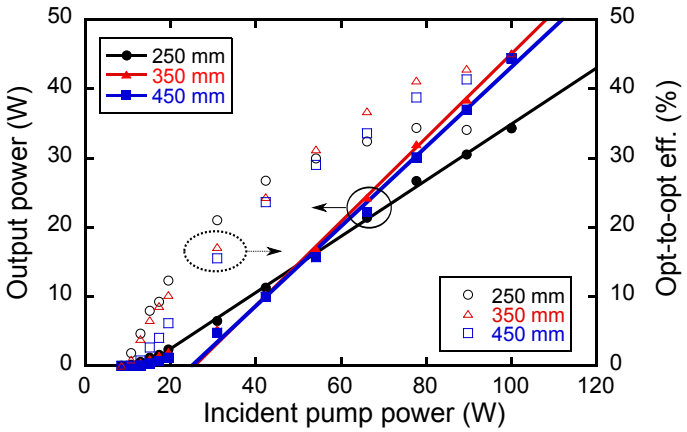

Fig. 5.15: Laser performances of the soldered Yb:Lu_2O_3 ceramic thin-disk.

the multi-mode resonator was constructed. The resonator length was changed from 250 mm to 450 mm to find the optimum position as mentioned in Section 3.5.

The laser performances are shown in Fig. 5.15 and are summarized in Table 5.5. The first thin-disk laser operation of Yb:Lu_2O_3 was successfully obtained with the soldered disk. When the resonator length was set to be 250 mm, a maximum output power of 34 W, a maximum optical efficiency of 34%, a slope efficiency of 41%, and a M^2 at the maximum pump point of 3.2 were obtained. In case of the resonator length of 450 mm, the output power of 44.4 W was obtained with an optical and a slope efficiencies of 60% and 61%, respectively, and a M^2 at the maximum pump point of 6.2. The best performance was obtained with the resonator length of 350 mm: a maximum output power of 45 W with a maximum optical efficiency of 45%, a slope efficiency of 58%, and a M^2 at the maximum pump point of 7.6 were obtained. The lasing wavelength was always around 1034 nm.

Table 5.5: Summary of the laser performances for the soldered Yb:Lu_2O_3 ceramic disk.

$L_{resonator}$ (mm)	P_{out} (W)	η_{o-o} (%)	η_{slope}(%)	M^2
250	34	34	41	3.2
350	45	45	61	7.6
450	44	44	58	6.2

The optical efficiency did not exhibit saturation above 350 mm of the resonator length. There were no signs of roll over. Furthermore, no instability and damages were obtained even the pump power density was close to the normal damage threshold. It means, our soldering method was expected to be successfully working, ant further power extraction can be possible by expanding the pump spot diameter.

5.4.3 Thin-disk laser operations of glued Yb:Lu_2O_3 ceramic disk

The schematic of the laser setup was the same as the previous section. Here, the available maximum pump power was 80 W due to the degradation leading to the slightly lower maximum pump power density of $\approx$ 3.5 kW/cm^2. The resonator length was changed from 150 mm to 350 mm.

Figure 5.16 indicates the laser performances and Table 5.6 summarizes the laser performances. The first thin-disk laser operation was also successfully obtained with the glued disk. A maximum output power of 34 W, a maximum optical efficiency of 43%, a slope efficiency of 55%, and a M^2 at the maximum pump point of 8.7 were obtained with the resonator length of 150 mm. In case of the resonator length of 350 mm, the output power of 34 W was obtained with an optical and a slope efficiencies of 43% and 55%, respectively, and a

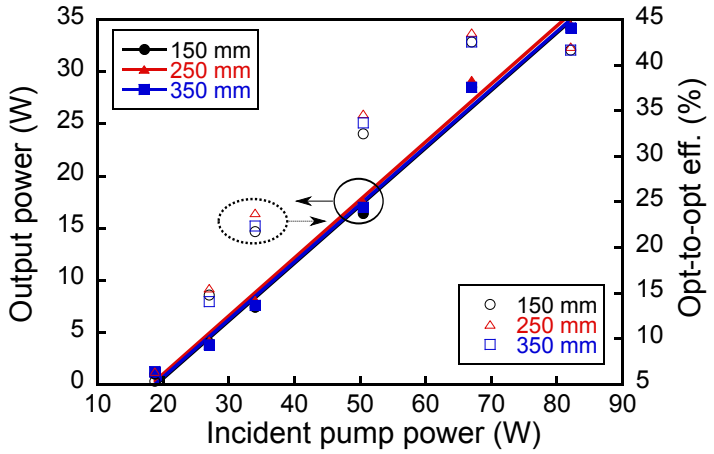

Fig. 5.16: Laser performances of the glued Yb:Lu_2O_3 ceramic thin-disk.

Table 5.6: Summary of the laser performances for the glued Yb:Lu_2O_3 ceramic thin-disk.

$L_{resonator}$ (mm)	P_{out} (W)	η_{o-o} (%)	η_{slope}(%)	M^2
150	34	43	55	8.7
250	35	44	56	9.5
350	34	43	55	9.4

M^2 at the maximum pump point of 9.4. When the resonator length was 250 mm, the best performance was obtained. A maximum output power of 35 W, a maximum optical efficiency of 44%, a slope efficiency of 56%, and a M^2 at the maximum pump point of 9.5 were obtained. The lasing wavelength was always around 1034 nm.

As is the case in the soldered disk, the glued disk indicates stable laser operation. Compared with the slope efficiency of the bulk-shaped Yb:Lu_2O_3 ceramic (in Subsection 5.1.4) of 53%, the Yb:Lu_2O_3 ceramic in the thin-disk geometry indicates improved slope efficiency of 61%. The highest optical and the slope efficiencies in the experiments are lower than those of the current records in the CW thin-disk laser operation based on Yb:Lu_2O_3 single crystal (η_{o-o} of 73% and η_{slope} of 85% [3]). Though the improvement of the quality is estimated from the enhanced slope efficiency, the quality is consider to be still lower than that of single crystal. The hand-built pumping module is another reason for the low efficiencies. The large degree of freedom of the prisms mirrors make the pump spot distribution difficult to achieve the top-flat profile. The further optimizations of the fabrication process and the multi-pass pumping module are necessary to improve the laser performances.

5.4.4 Thermography measurement

Both soldered and glued ceramic disks performed lasing without any damages and instabilities in the previous subsections 5.4.1 and 5.4.2. Thermography measurements under lasing were implemented to estimate the upper limit of the pump power densities of each disk. Figure 5.17 (a) shows the schematic of the setup for the measurement of the thermography of the disk. The same pump LD with the same diameter on the disk as is the subsections 5.4.1 and 5.4.2 were used. Due to the further degradation of the pump LD, the maximum available pump power was 64 W corresponding the maximum pump power density of 2.8 kW/cm^2. The thermographical images of the disk were recorded with a thermography camera (SC655, FLIR Systems, Inc.) placed

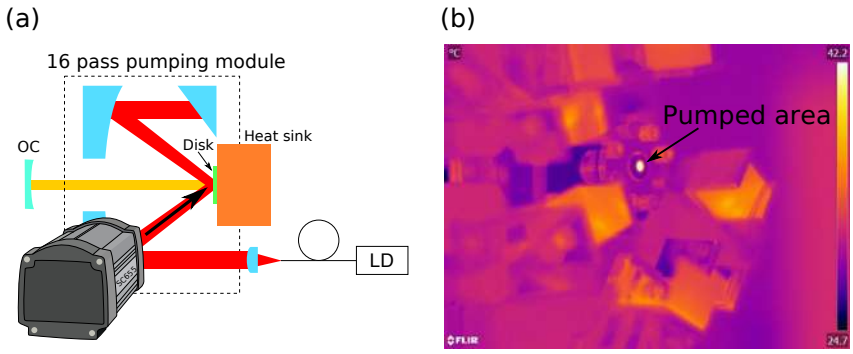

Fig. 5.17: Schematic of the setup for the thermographical measurement.

at the side of the multi-pass pumping module with a distance between the camera and the disk of ≈ 200 mm. An example of an actual thermographical image is shown in left of Fig. 5.17 (b). The number of the pixels covering the pumped area ≈ 20 leads to the spatial resolution of ≈ 85 μ m/pixel. It should be enough fine to analyze the temperature rising of the disk for the radial directions. To obtain the temperature distribution in the depth direction should be impossible.

Figure 5.18 indicates the highest temperatures in the pumped area on the disk with respect to the incident pump powers (the pump power densities). Note that, the highest temperature does not mean the surface temperature of the pumped area. The exact position with the highest temperature cannot be determined. In both disks, the temperatures rose linearly as an increase of the incident pump power. The maximum temperatures were ≈ 62 °C and ≈ 55 °C for the soldered disk and the glued disk, respectively. The glued disk indicated ≈ 20% lower slope of rise in the temperature. From the extrapolation, the tolerance of the maximum pump power density for the soldered disk is estimated to be around 6 kW/cm^2 which is limited by the melting temperature of In-Sn solder of ≈ 120 °C. In case of the glued disk, the true limitation of the maximum pump power density is defined by the maximum operating temperature of the epoxy resin of 200 °C mentioned in the data sheet [120]. The corresponding pump power density giving the temperature of 200 °C reaches almost 15 kW/cm^2. The glued disk has another limitation, i.e. the glass transition temperature. The epoxy resin used for the gluing has the glass transition temperature of ≈ 80 °C. The thermal expansion coefficient above the glass transition temperature increases to almost three times higher than that below the glass transition temperature. It means, the risk of the destruction of the disk dramatically increases above the glass transition temperature. The glued disk should successfully work at least up

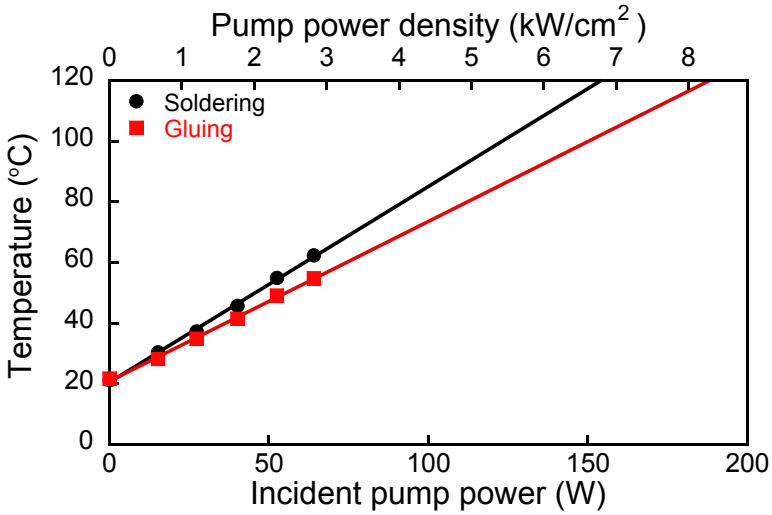

Fig. 5.18: Temperature of the disk with different pump powers.

to 100 °C corresponding the pump power density of ≈ 6kW/cm^2 because the disk was glued at the temperature. Therefore, the practical upper limit of the maximum pump power density can only be expected to be between 6 kW/cm^2 ∼ 15 kW/cm^2. Here, the damage thresholds were estimated from the highest temperature due to difficulty to obtain the temperature distribution in the depth direction as mentioned above. The estimated damage thresholds are possible to increase due to lower temperatures in the contacting layers than the measured highest temperatures.

In both cases, suppressing the temperature rising is necessary to improve the damage threshold of the pump power density. One effective way is to change the heat sink by a diamond one with a thermal conductivity of ≈ 2000 W/m·K. Only the gluing can contact a disk and a diamond heat sink without additional treatment such as extra metal layer coating.

5.5 Summary

The potentials of Yb:Lu_2O_3 ceramic as the gain medium for the thin-disk laser were investigated. The Yb:Lu_2O_3 ceramic has higher thermal conductivity of ≈ 14 W/mK at the doping concentration of 3 at.% and broader gain bandwidth of 13 nm than those of Yb:YAG.

Different from Yb:LuAG ceramic, the thin-disk laser performances of Yb:Lu_2O_3

ceramic were evaluated with our original soldering and gluing techniques and the hand-built 16 pass pumping module. The profiles of the disks after the contacting were measured with several method. Using the FRCI, the local ROC of the soldered disk were measured to be $\approx$ 10 m and $\approx$ 8.2 m, and those of glued disk were measured to be $\approx$ 18 m. While the local ROC were measured, the interference patterns suggested the complicated profile of the disks. The OPD profiles of the disks were measured with the Fourier-transform method. Then they were analyzed with the Zernike circular polynomials. The analysis showed the large higher order aberration of the soldered disk compared with the glued disk.

The thin-disk laser operations were challenged with our hand-built pumping module. The soldered disk showed the current maximum slope efficiency of $\approx$ 60% without instabilities and the damages up to the pump power density of 4.4 kW/cm^2. In the glued disk, the laser oscillation with the maximum slope efficiency of $\approx$ 56% was successfully obtained without any instabilities and damages up to the pump power density of 3.5 kW/cm^2. From these results, the improvement of the quality of Yb:Lu_2O_3 is suggested compared with Yb:Lu_2O_3 ceramic fabricated in 2005 whereas the quality is still lower than that of Yb:Lu_2O_3 single crystal. Not only the quality of Yb:Lu_2O_3 ceramic, but also unoptimized parameters of the hand-built pumping module can be reasons for low efficiencies. The efficiencies are expected to be improved by optimizing the hand-built pumping module and the fabrication process.

The temperature rise of the disks under lasing were measured with a thermocamera. Both disks indicate a linear increase of the temperature rise as an increase of pump powers. The results revealed our contacting methods are successfully established. The glued disk indicates lower temperature rise than that of the soldered disk. In addition, the gluing exhibits the negligible additional heat load in the contacted layer, the small aberration of the disk , the low temperature rising, and the capability to contact a disk and a diamond heat sink. It makes the gluing more promising contacting method than the soldering.

The glued Yb:Lu_2O_3 ceramic with the optimized fabrication process, the polishing process (same as is the case in Yb:LuAG ceramic), the multi-pass pumping module, and contacting process will be led to an ultrashort pulsed laser operation with high average power.

Chapter 6

Conclusions and outlooks

6.1 Conclusions

In this thesis, the performances of the thin-disk lasers based on Yb:LuAG ceramics and Yb:Lu_2O_3 ceramics were evaluated.

Yb:LuAG is one of the important gain media for the thin-disk amplifier architectures due to its improved thermal properties and larger emission cross section than that of Yb:YAG. While Yb:LuAG ceramic has higher thermal conductivity than Yb:YAG under high doping concentration, the drop in the thermal conductivity is nearly two times large than Yb:LuAG single crystal. It suggests the possibility of low quality of Yb:LuAG ceramic. The laser operation of the non-coated bulk-shaped Yb:LuAG ceramic with a doping concentration of 10 at.% was demonstrated. The highest slope efficiency in the CW regime is as high as that demonstrated with single crystal. The first SESAM mode-locked laser operation achieved the current shortest pulse duration compared with other Yb:LuAG ceramics and single crystals. These results are the evidence that the optical quality of Yb:LuAG ceramic is the same as that of Yb:LuAG single crystal.

The Yb:LuAG ceramics with a doping concentration of 10 at.% were contacted with the commercial soldering and gluing techniques. The disks were mounted in the multi-pass pumping module provided by the IFSW, and their maximum laser performances were measured. The highest optical and slope efficiencies of 60% and 72%, respectively, were obtained with the glued disk in the multi-mode regime whereas the soldered disks were damaged or deformed. The efficiencies are the same as the present highest performances for the thin-disk lasers based on Yb:LuAG single crystals. Additionally, the CW

laser operation with the near diffraction limited beam quality, the linearly polarized laser operation with the low depolarization loss were realized. These results show that ceramic can be one of the best gain media for the thin-disk lasers. The current maximum output power leads to the output power density of ≈ 2.5 kW/cm^2. According to the numerical simulation in ref. [123], the extractable power per one disk which is limited by amplified spontaneous emission (ASE) is estimated to be more than 40 kW for a CW operation of Yb:YAG thin-disk laser. It together with the typical pump spot diameter of mm $\sim$ cm lead to the output power density of several hundreds $\sim$ tens of kW/cm^2. It is enough higher than the typical damage threshold of the disk (> 5 kW/cm^2). Therefore, an output power can be simply scaled by expanding the pump spot diameter until the pump power density reaches the damage threshold of the disk. The cavity-dumped active Q-switched laser operation noted the importance of the polishing process for a high energy operation. The scratch flaws on the surface of the disk can introduce the damages, and is possible to reduce the efficiencies. An optimized polishing process will lead to a high energy operation with an improved efficiency.

Yb:Lu_2O_3 is the promising material for ultrashort pulsed lasers with high average output power due to its broader emission gain bandwidth and higher thermal conductivity than those of Yb:YAG. In the thin-disk geometry, 3 at.% Yb:Lu_2O_3 ceramics were evaluated with the new contacting techniques and the 16 pass pumping module. As the contacting methods, the soldering based on In-Sn alloy and the gluing were developed. The local ROC of the contacted disks were measured with FRCI. The interference pattens in the FRCI suggested the complicated profile of the disks. The profiles of the disk were measured with the Fourier-tronsform method and were analyzed with the Zernike fitting. The analysis resulted in the existence of the higher order aberrations in both the glued disk and the soldered disk. Both disks indicated CW thin-disk laser operation without any damages and instabilities up to the maximum pump power density of 4.4 kW/cm^2. The thermographical measurements exhibited linear increase of the temperature of the disk by pumping. The measurements suggest that a laser operation should be possible at a pump power density of more than 6 kW/cm^2. It is higher than the typical damage threshold of 5 kW/cm^2. The results denoted that the new contacting methods can be used for high power thin-disk lasers while an additional process is necessary to control the profile of the disk after the contacting.

6.2 Outlooks

It has been shown that the ceramic materials can be one of the best gain media for the thin-disk lasers. The ability to fabricate ceramic materials with large aperture size, high mechanical strengths, and the homogeneous distributions of density/concentration is favorable for high power/energy operation. The possibility to fabricate ceramic materials with high melting temperature is effective to resolve the serious problem in single crystals. With an improved polishing process, Yb:LuAG ceramic will demonstrate a high energy regenerative amplification. The maximum extractable energy per one disk limited by ASE is suggested to be 3 J in case of Yb:YAG thin-disk [123]. The advantages of Yb:LuAG ceramic in high repetition rate operation is effective to suppress the ASE. Yb:Lu_2O_3 ceramic with improved quality and extended aperture size will realize a mode-locked operation with higher average power than that of single crystal.

The results also showed that the bases of the new contacting methods have been established. Now undesirable higher order aberrations exist in both soldered and glued disks due to the absence of a control mechanisms in the contacting system. Introducing the mechanisms, for example, controlling the parallelism between a disk and a heat sink will suppress higher order aberrations. The improvement of the multi-pass pumping module is also necessary. Too many degrees of freedom in the current design can degrade the pump spot profile on the disk. The positions of the prisms have to be strictly determined. The number of pump beam passes have to be increased to at least 24 because a larger number of pump beam passes leads to smaller thickness of the gain medium.

Appendix

Measurement with Michelson interferometer

As the first measurement in Section 5.3, the simple MI shown in Fig. 3.8 was used. A He-Ne laser was used as the probe light source. The interference pattern was observed by a CCD camera. The measured interference patterns are shown in Fig. 6.2. Figure 6.2 (a) and (b) indicate the interference patterns of the soldered Yb:Lu_2O_3 ceramic disk. Because almost no interference pattern was observed when the both beams were completely overlapped (Fig. 6.2 (a)), the reference mirror was slightly tilted (Fig. 6.2 (b)). Then the linear fringe pattern was observed and thus the ROC of the disk can be estimated only to be flat or too large to measure. Figure 6.2 (c) is the interference pattern of the glued Yb:Lu_2O_3 ceramic disk. The image collected with colors because the interference pattern was too complicated to found out with a gray scale. The ring-like pattern is not the interference pattern. The light reflected by the disk itself had such kind of the complicated beam pattern. With this configuration, obtaining the wavefront information further was almost

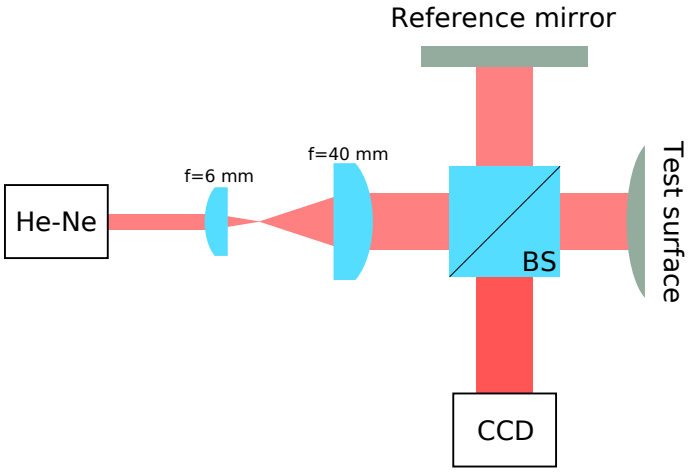

Fig. 6.1: Experimental setup of the Michelson interferometer.

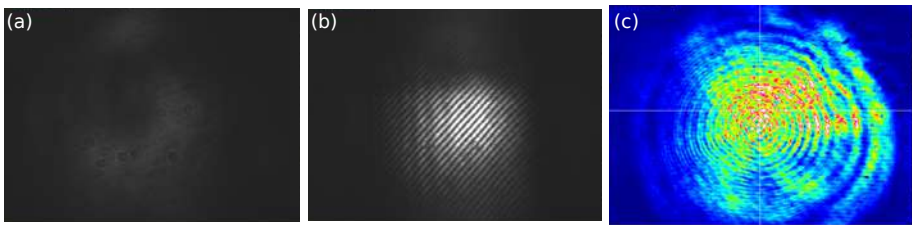

Fig. 6.2: Interference patterns of (a) and (b) soldered Yb:Lu_2O_3 ceramic disk, and (c) glued Yb:Lu_2O_3 ceramic disk.

impossible. For measuring the large ROC, the FRCI (Subsection 5.3.1) was constructed.

Measurement with phase shifting interferometer

The FRCI suggested deformation of the disk. The wavefront information other than local ROC cannot be measured with the FRCI. The PSI was constructed to measure the wavefront profile of the disk. Figure 6.3 shows the schematic of the setup of the PSI. The probe laser was the same as used in the FRCI. The beam was collimated by a lens L_1 with a focal length of 8 mm, and was expanded by a pair of lenses L_2 and L_3 with focal lengths were 150 mm and 200 mm, respectively. The expanded beam was split by the BS. One beam propagated to the reference mirror, and the other propagated to the test surface. The interference pattern was measured by a CCD camera.

The piezoelectric transducer (PZT) was used as the phase shifter. By modulating the applied voltage to the PZT, the phase retardations were in-

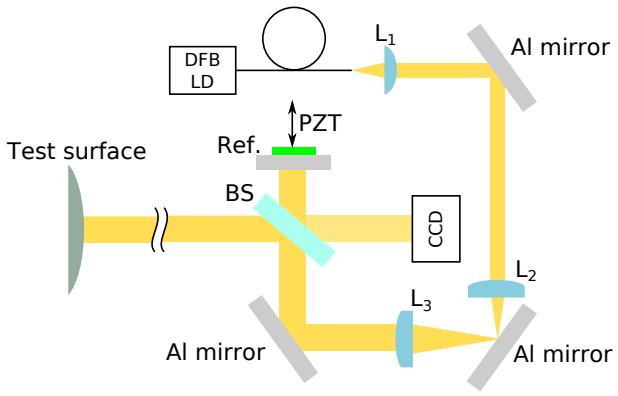

Fig. 6.3: Schematic of the setup for the PSI.

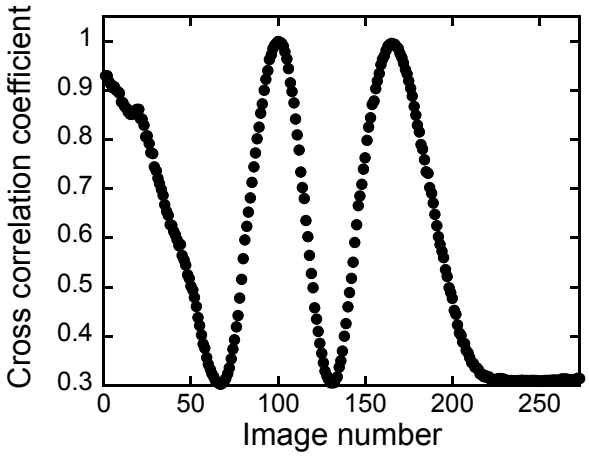

Fig. 6.4: Cross correlation coefficient as a function of the order of the image.

troduced. However, the PZT exhibits a hysteresis and requires an additional process to determine the phase delay. Here, determination of the phase delay was tried by calculating the cross correlation coefficient. By modulating the applied voltage to the PZT, the interference pattern showed the breathing. Taking a movie of this breathing with the CCD camera, then the movie was divided into individual images. One image was defined as the reference. The cross correlation coefficients between each image and the defined reference image were calculated. An example of the calculated cross correlation coefficient as a function of the order of the image is shown in Fig. 6.4. Local maximums and local minimums are observed. The reason why the value of the local minimum is not zero would be the noise. Since the interferometric term is a cosine function, the phase difference $\phi = 0$ and $\phi = \pi$ should correspond the cross correlation coefficient of 0 and 1, respectively. Therefore, the mean value between the local maximum and the local minimum can be estimated as the phase difference of $\frac{\pi}{2}$.

Using the method mentioned above, the profile of the glued disk was measured. Figure 6.5 shows the collected five interference patterns (left five images) and the calculated phase (right image). The actual cross sectional number of pixels of the CMOS camera was 1024×1280. The recorded image was clipped with 1000 pixel $\times$ 1000 pixel for data processing.

The complicated profile was again obtained even after calculating the phase. This would be caused by incorrect phase difference between each in-

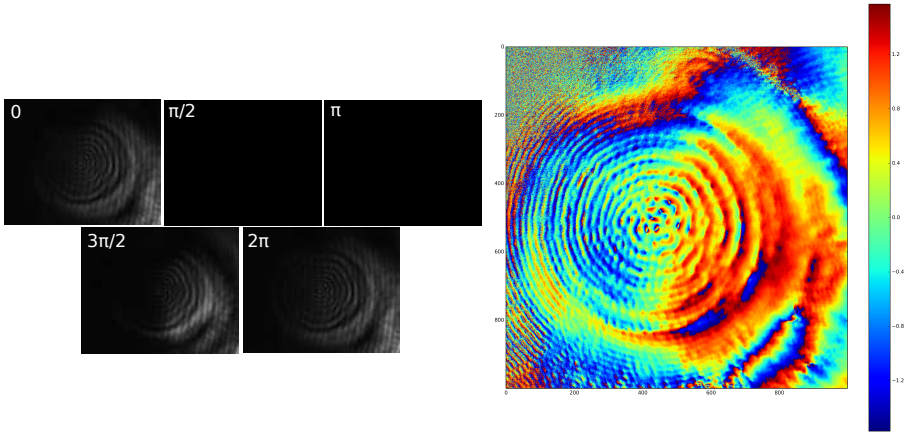

Fig. 6.5: Interferometric images (left) and calculated phase (right).

terference pattern. As mentioned above, the phase delay was determined by taking the cross correlation. The problem of this method is discrete data points. The used CMOS camera can take a movie with 25 frames per second. Hence, the resolution of the data points of the cross correlation coefficients are determined by the scanning rate of the applied voltage to the PZT. In addition, the slow scanning rate of the PZT can have the tendency to be affected easily by the additional disturbances such as the vibration, the atmospheric fluctuation and so on. The problem was resolved with the Fourier-transform method as mentioned in Subsection 5.3.2.

Bibliography

[1] A. Giesen, H. Hügel, A. Voss, K. Wittig, U. Brauch, and H. Opower, "Scalable concept for diode-pumped high-power solid-state lasers," *Applied Physics B*, vol. 58, no. 5, pp. 365–372, 1994.

[2] K. Beil, S. T. Fredrich-Thornton, F. Tellkamp, R. Peters, C. Kränkel, K. Petermann, and G. Huber, "Thermal and laser properties of Yb: LuAG for kW thin disk lasers," *Optics express*, vol. 18, no. 20, pp. 20712–20722, 2010.

[3] R. Peters, C. Krnkel, S. Fredrich-Thornton, K. Beil, K. Petermann, G. Huber, O. Heckl, C. Baer, C. Saraceno, T. Sdmeyer, and U. Keller, "Thermal analysis and efficient high power continuous-wave andmode-locked thin disk laser operation of Yb-doped sesquioxides," *Applied Physics B*, vol. 102, no. 3, pp. 509–514, 2011.

[4] T. H. Geballe and G. W. Hull, "Isotopic and Other Types of Thermal Resistance in Germanium," *Phys. Rev.*, vol. 110, pp. 773–775, May 1958.

[5] S. T. Fredrich-Thornton, C. Hirt, F. Tellkamp, K. Petermann, G. Huber, K.-i. Ueda, and H. Yagi, "Highly doped Yb:YAG Thin-Disk Lasers: A Comparison between Single Crystal and Ceramic Active Media," in *Advanced Solid-State Photonics*, p. WB13, Optical Society of America, 2008.

[6] W. P. Latham, A. Lobad, T. Newell, and D. Stalnaker, "6.5 kW, Yb:YAG ceramic thin disk laser," tech. rep., DTIC Document, 2011.

[7] M. Tokurakawa, A. Shirakawa, K.-i. Ueda, H. Yagi, T. Yanagitani, A. A. Kaminskii, K. Beil, C. Kränkel, and G. Huber, "Continuous wave and mode-locked Yb^{3+}:Y_2O_3 ceramic thin disk laser," *Optics Express*, vol. 20, no. 10, pp. 10847–10853, 2012.

[8] H. Nakao, A. Shirakawa, K.-i. Ueda, H. Yagi, T. Yanagitani, B. Weichelt, K. Wentsch, M. A. Ahmed, and T. Graf, "Demonstration of a Yb^{3+}-

doped $Lu_3Al_5O_{12}$ ceramic thin-disk laser," *Optics Letters*, vol. 39, no. 10, pp. 2884–2887, 2014.

[9] H. Nakao, T. Inagaki, A. Shirakawa, K. ichi Ueda, H. Yagi, T. Yanagitani, A. A. Kaminskii, B. Weichelt, K. Wentsch, M. A. Ahmed, and T. Graf, "Yb^{3+}-doped ceramic thin-disk lasers of Lu-based oxides," *Opt. Mater. Express*, vol. 4, pp. 2116–2121, Oct 2014.

[10] R. Peters, C. Kränkel, K. Petermann, and G. Huber, "Crystal growth by the heat exchanger method, spectroscopic characterization and laser operation of high-purity Yb: Lu_2O_3," *Journal of Crystal Growth*, vol. 310, no. 7, pp. 1934–1938, 2008.

[11] J. Lu, K. Takaichi, T. Uematsu, A. Shirakawa, M. Musha, K.-i. Ueda, H. Yagi, T. Yanagitani, and A. A. Kaminskii, "Yb^{3+}: Y_2O_3 ceramics–a novel solid-state laser material," *Japanese journal of applied physics*, vol. 41, no. 12A, pp. L1373–L1375, 2002.

[12] S. T. Fredrich-Thornton, *Nonlinear Losses in Single Crystalline and Ceramic Yb:YAG Thin-Disk Lasers*. PhD thesis, Universität Hamburg, 2010.

[13] "Trumpf GmbH." `http://www.trumpf.com/de.html`.

[14] "Dausinger + Giesen GmbH." `http://www.dausinger-giesen.de/`.

[15] "Institut für Strhalwerkzeuge." `http://www.ifsw.uni-stuttgart.de/#`.

[16] D. Hanna, J. Jones, A. Large, D. Shepherd, A. Tropper, P. Chandler, M. Rodman, P. Townsend, and L. Zhang, "Quasi-three level 1.03 μm laser operation of a planar ion-implanted Yb:YAG waveguide," *Optics Communications*, vol. 99, no. 3—4, pp. 211 – 215, 1993.

[17] A. Lupei, V. Enaki, V. Lupei, C. Presura, and A. Petraru, "Resonant electron—phonon coupling of Yb^{3+} in YAG," *Journal of Alloys and Compounds*, vol. 275—277, no. 0, pp. 196 – 199, 1998.

[18] J. Fournier and R. Bartram, "Inhomogeneous broadening of the optical spectra of Yb^{3+} in phosphate glass," *Journal of Physics and Chemistry of Solids*, vol. 31, no. 12, pp. 2615 – 2624, 1970.

[19] A. Yariv and P. Yeh, *Photonics: Optical Electronics in Modern Communications*. The Oxford series in electrical and computer engineering, Oxford University Press, 2007.

[20] S.-S. Schad, C. Stolzenburg, K. Michel, and D. Sutter, "Latest Advances in High Brightness Disk Lasers," *Laser Technik Journal*, vol. 11, no. 2, pp. 49–53, 2014.

[21] C. J. Saraceno, F. Emaury, O. H. Heckl, C. R. E. Baer, M. Hoffmann, C. Schriber, M. Golling, T. Südmeyer, and U. Keller, "275 W average output power from a femtosecond thin disk oscillator operated in a vacuum environment," *Opt. Express*, vol. 20, pp. 23535–23541, Oct 2012.

[22] C. J. Saraceno, F. Emaury, C. Schriber, M. Hoffmann, M. Golling, T. Südmeyer, and U. Keller, "Ultrafast thin-disk laser with 80 μJ pulse energy and 242 W of average power," *Opt. Lett.*, vol. 39, pp. 9–12, Jan 2014.

[23] J.-P. Negel, A. Voss, M. A. Ahmed, D. Bauer, D. Sutter, A. Killi, and T. Graf, "1.3 kW average output power Yb:YAG thin-disk multipass amplifier for multi-mJ picosecond laser pulses," in *CLEO: 2014*, p. STu1O.2, Optical Society of America, 2014.

[24] J. Tümmler, R. Jung, H. Stiel, P. V. Nickles, and W. Sandner, "High-repetition-rate chirped-pulse-amplification thin-disk laser system with joule-level pulse energy," *Opt. Lett.*, vol. 34, pp. 1378–1380, May 2009.

[25] M. Schulz, H. Hoeppner, M. Temme, R. Riedel, B. Faatz, M. J. Prandolini, M. Drescher, and F. Tavella, "14 kilowatt burst average power from 2-stage cascaded Yb:YAG thin-disk multipass amplifier," in *Frontiers in Optics 2013*, p. FTu4A.2, Optical Society of America, 2013.

[26] C. Teisset, M. Schultze, R. Bessing, M. Haefner, S. Prinz, D. Sutter, and T. Metzger, "300 W Picosecond Thin-Disk Regenerative Amplifier at 10 kHz Repetition Rate," in *Advanced Solid-State Lasers Congress Postdeadline*, p. JTh5A.1, Optical Society of America, 2013.

[27] C. Teisset, M. Schultze, R. Bessing, M. Häfner, J. Rauschenberger, D. Sutter, and T. Metzger, "Picosecond Thin-Disk Regenerative Amplifier with High Average Power for Pumping Optical Parametric Amplifiers," in *CLEO: 2013 Postdeadline*, p. CTh5C.6, Optical Society of America, 2013.

[28] C. R. E. Baer, C. Kränkel, C. J. Saraceno, O. H. Heckl, M. Golling, R. Peters, K. Petermann, T. Südmeyer, G. Huber, and U. Keller, "Femtosecond thin-disk laser with 141 W of average power," *Opt. Lett.*, vol. 35, pp. 2302–2304, Jul 2010.

[29] C. Schriber, F. Emaury, A. Diebold, S. Link, M. Golling, K. Beil, C. Kränkel, C. J. Saraceno, T. Südmeyer, and U. Keller, "Dual-gain SESAM modelocked thin disk laser based on Yb:Lu_2O_3 and Yb:Sc_2O_3," *Opt. Express*, vol. 22, pp. 18979–18986, Aug 2014.

[30] K. Beil, C. Saraceno, C. Schriber, F. Emaury, O. Heckl, C. Baer, M. Golling, T. Sdmeyer, U. Keller, C. Krnkel, and G. Huber, "Yb-doped mixed sesquioxides for ultrashort pulse generation in the thin disk laser setup," *Applied Physics B*, vol. 113, no. 1, pp. 13–18, 2013.

[31] B. Weichelt, A. Voss, M. A. Ahmed, and T. Graf, "Enhanced performance of thin-disk lasers by pumping into the zero-phonon line," *Opt. Lett.*, vol. 37, pp. 3045–3047, Aug 2012.

[32] R. Peters, C. Kränkel, K. Petermann, and G. Huber, "Broadly tunable high-power Yb:Lu_2O_3 thin disk laser with 80% slope efficiency," *Opt. Express*, vol. 15, pp. 7075–7082, May 2007.

[33] B. Weichelt, K. S. Wentsch, A. Voss, M. A. Ahmed, and T. Graf, "A 670 W Yb:Lu_2O_3 thin-disk laser," *Laser Physics Letters*, vol. 9, no. 2, p. 110, 2012.

[34] R. Peters, C. Krnkel, S. Fredrich-Thornton, K. Beil, K. Petermann, G. Huber, O. Heckl, C. Baer, C. Saraceno, T. Sdmeyer, and U. Keller, "Thermal analysis and efficient high power continuous-wave andmode-locked thin disk laser operation of Yb-doped sesquioxides," *Applied Physics B*, vol. 102, no. 3, pp. 509–514, 2011.

[35] K. Petermann, D. Fagundes-Peters, J. Johannsen, M. Mond, V. Peters, J. Romero, S. Kutovoi, J. Speiser, and A. Giesen, "Highly Yb-doped oxides for thin-disc lasers," *Journal of Crystal Growth*, vol. 275, no. 1—2, pp. 135 – 140, 2005. Proceedings of the 14th International Conference on Crystal Growth and the 12th International Conference on Vapor Growth and Epitaxy.

[36] C. Krnkel, J. Johannsen, R. Peters, K. Petermann, and G. Huber, "Continuous-wave high power laser operation and tunability of Yb:$LaSc_3(BO_3)_4$ in thin disk configuration," *Applied Physics B*, vol. 87, no. 2, pp. 217–220, 2007.

[37] J. Brons, V. Pervak, E. Fedulova, M. Seidel, D. Bauer, D. Sutter, V. Kalashnikov, A. Apolonski, O. Pronin, and F. Krausz, "Power-scaling a kerr-lens mode-locked Yb:YAG thin-disk oscillator via enlarging the

cavity mode in the Kerr-medium," in *CLEO: 2014*, p. SM4F.7, Optical Society of America, 2014.

[38] O. Pronin, J. Brons, C. Grasse, V. Pervak, G. Boehm, M.-C. Amann, V. L. Kalashnikov, A. Apolonski, and F. Krausz, "High-power 200 fs Kerr-lens mode-locked Yb:YAG thin-disk oscillator," *Opt. Lett.*, vol. 36, pp. 4746–4748, Dec 2011.

[39] O. Pronin, J. Brons, C. Grasse, V. Pervak, G. Boehm, M.-C. Amann, A. Apolonski, V. L. Kalashnikov, and F. Krausz, "High-power Kerr-lens mode-locked Yb:YAG thin-disk oscillator in the positive dispersion regime," *Opt. Lett.*, vol. 37, pp. 3543–3545, Sep 2012.

[40] F. Brunner, T. Südmeyer, E. Innerhofer, F. Morier-Genoud, R. Paschotta, V. E. Kisel, V. G. Shcherbitsky, N. V. Kuleshov, J. Gao, K. Contag, A. Giesen, and U. Keller, "240-fs pulses with 22-W average power from a mode-locked thin-disk Yb:$KY(WO_4)_2$ laser," *Opt. Lett.*, vol. 27, pp. 1162–1164, Jul 2002.

[41] G. Palmer, M. Siegel, A. Steinmann, and U. Morgner, "Microjoule pulses from a passively mode-locked Yb:$KY(WO_4)_2$ thin-disk oscillator with cavity dumping," *Opt. Lett.*, vol. 32, pp. 1593–1595, Jun 2007.

[42] G. Palmer, M. Schultze, M. Siegel, M. Emons, U. Bünting, and U. Morgner, "Passively mode-locked Yb:$KLu(WO_4)_2$ thin-disk oscillator operated in the positive and negative dispersion regime," *Opt. Lett.*, vol. 33, pp. 1608–1610, Jul 2008.

[43] F. Brunner, G. J. Spühler, J. A. der Au, L. Krainer, F. Morier-Genoud, R. Paschotta, N. Lichtenstein, S. Weiss, C. Harder, A. A. Lagatsky, A. Abdolvand, N. V. Kuleshov, and U. Keller, "Diode-pumped femtosecond Yb:$KGd(WO_4)_2$ laser with 1.1-W average power," *Opt. Lett.*, vol. 25, pp. 1119–1121, Aug 2000.

[44] A. Diebold, F. Emaury, C. Schriber, M. Golling, C. J. Saraceno, T. Südmeyer, and U. Keller, "SESAM mode-locked Yb:$CaGdAlO_4$ thin disk laser with 62 fs pulse generation," *Opt. Lett.*, vol. 38, pp. 3842–3845, Oct 2013.

[45] O. H. Heckl, C. Kränkel, C. R. E. Baer, C. J. Saraceno, T. Südmeyer, K. Petermann, G. Huber, and U. Keller, "Continuous-wave and modelocked Yb:YCOB thin disk laser: first demonstration and future prospects," *Opt. Express*, vol. 18, pp. 19201–19208, Aug 2010.

[46] U. Buenting, H. Sayinc, D. Wandt, U. Morgner, and D. Kracht, "Regenerative thin disk amplifier with combined gain spectra producing 500 μJ sub 200 fs pulses," *Opt. Express*, vol. 17, pp. 8046–8050, May 2009.

[47] J. Czochralski, "Ein neues Verfahren zur Messung der Kristallisationsgeschwindigheit der Metalle," *Z. phys. Chemie.*, vol. 92, pp. 219–221, 1918.

[48] K. Kitamura, J. Yamamoto, N. Iyi, S. Kirnura, and T. Hayashi, "Stoichiometric $LiNbO_3$ single crystal growth by double crucible Czochralski method using automatic powder supply system," *Journal of crystal growth*, vol. 116, no. 3, pp. 327–332, 1992.

[49] V. Peters, A. Bolz, K. Petermann, and G. Huber, "Growth of high-melting sesquioxides by the heat exchanger method," *Journal of Crystal Growth*, vol. 237, pp. 879–883, 2002.

[50] P. Yang, P. Deng, and Z. Yin, "Concentration quenching in Yb: YAG," *Journal of luminescence*, vol. 97, no. 1, pp. 51–54, 2002.

[51] S. E. Hatch, W. F. Parsons, and R. J. Weagley, "Hot - pressed polycrystalline CaF_2:Dy^{2+} laser," *Applied Physics Letters*, vol. 5, no. 8, pp. 153–154, 1964.

[52] C. Greskovich and J. P. Chernoch, "Polycrystalline ceramic lasers," *Journal of Applied Physics*, vol. 44, no. 10, pp. 4599–4606, 1973.

[53] A. Ikesue, T. Kinoshita, K. Kamata, and K. Yoshida, "Fabrication and Optical Properties of High-Performance Polycrystalline Nd:YAG Ceramics for Solid-State Lasers," *Journal of the American Ceramic Society*, vol. 78, no. 4, pp. 1033–1040, 1995.

[54] J. Lu, M. Prabhu, J. Song, C. Li, J. Xu, K. Ueda, A. Kaminskii, H. Yagi, and T. Yanagitani, "Optical properties and highly efficient laser oscillation of Nd:YAG ceramics," *Applied Physics B*, vol. 71, no. 4, pp. 469–473, 2000.

[55] J. Lu, H. Yagi, K. Takaichi, T. Uematsu, J.-F. Bisson, Y. Feng, A. Shirakawa, K.-I. Ueda, T. Yanagitani, and A. Kaminskii, "110W ceramic Nd^{3+}:$Y_3Al_5O_{12}$ laser," *Applied Physics B*, vol. 79, no. 1, pp. 25–28, 2004.

[56] T. Taira, "Domain-controlled laser ceramics toward giant microphotonics," *Optical Materials Express*, vol. 1, no. 5, pp. 1040–1050, 2011.

[57] A. Patel, M. Levy, R. Grimes, R. Gaume, R. Feigelson, K. McClellan, and C. Stanek, "Mechanisms of nonstoichiometry in $Y_3Al_5O_{12}$," *Applied Physics Letters*, vol. 93, no. 19, p. 191902, 2008.

[58] 柳谷高公, 八木秀喜, and 市川昌文, "イットリウムアルミニウムガーネット微粉体の製造方法." 特許第 3798482 号, April 2006. 特開平 10-101333, April 4, 1998, 特願平 8-274164, Sep. 24, 1996.

[59] 柳谷高公, 八木秀喜, and 山崎裕生, "イットリウムアルミニウムガーネット微粉体の製造方法." 特許第 3692188 号, June 2005. 特開平 10-101411, April 21, 1998, 特願平 8-274165, Sep. 24, 1996.

[60] Y. Sato, J. Akiyama, and T. Taira, "Orientation control of microdomains in anisotropic laser ceramics," *Opt. Mater. Express*, vol. 3, pp. 829–841, Jun 2013.

[61] J. Akiyama, Y. Sato, and T. Taira, "New Generation of Laser Ceramics with Anisotropic Materials," in *Advanced Solid-State Photonics*, p. MF1, Optical Society of America, 2009.

[62] J. Akiyama and T. Taira, "First Demonstration of Rare-Earth-Doped Anisotropic Ceramic Laser," in *CLEO/Europe and EQEC 2011 Conference Digest*, pp. CA1–1, Optical Society of America, 2011.

[63] E. A. Khazanov, "Thermally induced birefringence in Nd:YAG ceramics," *Opt. Lett.*, vol. 27, pp. 716–718, May 2002.

[64] Y. Oishi, T. Dascalu, K. Midorikawa, and T. Taira, "Thermal-Birefringence-Induced Local Depolarization in Thin YAG Ceramic," in *Advanced Solid-State Photonics*, p. MC15, Optical Society of America, 2008.

[65] A. A. Kaminskii, "Laser crystals and ceramics: recent advances," *Laser & Photonics Reviews*, vol. 1, no. 2, pp. 93–177, 2007.

[66] M. J. Weber, *Handbook of optical materials*, vol. 19. CRC press, 2002.

[67] Y.-N. Xu and W. Y. Ching, "Electronic structure of yttrium aluminum garnet ($Y_3Al_5O_{12}$)," *Phys. Rev. B*, vol. 59, pp. 10530–10535, Apr 1999.

[68] B. H. O'Connor and T. M. Valentine, "A neutron diffraction study of the crystal structure of the C-form of yttrium sesquioxide," *Acta Crystallographica Section B*, vol. 25, no. 10, pp. 2140–2144, 1969.

[69] Y. Kuwano, K. Suda, N. Ishizawa, and T. Yamada, "Crystal growth and properties of (Lu, Y)$_3$Al$_5$O$_{12}$," *Journal of crystal growth*, vol. 260, no. 1, pp. 159–165, 2004.

[70] J. Leitner, P. Chuchvalec, D. Sedmidubsk, A. Strejc, and P. Abrman, "Estimation of heat capacities of solid mixed oxides," *Thermochimica Acta*, vol. 395, no. 1—2, pp. 27 – 46, 2002.

[71] J. H. Mun, A. Jouini, A. Novoselov, A. Yoshikawa, T. Kasamoto, H. Ohta, H. Shibata, M. Isshiki, Y. Waseda, G. Boulon, and T. Fukuda, "Thermal and Optical Properties of Yb^{3+} -Doped Y_2O_3 Single Crystal Grown by the Micro-Pulling-Down Method," *Japanese Journal of Applied Physics*, vol. 45, no. 7R, p. 5885, 2006.

[72] L. Kazakova, G. Kuz'micheva, and E. Suchkova, "Growth of y3al5o12 crystals for jewelry," *Inorganic Materials*, vol. 39, no. 9, pp. 959–970, 2003.

[73] R. L. Aggarwal, D. J. Ripin, J. R. Ochoa, and T. Y. Fan, "Measurement of thermo-optic properties of $Y_3Al_5O_{12}$, $Lu_3Al_5O_{12}$, $YAiO_3$, $LiYF_4$, $LiLuF_4$, BaY_2F_8, $KGd(WO_4)_2$, and $KY(WO_4)_2$ laser crystals in the 80 —300K temperature range," *Journal of Applied Physics*, vol. 98, no. 10, pp. –, 2005.

[74] J. Sanghera, W. Kim, G. Villalobos, B. Shaw, C. Baker, J. Frantz, B. Sadowski, and I. Aggarwal, "Ceramic laser materials," *Materials*, vol. 5, no. 2, pp. 258–277, 2012.

[75] V. Cardinali, E. Marmois, B. Le Garrec, and G. Bourdet, "Determination of the thermo-optic coefficient dn/dT of ytterbium doped ceramics (Sc_2O_3, Y_2O_3, Lu_2O_3, YAG), crystals (YAG, CaF_2) and neodymium doped phosphate glass at cryogenic temperature," *Optical Materials*, vol. 34, no. 6, p. 990, 2012.

[76] "VESTA." `http://jp-minerals.org/vesta/jp/`.

[77] A. Senyshyn and L. Vasylechko, "Low Temperature Crystal Structure Behaviour of Complex Yttrium Aluminium Oxides $YAlO_3$ and $Y_3Al_5O_{12}$," *Acta Physica Polonica A*, vol. 124, no. 2, pp. 329–335, 2013.

[78] M. E. Wieser and T. B. Coplen, "Atomic weights of the elements 2009 (IUPAC Technical Report)," *Pure and Applied Chemistry*, vol. 83, no. 2, pp. 359–396, 2010.

[79] G. Bogomolova, D. Vylegzhanin, and A. Kaminskii, "Spectral and lasing investigations of garnets with Yb^{3+} ions," *Zh. Eksp. Teor. Fiz*, vol. 69, p. 860, 1975.

[80] C. W. Xu, D. W. Luo, J. Zhang, H. Yang, X. P. Qin, W. D. Tan, and D. Y. Tang, "Diode pumped highly efficient Yb:$Lu_3Al_5O_{12}$ ceramic laser," *Laser Physics Letters*, vol. 9, no. 1, p. 30, 2012.

[81] H. Nakao, A. Shirakawa, K. ichi Ueda, H. Yagi, and T. Yanagitani, "CW and mode-locked operation of Yb^{3+}-doped $Lu_3Al_5O_{12}$ ceramic laser," *Opt. Express*, vol. 20, pp. 15385–15391, Jul 2012.

[82] H. Nakao, A. Shirakawa, K. ichi Ueda, A. A. Kaminskii, S. Kuretake, N. Tanaka, Y. Kintaka, K. Kageyama, H. Yagi, and T. Yanagitani, "Investigation of the laser and optical properties of Nd^{3+}:Ba(Zr, Mg, Ta)O_3 ceramic, $Nd^{3+}(Na^+)$:$Ca_2MgSi_2O_7$ single crystal, and Yb^{3+}:$Lu_3Al_5O_{12}$ ceramic," *Optical Materials*, vol. 35, no. 4, pp. 700 – 703, 2013. 7th {LCS}.

[83] M. Siebold, M. Loeser, F. Roeser, M. Seltmann, G. Harzendorf, I. Tsybin, S. Linke, S. Banerjee, P. D. Mason, P. J. Phillips, K. Ertel, J. C. Collier, and U. Schramm, "High-energy, ceramic-disk Yb:LuAG laser amplifier," *Opt. Express*, vol. 20, pp. 21992–22000, Sep 2012.

[84] M. Guzik, J. Pejchal, A. Yoshikawa, A. Ito, T. Goto, M. Siczek, T. Lis, and G. Boulon, "Structural Investigations of Lu_2O_3 as Single Crystal and Polycrystalline Transparent Ceramic," *Crystal Growth & Design*, vol. 14, no. 7, pp. 3327–3334, 2014.

[85] K. Takaichi, H. Yagi, A. Shirakawa, K. Ueda, S. Hosokawa, T. Yanagitani, and A. Kaminskii, "Lu_2O_3:Yb^{3+} ceramics–a novel gain material for high-power solid-state lasers," *physica status solidi (a)*, vol. 202, no. 1, pp. R1–R3, 2005.

[86] J. Sanghera, J. Frantz, W. Kim, G. Villalobos, C. Baker, B. Shaw, B. Sadowski, M. Hunt, F. Miklos, A. Lutz, and I. Aggarwal, "10% Yb^{3+}-Lu_2O_3 ceramic laser with 74% efficiency," *Opt. Lett.*, vol. 36, pp. 576–578, Feb 2011.

[87] P. Klopp, *New Yb^{3+}-doped laser materials and their application in continuous-wave and mode-locked lasers.* PhD thesis, Humboldt-Universität zu Berlin, 2006.

[88] C. Stewen, K. Contag, M. Larionov, A. Giesen, and H. Hugel, "A 1-kW CW thin disc laser," *Selected Topics in Quantum Electronics, IEEE Journal of*, vol. 6, pp. 650–657, July 2000.

[89] D. M. Jacobson and G. Humpston, "Gold coatings for fluxless soldering," *Gold Bulletin*, vol. 22, no. 1, pp. 9–18, 1989.

[90] "Indium Corporation, Technical document of solders." `http://www.indium.com/thermal-interface-materials/ribbon-and-foil/solder_ribbon_and_foil_97621_a4_r4.pdf`.

[91] J. G. Speight *et al.*, *Lange's handbook of chemistry*, vol. 1. McGraw-Hill New York, 2005.

[92] D. Malacara, *Optical shop testing*, vol. 59. John Wiley & Sons, 2007.

[93] Y. Xiang, "Focus retrocollimated interferometry for long-radius-of-curvature measurement," *Appl. Opt.*, vol. 40, pp. 6210–6214, Dec 2001.

[94] J. Schmit, K. Creath, and M. Kujawinska, "Spatial and temporal phase-measurement techniques: a comparison of major error sources in one dimension," *Proc. SPIE*, vol. 1755, pp. 202–211, 1993.

[95] J. Schmit and K. Creath, "Extended averaging technique for derivation of error-compensating algorithms in phase-shifting interferometry," *Applied Optics*, vol. 34, no. 19, pp. 3610–3619, 1995.

[96] M. Takeda, H. Ina, and S. Kobayashi, "Fourier-transform method of fringe-pattern analysis for computer-based topography and interferometry," *J. Opt. Soc. Am.*, vol. 72, pp. 156–160, Jan 1982.

[97] R. J. Noll, "Zernike polynomials and atmospheric turbulence," *J. Opt. Soc. Am.*, vol. 66, pp. 207–211, Mar 1976.

[98] N. Hodgson and H. Weber, *Laser resonators and beam propagation.* Springer, 2005.

[99] G. Smith, "The early laser years at Hughes Aircraft Company," *Quantum Electronics, IEEE Journal of*, vol. 20, pp. 577–584, Jun 1984.

[100] W. Koechner, *Solid-state laser engineering*, vol. 1. Springer, 2006.

[101] A. Inam, M. S. Hegde, X. D. Wu, T. Venkatesan, P. England, P. F. Miceli, E. W. Chase, C. C. Chang, J. M. Tarascon, and J. B. Wachtman, "As - deposited high T_c and J_c superconducting thin films made at low

temperatures," *Applied Physics Letters*, vol. 53, no. 10, pp. 908–910, 1988.

[102] A. H. Clauer, "Laser shock peening for fatigue resistance," *Surface performance of titanium*, pp. 217–230, 1996.

[103] R. Sattmann, V. Sturm, and R. Noll, "Laser-induced breakdown spectroscopy of steel samples using multiple Q-switch Nd:YAG laser pulses," *Journal of Physics D: Applied Physics*, vol. 28, no. 10, p. 2181, 1995.

[104] R. J. Collins and P. Kisliuk, "Control of Population Inversion in Pulsed Optical Masers by Feedback Modulation," *Journal of Applied Physics*, vol. 33, no. 6, pp. 2009–2011, 1962.

[105] R. C. Benson and M. R. Mirarchi, "The Spinning Reflector Technique for Ruby Laser Pulse Control," *Military Electronics, IEEE Transactions on*, vol. 8, pp. 13–21, Jan 1964.

[106] W. Buchman, W. Koechner, and D. Rice, "Vibrating mirror as a repetitive Q switch," *Quantum Electronics, IEEE Journal of*, vol. 6, pp. 747–749, Nov 1970.

[107] R. Chesler, M. Karr, and J. Geusic, "An experimental and theoretical study of high repetition rate Q-switched Nd: YAlG lasers," *Proceedings of the IEEE*, vol. 58, no. 12, pp. 1899–1914, 1970.

[108] G. B. Michelangeli, G. Giuliani, E. Palange, and E. Penco, "Q switching and cavity dumping of a high-power cw Nd:YAG laser by means of a novel electro-optic configuration," *Opt. Lett.*, vol. 11, pp. 360–362, Jun 1986.

[109] "Manual of Pockels cell driver, Model PCD-bpp, BEM Bergmann."

[110] "Leysop LTD., BBO Pockels-cell." `http://www.leysop.com/bbo_pockels_cell.htm`.

[111] T. Bridges and P. Cheo, "Spontaneous self-pulsing and cavity dumping in a CO_2 laser with electro-optic q-switching," *Applied Physics Letters*, vol. 14, pp. 262–264, 1969.

[112] M. S. Akchurin, R. Gainutdinov, I. Kupenko, K. Yagi, K. Ueda, A. Shirakava, and A. Kaminskii, "Lutetium-aluminum garnet laser ceramics," in *Doklady Physics*, vol. 56, pp. 589–592, Springer, 2011.

[113] M. I. MENDELSON, "Average Grain Size in Polycrystalline Ceramics," *Journal of the American Ceramic Society*, vol. 52, no. 8, pp. 443–446, 1969.

[114] W. J. Parker, R. J. Jenkins, C. P. Butler, and G. L. Abbott, "Flash Method of Determining Thermal Diffusivity, Heat Capacity, and Thermal Conductivity," *Journal of Applied Physics*, vol. 32, no. 9, pp. 1679–1684, 1961.

[115] W. F. Krupke, M. D. Shinn, J. E. Marion, J. A. Caird, and S. E. Stokowski, "Spectroscopic, optical, and thermomechanical properties of neodymium- and chromium-doped gadolinium scandium gallium garnet," *J. Opt. Soc. Am. B*, vol. 3, pp. 102–114, Jan 1986.

[116] J. Dong, K. Ueda, and A. A. Kaminskii, "Laser-diode pumped efficient Yb:LuAG microchip lasers oscillating at 1030 and 1047 nm," *Laser Physics Letters*, vol. 7, no. 10, p. 726, 2010.

[117] "IFSW, B1 module." `http://www.ifsw.uni-stuttgart.de/produkte/pdf/1406_IFSW_HO_TDPumpModules_end.pdf`.

[118] M. Tokurakawa, K. Takaichi, A. Shirakawa, K. Ueda, H. Yagi, S. Hosokawa, T. Yanagitani, and A. A. Kaminskii, "Diode-pumped mode-locked Yb^{3+}:Lu_2O_3 ceramic laser," *Opt. Express*, vol. 14, pp. 12832–12838, Dec 2006.

[119] M. Tokurakawa, *Kerr-lens mode locked lasers based on Yb^{3+}-doped materials*. PhD thesis, University of Electro-Communications, 2010.

[120] "Epoxy Technology, Technical document of epoxy resin 301-2." `http://www.epotek.com/site/administrator/components/com_products/assets/files/Style_Uploads/301-2.pdf`.

[121] M. A. Herráez, D. R. Burton, M. J. Lalor, and M. A. Gdeisat, "Fast two-dimensional phase-unwrapping algorithm based on sorting by reliability following a noncontinuous path," *Appl. Opt.*, vol. 41, pp. 7437–7444, Dec 2002.

[122] J. Schwiegerling, J. E. Greivenkamp, and J. M. Miller, "Representation of videokeratoscopic height data with Zernike polynomials," *JOSA A*, vol. 12, no. 10, pp. 2105–2113, 1995.

[123] A. Giesen and J. Speiser, "Fifteen years of work on Thin-Disk Lasers: Results and Scaling Laws," *Selected Topics in Quantum Electronics, IEEE Journal of*, vol. 13, pp. 598–609, May 2007.

List of Publications

List of Publications Related to the Thesis

Scientific Journals

1. H. Nakao, T. Inagaki, A. Shirakawa, K. Ueda, H. Yagi, T. Yanagitani, A. A. Kaminskii, B. Weichelt, K. Wentsch, M. Abdou Ahmed, and T. Graf, "Yb^{3+}-doped ceramic thin-disk lasers of Lu-based oxides," Opt. Mat. Express **4**, 2116-2121 (2014).

2. H. Nakao, A. Shirakawa, K. Ueda, H. Yagi, T. Yanagitani, B. Weichelt, K. Wentsch, M. Abdou Ahmed, and T. Graf,“ Demonstration of a Yb^{3+}-doped $Lu_3Al_5O_{12}$ ceramic thin-disk laser, ” Opt. Lett. **39**, 2884-2887 (2014).

3. H. Nakao, A. Shirakawa, K. Ueda, A. A. Kaminskii, S. Kuretake, N. Tanaka, Y. Kintaka, K. Kageyama, H. Yagi, and T. Yanagitani, “ Investigation of the laser and optical properties of Nd^{3+}:Ba(Zr, Mg, Ta)O_3 ceramic, $Nd^{3+}(Na^+)$:$Ca_2MgSi_2O_7$ single crystal, and Yb^{3+}:$Lu_3Al_5O_{12}$ ceramic, ” Opt. Materials **35** 700-703 (2013).

4. H. Nakao, A. Shirakawa, K. Ueda, H. Yagi, and T. Yanagitani, “ CW and mode-locked operation of Yb^{3+}-doped $Lu_3Al_5O_{12}$ ceramic laser, ” Opt. Express **20**, 15385-15391 (2012).

List of Other Publications

Scientific Journals

1. A. A. Kaminskii, H. Nakao, A. Shirakawa, K. Ueda, J. Liebertz, P. Becker, L. Bohaty, “ CW one-micron($^4F_{3/2} \rightarrow {}^4I_{11/2}$) laser oscillation of Nd^{3+} ions in the melilite-type crystal $Ca_2MgSi_2O_7$:$Nd^{3+}(Na^+)$ at its incommensurate-commensurate phase transition, ” App. Phys. B **103**, 629-635 (2011).

2. A. A. Kaminskii, H. Nakao, L. Bohaty, P. Becker, J. Liebertz, R. Kleinschrodt, K. Ueda, A. Shirakawa, " Stimulated emission ($^4F_{3/2} \rightarrow {}^4I_{11/2}$ channel) with LD and Xe-flashlamp pumping of tetragonal, incommensurately modulated $Ca_2MgSi_2O_7$:Nd^{3+}(Na^+) - a new disordered laser crystal, " Laser Phys. Lett. **7**, 876-883 (2010).

International conferences

Talks

1. Y. Higashi, H. Nakao, A. Shirakawa, K. Ueda, A. A. Kaminskii, S. Kuretake, Y. Kintaka, K. Murayama, and N. Tanaka, " Femtosecond Mode-Locked Nd^{3+}-doped Ba(Zr,Mg,Ta)O_3 Ceramic Laser, " Advanced Solid-State Lasers (ASSL) 2014, paper AM4A5, Shanghai, China, Nov. 17, 2014. (accepted)

2. H. Nakao, "Potential of ceramic materials for thin-disk lasers," Second MIPT-UEC Joint Workshop on Optical Science, Chofu, Oct. 16-20, 2014. (accepted)

3. H. Nakao, T. Inagaki, M. Tokurakawa, A. Shirakawa, K. Ueda, A. A. Kaminskii, H. Yagi, T. Yanagitani, B. Weichelt, K. Wentsch, M. Abdou Ahmed, and T. Graf, "Ceramic Thin-disk Lasers, "Stuttgart Laser Technology Forum 2014 (STL'14), paper Di18, Stuttgart, Germany, June 24, 2014. (Invited talk)

4. Y. Higashi, T. Tomita, J. Fuse, H. Nakao, A. Shirakawa, K. Ueda, A. A. Kaminskii, S. Kuretake, Y. Kintaka, K. Murayama, and N. Tanaka, " Femtosecond Mode-locked Nd^{3+}-doped Ba(Zr,Mg,Ta)O_3 Ceramic Laser, "3rd Advanced Lasers and Photon Sources (ALPS '14), paper ALPS8-5, Pacifico Yokohama, Japan, April 24 2014.

5. H. Nakao, T. Inagaki, A. Shirakawa, K. Ueda, H. Yagi, and T. Yanagitani," Yb^{3+}-doped Lu_2O_3 ceramic thin-disk laser, "3rd Advanced Lasers and Photon Sources (ALPS '14), paper ALPS2-8, Yokohama, April 23, 2014.

6. A. Shirakawa, H. Nakao, T. Inagaki, K. Ueda, H. Yagi, and T. Yanagitani, " Ceramic thin-disk lasers of Yb^{3+}:$Lu_3Al_{12}O_5$ and Yb^{3+}:Lu_2O_3, " 9th Laser Ceramics Symposium (LCS 2013), paper C-1, Daejeon, Korea, Dec. 3, 2013. (Invited talk)

7. A. Shirakawa, H. Nakao, Y. Higashi, K. Ueda, Y. Ezura, and H. Ishizawa, " Yb^{3+}-doped CaF_2-LaF_3 Ceramic Laser, " Advanced Solid-State Lasers (ASSL) 2013, paper JTh5A , Paris, France, Oct. 31, 2013.

8. H. Nakao, A. Shirakawa, K. Ueda, H. Yagi, T. Yanagitani, B. Weichelt, K. Wentsch, M. Abdou Ahmed, and T. Graf, " Yb^{3+}-doped $Lu_3Al_5O_{12}$ ceramic thin-disk laser, " CLEO-PR & OECC/PS 2013, paper ThA3-3, Kyoto, Japan, July 4, 2013.

9. A. Shirakawa, M. Tokurakawa, H. Nakao, K. Ueda, and A.A. Kaminskii, " Ultrafast ceramic lasers, " 8th Laser Ceramics Symposium, Nizhny Novgorod, Russia, Dec. 7, 2012. (invited talk)

10. H. Nakao, A. Shirakawa, K. Ueda, H. Yagi, and T. Yanagitani," Efficient CW laser operation of Yb:LuAG ceramic laser, " CLEO 2012, paper CM2D.4, San Jose, USA, May 7, 2012.

11. H. Nakao, A. Shirakawa, K. Ueda, A. A. Kaminskii, S. Kuretake, N. Tanaka, Y. Kintaka, K. Kageyama, H. Yagi, and T. Yanagitani, " Investigation of the laser and optical properties of new laser materials, " 7th Laser Ceramics Symposium, paper I-6, Singapore, Nov. 15, 2011. (invited talk)

Posters

1. H. Nakao, A. Shirakawa, K. Ueda, H. Yagi, T.Yanagitani, B. Weichelt, K. S. Wentsch, M. Abdou Ahmed, and T. Graf, " Efficient High Power Operation of Yb^{3+}-doped $Lu_3Al_5O_{12}$ ceramic thin-disk laser, "Advanced Solid-State Lasers (ASSL) 2013, paper ATu3A.23, Paris, France, Oct. 29, 2013.

2. H. Nakao, A, Shirakawa, K. Ueda, H. Yagi, and T. Yanagitani, " CW and mode-locked operation of Yb^{3+}-doped $Lu_3Al_5O_{12}$ ceramic laser, " International Workshop on Laser Science (IWLS), paper P-5, Chofu, Japan, Oct. 5, 2012.

3. H. Nakao, A. Shirakawa, K. Ueda, H. Yagi, and T. Yanagitani, " Mode-locked Yb^{3+}-doped $Lu_3Al_5O_{12}$ ceramic laser, " 5th EPS-QED Europhoton Conference 2012, paper TuP.10, Stockholm, Sweden, Aug. 28, 2012.

4. 4. Hiroaki Nakao, A. Shirakawa, K. Ueda, L. Bohat, P. Becker, and A. A. Kaminskii, " Na,Nd co-doped $Ca_2MgSi_2O_7$ laser, " CLEO/Europe 2011, paper CA.P.17, Munich, Germany, May 22, 2011.

Domestic conferences

Talks

1. 東 祐軌, 富田 貴之, 布施 純一, 中尾 博明, 植田 憲一, 呉竹 悟志, 金高 祐二, 村山 浩二, 田中 伸彦, Alexander A. Kaminskii, "フェムト秒モード同期 Nd^{3+}添加 $Ba(Zr,Mg,Ta)O_3$セラミックレーザー," 第 75 回応用物理学会秋季学術講演会, paper 20p-C8-5, 北海道大学, 北海道, 2014 年 9 月 20 日.

2. 中尾 博明, 白川 晃, 植田 憲一, 八木 秀喜, 柳谷高公, Birgit Weichelt, Katrin Wentsch, Marwan Abdou Ahmed, andThomas Graf,"高出力・高効率 Yb:LuAG セラミック thin-disk レーザー," 第 75 回応用物理学会秋季学術講演会, paper 20p-C8-4, 北海道大学, 北海道, 2014 年 9 月 20 日.

3. 北島 将太朗, 中尾 博明, 白川 晃, 植田 憲一, 八木 秀喜, 柳谷高公, "モード同期 Yb^{3+}添加 $Lu_3Al_5O_{12}$セラミックレーザー," 第 75 回応用物理学会秋季学術講演会, paper 20p-C8-3, 北海道大学, 北海道, 2014 年 9 月 20 日.

4. 中尾 博明, 稲垣 達也, 白川 晃, 植田 憲一, 八木 秀喜, 柳谷高公, Alexander A. Kaminskii, "LD 励起 Yb^{3+}添加 Lu_2O_3セラミック thin-disk レーザー," レーザー学会第 34 回年次大会, paper B21aIV10, 北九州国際会議場, 福岡, 2014 年 1 月 21 日.

5. 東 祐軌, 布施 純一, 中尾 博明, 植田 憲一, 呉竹 悟志, 田中 伸彦, 金高 祐二, 景山 恵介, Alexander A. Kaminskii, "Nd^{3+}添加 $Ba(Zr,Mg,Ta)O_3$セラミックレーザーの研究," 第 74 回応用物理学会秋季学術講演会, paper 19a-A14-12, 同志社大学, 京都, 2013 年 9 月 19 日.

6. 稲垣 達也, 中尾 博明, 白川 晃, 植田 憲一, 八木 秀喜, 柳谷高公, "Yb^{3+}添加 Lu_2O_3セラミック thin-disk レーザー," 第 74 回応用物理学会秋季学術講演会, paper 19a-A14-10, 同志社大学, 京都, 2013 年 9 月 19 日.

7. 中尾 博明, 白川 晃, 植田 憲一, 八木 秀喜, 柳谷高公, Birgit Weichelt, Katrin Wentsch, Marwan Abdou Ahmed, and Thomas Graf, "100 W Yb^{3+}添加 $Lu_3Al_5O_{12}$セラミック thin-disk レーザー," 第 74 回応用物理学会秋季学術講演会, paper 19a-A14-9, 同志社大学, 京都, 2013 年 9 月 19 日.

8. 中尾 博明, 白川 晃, 植田 憲一, 八木 秀喜, 柳谷 高公, " 半導体レーザー励起 Yb 添加 LuAG セラミックレーザー, " 春季第 59 回応用物理学関係連合講演会, 16p-E9-7, 早稲田大学, 2012 年 3 月 16 日.

9. 中尾 博明, 白川 晃, 植田 憲一, 八木 秀喜, 柳谷 高公, " Yb 添加 LuAG セラミックのレーザー及び分光特性, " レーザー学会学術講演会第 32 回年次大会, 31aI4, TKP 仙台カンファレンスセンター, 2012 年 1 月 31 日.

10. 中尾 博明, 白川 晃, 植田 憲一, Ladislav Bohaty, Petra Becker, Alexander A. Kaminskii, “ 相転移による Na,Nd 共添加 $Ca_2MgSi_2O_7$レーザーの特性変化, ” 秋季第 72 回応用物理学会学術講演会, 30p-J-9, 山形大学, 2011 年 8 月 30 日.

11. 中尾 博明, 白川 晃, 植田 憲一, Ladislav Bohaty, Petra Becker, Alexander A. Kaminskii, “ Na,Nd 共添加 $Ca_2MgSi_2O_7$レーザーにおける相転移による特異な振る舞い, ” 春季第 58 回応用物理学関係連合講演会, 27-KG-7, 神奈川工科大学, 2011 年 3 月 27 日.

12. 中尾 博明, 白川 晃, 植田 憲一, Ladislav Bohaty, Petra Becker, Alexander A. Kaminskii, “ Na,Nd 共添加 $Ca_2MgSi_2O_7$レーザー, ” 秋季 71 回応用物理学会学術講演会, 14p-D-13, 長崎大学, 2010 年 9 月 14 日.

Posters

1. 中尾 博明, “ 高出力セラミックレーザーの研究, ” 第三回先端フォトニクスシンポジウム, 51, 日本学術会議, 2013 年 4 月 26 日.

2. 中尾 博明, 白川 晃, 植田 憲一, 八木 秀喜, 柳谷 高公, “ Yb:LuAG セラミックレーザーの開発, ” 第 5 回文部科学省「最先端の光の創成を目指したネットワーク研究拠点プログラム」シンポジウム, 76, 日本科学未来館, 2013 年 1 月 11 日.

Awards

1. 電気通信大学学生表彰, 2013 年 3 月.

2. 第 12 回レーザー学会東京支部研究会　ポスター講演優秀賞, 2012 年 3 月.

Acknowledgments

The work presented in this thesis was supervised by Prof. Dr. Ken-ichi Ueda and associate Prof. Dr. Akira Shirakawa. From 2009 to 2012, Prof. Dr. Ken-ichi Ueda was my supervisor. His instructions were always the philosophy and gave me the rout towards the researcher. Unfortunately, he have been retired at the same time as the finish of my Master degree. I was greatly impressed with his quite flexible consciousness. I would like to express my sincere appreciation to Prof. Dr. Ken-ichi Ueda.

Before his retirement and during my Ph.D, associate Prof. Dr. Akira Shirakawa guided me with sincerity. He greatly supported me not only as a student, but also as a researcher. I was served many precious opportunities such as attendance to the various international conferences, three months overseas stay, etc.. I also would like to express my sincere appreciation to associate Prof. Dr. Akira Shirakawa.

This work was also greatly supported by Prof. Dr. Thomas Graf and his colleagues at the IFSW. Firstly, I would like to thank Prof. Dr. Thomas Graf for accepting my three month stay. The stay gave me not only the basics of the thin-disk techniques, but also many cultural shock. Everything was quite impressive. It's hard to get my incredible experience out at the Oktoberfest!

I also would like to thank Dr. Marwan Abdou Ahmed for his kind help during my stay. I learned many things from him, and his support is really helpful even now! It was difficult to complete my three months stay without your help.

I thank to all of the members of the IFSW, Martin Rumple, Birgit Weichelt, Katrin Sara Wentsch, Stefan Piehler, Michael Eckerle, Jan-Philipp Negel, Johannes Früchtenicht, and Cherry May Mateo. They really helped me, and I really enjoyed the communication with them. Vielen herzlichen Dank!

I would like to thank Dr. Hideki Yagi, and Dr. Takagimi Yanagitani in Konoshima Chemical Co. Ltd. for providing me excellent ceramics. This

work could not be completed without their kind cooperation.

I would like to thank Prof. Dr. Alexander A. Kaminskii for teaching me his quite deep understand regarding the crystals. The discussion with him also improved my English skill.

I would like to thank Prof. Dr. Masayoshi Watanabe, Prof. Dr. Masayuki Katsuragawa, associate Prof. Dr. Junji Kawanaka for sparing their time to review my Ph.D thesis.

I would like to thank the staffs of ILS. I would like to thank Prof. Dr. Hitoki Yoneda who is also my supervisor. I learned many things from his deep, strict and precise advises. He also gave me the unobtainable opportunities: GenkaiT and Elementaly Teaching Laboratory (ETL). Both are the great programs to convert the book knowledges to the actual experiences via my body directly.

I would like to thank Mz. Mie Asuma, Ms. Mina Ito and Ms. Shoko Okudaira for greatly supporting my 6 years student life.

I would like to thank Prof. Dr. Ken'ichi Nakagawa and Prof. Dr. Hajime Nishioka for spending the time for teaching the laser basics.

I would like to thank associate Prof. Dr. Mitsuru Musha for not only supporting me as the student but also shearing the many time as a colleague.

I also would like to thank Dr. Masaki Tokurakawa for teaching me the fundamentals of the solid-state lasers and giving me a great opportunity to enter the thin-disk world.

I would like to thank the members of Shirakawa and Musha-lab. I would like to thank Mingchen Chen and Toshiyuki Kitamura who are my best friends from my undergraduate years. I strongly wish they also have the same feeling because we're in the same boat for $5 \sim 6$ years.

I also would like to other lab. members for sharing a lot of time.

I would like to thank Mr. Akiyoshi Sugo, Mrs. Yoko Sugo, Mr. Masumitsu Sugo who are staffs of Daikoku-sushi for their kind food supports when I was a part-timer until the restaurant have been closed in February 2014.

I also would like to thank my late parents, and grand parents for kind support in my life.

Finally, I would like to express my sincere appreciation to Yuka Tarumi, to be my wife, for greatly supporting me mentally. It is impossible to complete all of my university life without you. Again I really thank you and am really sorry for leaving you alone too long.